Diffusion Tensor Imaging Analysis of the Visual Pathway with Application to Glaucoma

Diffusion Tensor Imaging Analyse der Sehbahn zur Glaukomerkennung

Der Technischen Fakultät der
Universität Erlangen–Nürnberg

zur Erlangung des Grades

DOKTOR–INGENIEUR

vorgelegt von

Ahmed El-Rafei

Erlangen — 2012

Als Dissertation genehmigt von der
Technischen Fakultät der
Universität Erlangen-Nürnberg

Tag der Einreichung:	23.01.2012
Tag der Promotion:	13.03.2012
Dekan:	Prof. Dr.-Ing. M. Merklein
Berichterstatter:	Prof. Dr.-Ing. J. Hornegger
	Prof. Dr. J.M.R.S. Tavares

Abstract

Glaucoma is an optic neuropathy affecting the entire visual system. The worldwide prevalence of glaucoma is estimated to be 60.5 million people. The visual disorder caused by glaucoma can reach complete blindness if untreated. Various treatment approaches exist that can largely prevent the visual disability and limit the vision loss due to glaucoma if the disease is diagnosed in its early phases. Nevertheless, the slow progression of the disease along with the lack of clear symptoms results in the late identification of glaucoma. Moreover, the pathophysiology of glaucoma, and its biological foundation and factors are not yet fully determined or understood. Therefore, novel directions are essential for improving the diagnostic flow and the understanding of the glaucoma mechanism.

Most of the glaucoma diagnostic methods analyze the eye with a main focus on the retina, despite the transsynaptic nature of the fiber degeneration caused by glaucoma. Thus, they ignore a significant part of the visual system represented by the visual pathway in the brain. The advances in neuroimaging, especially diffusion tensor imaging (DTI), enable the identification and characterization of white matter fibers. It has been reported that glaucoma affects different parts of the visual system. Optic nerve and optic radiation were shown to have abnormalities measured by DTI-derived parameters in the presence of glaucoma. These outcomes suggest the significance of visual pathway analysis in the diagnosis.

In this work, we propose visual pathway analysis using DTI in glaucoma diagnosis to complement the existing retina-based techniques. A system is proposed to automatically identify the optic radiation on the DTI-images. The segmentation algorithm is applied to healthy and glaucoma subjects and showed high accuracy in segmenting such a complicated fiber structure. The automation eliminates the necessity of medical experts' intervention and facilitates studies with large number of subjects. This algorithm was incorporated in a framework for the determination of the local changes of the optic radiation due to glaucoma using DTI. The framework can aid further studies and understanding of the pathophysiology of glaucoma. Moreover, the framework is applied to normal and glaucoma groups to provide localization maps of the glaucoma effect on the optic radiation. Finally, we propose a system that extracts different aspects of the visual pathway fibers from the diffusion tensor images for detecting and discriminating different glaucoma entities. The classification results indicate the superior performance of the system compared to many state of the art retina-based glaucoma detection systems.

The proposed approach utilizes visual pathway analysis rather than the conventional eye analysis which presents a new trend in glaucoma diagnosis. Analyzing the entire visual system could provide significant information that can improve the glaucoma examination flow and treatment.

Zusammenfassung

Glaukomerkrankungen sind eine Optikusneuropathie, die das gesamte visuelle System beeinflusst. Die weltweite Prävalenz des Glaukoms wird auf 60,5 Millionen Menschen geschätzt. Unbehandelt kann die durch ein Glaukom verursachte visuelle Beeinträchtigung bis zu völliger Blindheit führen. Eine Erkennung der Krankheit im Frühstadium kann dies verhindern. Glaukomerkrankungen werden jedoch meist zu spät identifiziert, da die Erkrankung langsam fortschreitet und kaum eindeutige Symptome aufweist. Darüber hinaus sind die Pathophysiologie des Glaukoms und seine biologischen Grundlagen und Faktoren bisher noch nicht vollständig ermittelt und verstanden. Deshalb müssen neue Wege in der Forschung und Diagnostik eingeschlagen werden, um das Verständnis der zugrunde liegenden Mechanismen und letztendlich die Behandlung zu verbessern.

Der Großteil der aktuell eingesetzten Methoden zur Glaukomdiagnose analysiert schwerpunktmäßig die Netzhaut des Auges, trotz der transsynaptischen Natur der Faserdegeneration, die ein Glaukom verursacht. Diese Ansätze ignorieren einen erheblichen Teil des visuellen Systems, nämlich die Sehbahn im Gehirn. Die Fortschritte in der Bildgebung, insbesondere des Diffusion Tensor Imaging (DTI), ermöglichen die Identifizierung und Charakterisierung von Fasern der weißen Gehirnsubstanz. Untersuchungen haben ergeben, dass eine Glaukomerkrankung sich auf verschiedene Teile des visuellen Systems auswirkt. Parameter, die aus dem DTI abgeleitet wurden, zeigten bei Glaukompatienten Abweichungen für den Sehnerv und die Sehstrahlung. Dies ist ein starker Indikator für die diagnostische Relevanz der Sehbahnanalyse.

In dieser Arbeit werden Methoden zur Analyse der Sehbahn mittels DTI vorgestellt, mit denen bestehende netzhautbasierte Techniken zur Glaukomuntersuchung ergänzt werden können. Ein System zur automatischen Identifizierung der Sehstrahlung auf Basis des DTI wird präsentiert. Die Segmentierung wurde auf gesunde Personen und Glaukompatienten angewendet und zeigt eine hohe Genauigkeit bei der Segmentierung dieser komplizierten Faserstruktur. Die Automatisierung eliminiert die Notwendigkeit, medizinische Gutachten von Experten erstellen zu lassen und erleichtert Studien mit einer großen Anzahl von Patienten. Dieser Algorithmus ist die Grundlage eines Frameworks für die Bestimmung durch Glaukom verursachter lokaler Veränderungen der Sehstrahlung mittles DTI. Das Framework kann für weitere Studien und das Verständnis der Pathophysiologie des Glaukoms genutzt werden. Darüber hinaus wurde das Framework auf Gesunde und Glaukompatienten angewendet, um eine Kartographierung des Glaukomeffekts in der Sehstrahlung zu ermöglichen. Schließlich wird ein System zur Erkennung und Unterscheidung verschiedener Glaukomformen vorgeschlagen, das auf einer DTI-Analyse der Sehbahn-Fasern basiert. Die Klassifikationsergebnisse zeigen die hohe Genauigkeit des Systems im Vergleich zu vielen aktuellen netzhautbasierten Glaukom-Erkennungsystemen.

Der vorgeschlagene Ansatz nutzt die Sehbahn-Analyse, die einen neuen Trend in der Glaukom-Diagnose darstellt, anstelle der üblichen Augenanalyse. Eine Analyse des gesamten visuellen Systems kann wichtige Informationen ergeben, die den Ablauf der Glaukomuntersuchung und die Behandlung verbessern.

Acknowledgment

I would like to thank God and I extremely appreciate His unlimited blessings in my life.

I would like to express my highest appreciation to Prof. Dr.-Ing. Joachim Hornegger for giving me the opportunity to work under his supervision. The productive and structured environment created in the Pattern Recognition Lab (LME) is greatly attributed to his efforts which I have largely learnt and benefited from. During the PhD, his outstanding support, guidance, and understanding were very important to motivate and help me concentrate on the work progress.

The research presented in this thesis is the result of the co-operation between the pattern recognition lab, the department of Ophthalmology, and the department of Neuroradiology in the Erlangen-Nuremberg University. This multidisciplinary project would not have been successful, if it was not for the outstanding coordination and contribution from all the members. Therefore, I am deeply grateful to Prof. Dr. med. Georg Michelson for enriching my knowledge in ophthalmology, for his great continuous support, and for accepting to review my dissertation. The chance given to me by Prof. Dr. med. Arnd Dörfler to work in the department of Neuroradiology is tremendously beneficial for an engineer to get an insight into the clinical flow. In addition, I am greatly thankful for sharing his expertise. Many thanks go to Dr. Simone Wärntges and Dr. Tobias Engelhorn who provided me with the medical foundation and feedback necessary to understand and contribute to this project and were excellent cooperation partners.

I would like to thank Prof. Dr. João Tavares for his acceptance to be a member of the reviewing committee and Prof. Dr. Burak Acar for his valuable guidance and technical advices in the field of diffusion tensor imaging processing.

Many thanks to my colleagues at the Pattern Recognition Lab, especially to my team members Jörg Meier, Rüdiger Bock, Markus Mayer, Attila Budai, Jan Paulus, Thomas Köhler, Ioannis Moupagiatzis, and Lenke Laurik. Special thanks go to Rüdiger Bock and Markus Mayer for their mentoring and fruitful discussions. I am grateful to Markus Mayer, Firas Mualla, Ioannis Moupagiatzis, Lenke Laurik, Christian Riess, and Dr.-Ing. Tino Haderlein for the thesis proof reading. I would like to thank the adminstration and the technical staff at the Pattern Recognition Lab particularly Mrs. Kristina Müller and Mr. Friedrich Popp.

I gratefully acknowledge the funding of the German Academic Exchange Service (DAAD) and the Erlangen Graduate School in Advanced Optical Technologies (SAOT) by the German National Science Foundation (DFG) in the framework of the excellence initiative.

I am deeply thankful to my wife Nancy Shaker who always stands beside me and surrounds me with love and care. Furthermore, I would like to thank her for shining my world with my daughter Merna and my son Karim. I can not find enough words to thank my parents for their endless support during my whole life. I am also grateful to my family, especially my brother. I dedicate this dissertation to the soul of my father who was my friend, mentor, and role model. He was and will always be the

source of encouragement and inspiration in my life and will always be in my heart guiding my steps.

Ahmed El-Rafei

Contents

Chapter 1

Overview

1.1 Motivation

Glaucoma is an optic neuropathy accompanied by visual disorder. The progression of glaucoma results in visual impairment that can reach complete vision loss if untreated. It is the second leading cause of blindness in the world affecting more than 60 million people with 8.4 million people suffering from bilateral blindness [Quig 06]. The glaucomatous vision loss is irreversible. Nevertheless, if glaucoma is detected in an early stage, its progression can be delayed or stopped. Different clinical methods are present to assist the diagnosis. However, the complex nature of the glaucoma disease and the necessity for early diagnosis methods impose the exploration of new directions that can be integrated in the diagnostic flow to improve the screening and the identification of the disease and in turn assist the treatment.

The mechanism of glaucoma remains an area of research with no definite understanding. However, morphological damage along the visual pathway and the functional assessment are used to identify the presence of the disease. Glaucoma is accompanied by gradual loss of the retinal ganglion cells and their axons leading to a thinning of the retinal nerve fibers comprising the optic nerve [Fech 94]. Different imaging modalities currently exist that provide structural information and images to characterize the previously mentioned changes. Fundus imaging cameras, Heidelberg retina tomograph (HRT), and optical coherence tomography (OCT) are examples of the currently available modalities that produce valuable information about the retina. Other techniques test the visual function of the eye such as the frequency doubling technology (FDT).

The common factor between all the aforementioned techniques is that they all focus on the eye, especially the retina region, which is mainly responsible for acquiring the visual information. This neglects the growing evidence that glaucoma is likely a systemic disease that generally affects the entire visual system. The human visual system contains cerebral white matter fibers and gray matter centers that transmit and process the visual information, respectively [Wich 04, Remi 04]. In experimental glaucoma, the degeneration has been shown to be transsynaptic. i.e., atrophy is transmitted from diseased neurons to healthy nerve cells through synaptic connections [Gupt 07]. The neuronal degeneration of glaucoma was shown to extend to different parts of the visual pathway spreading to the intracranial optic nerve, the

lateral geniculate nucleus and the visual cortex [Gupt 06]. The integrity of the white matter fibers of the optic nerve and the optic radiation is reported to be globally decreased assessed by parameters derived from the diffusion tensors [Hui 07, Gara 09]. Moreover, the optic radiation showed localized structural changes using morphometry analysis in the presence of glaucoma [Hern 11]. These findings indicate that there is a great potential in diagnosing glaucoma using visual pathway analysis.

Diffusion tensor imaging (DTI) opened a new dimension in the field of neuroimaging [Mori 99, Le B 01] enabling the reconstruction of the brain white matter structure non-invasively and in-vivo [Bass 02, Nuci 07]. It allows building an atlas of white matter fibers [Mori 08]. Moreover, DTI received a lot of attention due to its clinical applications [Dong 04] such as acute stroke detection as well as the demonstrated sensitivity of diffusion tensor-derived parameters to different neuropathologies including Alzheimer's disease and multiple sclerosis [Mose 90, Henr 03, Chen 09].

DTI is utilized in this work to characterize and identify the optic radiation as a part of the visual pathway. The complexity and the limited spatial resolution of the DTI data, the limitation of the diffusion tensor model, and the interpersonal variability of the brain fiber structure are among the challenges in the analysis of the fibers. Additionally, the identification and analysis of the optic radiation which has a complicated fiber structure with highly variable course is a serious challenge. Therefore, all the aforementioned issues need to be handled carefully when processing the DTI-data.

1.2 Contributions

This work extends the current state of the art in glaucoma detection and analysis from conventional eye examinations to visual pathway analysis. The general aim is to investigate the significance of the visual pathway analysis for giving insight into the disease and for detecting its different entities. To accomplish this goal, a set of tools are proposed in order to identify and analyze the visual pathway in the presence of glaucoma. The sensitivity of the DTI-derived parameters in detecting the abnormalities in the visual pathway fibers due to glaucoma is studied. The ability of the DTI-derived parameters, sensitive to the underlying fiber structure, to diagnose different forms of glaucoma is examined as well. The scientific contributions of this work are

1. **Optic Radiation Segmentation:** The developed optic radiation segmentation algorithm based on DTI-data is a fully automated fiber bundle identification algorithm. The automation of the system is utilizing the physiological and anatomical information to produce a robust initial estimation of the optic radiation. This estimation initializes a statistical level set framework. The level set formulation by Lenglet et al. [Leng 06] is extended to work with the Log-Euclidean framework. This maintained the simplicity and low computational cost of the calculations while avoiding the drawbacks of the Euclidean framework when dealing with the diffusion tensor space. The optic radiation is segmented by the surface evolution of the level set function. Moreover, the system is applicable to normal subjects and glaucoma patients with similar per-

formance [El R 09, El R 11a] regardless of the previously reported abnormalities in the optic radiation due to glaucoma. The purpose of this algorithm is to aid glaucoma studies by avoiding the user intervention while maintaining accurate segmentation of such a complex fiber structure as the optic radiation.

2. **A framework for voxel-based morphometry analysis of the optic radiation:** The aim of this work is to establish a framework for the determination of the local changes of the optic radiation due to glaucoma using DTI. The proposed system utilizes the previous automated algorithm to produce an efficient identification of the optic radiation. Segmented optic radiations are transformed to a unified space using shape-based non-rigid registration. The maps of the diffusion tensor-derived parameters from different subjects can be compared in the unified space. This allows for statistical voxel-wise analysis to produce significant abnormality maps. This framework is capable of capturing the significant local changes of the optic radiation due to glaucoma [El R 11b] and facilitates further studies and understanding of the pathophysiology of glaucoma.

3. **Voxel-based morphometry analysis of the optic radiation in glaucoma:** The proposed framework is applied to a group of glaucoma patients and a control group. The groups are age matched in order to eliminate the age effect on the analysis. Diffusion related parameters (axial, radial, and mean diffusivities) and an anisotropy index (fractional anisotropy) are studied. The analysis showed significant regional changes indicating different localized fiber abnormalities as demonstrated in [El R 11b]. The preliminary analysis suggests that the glaucomatous optic radiation may suffer from localized white matter degeneration. To the best of our knowledge, this is the first attempt to localize the glaucoma effect on the visual pathway using DTI.

4. **Glaucoma classification based on visual pathway analysis:** We propose a system based on DTI analysis of the visual pathway fibers in the optic radiation for detecting and discriminating different glaucoma entities. The optic radiation is identified semi-automatically based on our developed algorithm. DTI provides information about the fiber orientation and a set of derived parameters describing the degree of diffusion anisotropy and diffusivity. Features for each DTI derived measure are extracted from a specified region of interest on the optic radiation. The features are statistical features as well as texture features. These features are ranked according to their classification weights recursively and the top ranked features are used for classification. The system is applied on three age-matched subjects' categories containing healthy, primary open angle glaucoma (POAG), and normal tension glaucoma (NTG) subjects. The classification results indicate the high performance of the system compared to retina-based glaucoma detection systems. Moreover, it showed that using only the DTI modality and visual pathway analysis, it is possible to differentiate healthy subjects from different types of glaucoma patients. In addition, sub-classes of glaucoma can also be identified. The proposed approach utilizes visual pathway analysis rather than the conventional eye analysis which presents a new trend in glaucoma detection. An early version of the system with only histogram features and one glaucoma class was presented in [El R 11c].

The author contributed partially to the following medical studies

5. **Clustering of glaucoma subjects:** In [Mich 12c], glaucoma and normal groups were clustered taking into consideration the effects of age and the presence of microangiopathy. DTI-parameters and retinal nerve fiber layer thickness were used to determine the subjects' groups. The clustering analysis identified four different clusters showing an increased sensitivity of the DTI-parameters to advanced age glaucoma patients. This indicated the degeneration of white matter fibers in the optic radiation associated with the damage in the retinal nerve fiber. However, the results showed the inability to detect optic radiation impairment in the middle-aged group.

6. **Correlation of the integrity of the optic radiation to glaucoma indices:** The correlation between DTI-measures and indices describing the severity of glaucoma was investigated in [Mich 12a, Enge 12b]. The optic radiation was delineated using the aforementioned segmentation algorithm. DTI-parameters related to the integrity and demyelination degree of the fibers are extracted from the optic radiations. A correlation analysis was performed between these parameters and morphological, functional assessment indices of glaucoma. The results showed significant correlation between glaucoma severity and the optic radiation damage measured by DTI. This work is extended to include POAG and NTG groups [Mich 12b]. Fibers bundles of the visual pathway in addition to the optic radiation were also examined using degradation of the fractional anisotropy as an indicator of compromised fibers. This was accomplished by selecting regions of interest on the orbital and intracranial parts of the optic nerve, the optic chiasm, the lateral geniculate nucleus, and the optic radiation [Enge 12a].

1.3 Organization of the Thesis

The thesis is divided into two main parts. The first part (Chapters 2 and 3) contains the information related to the medical problem and the used imaging modality. The medical background of the glaucoma disease is described in Chapter 2. In Chapter 3, the basic principles of DTI are detailed. The background part is structured as follows:

- Chapter 2: The anatomical and functional aspects of the human visual system are necessary to understand the effect of different pathologies on the system and, therefore, are detailed in this chapter. The human visual system is divided into two major parts which are the eye, and the intracerebral pathway containg the white matter fibers and the gray matter centers in the cortex. Then, the mechanism of the glaucoma disease as well as the recent findings in glaucoma diagnosis is introduced. This includes the different glaucoma types and the effect of glaucoma on the visual system. The chapter concludes with an overview of the state of the art in glaucoma diagnostic systems. These systems are based on different imaging modalities that are briefly described indicating the capabilities of each of them and their application.

- Chapter 3: Diffusion weighted imaging is the basis of the DTI. Its physical principles and acquisition are presented. The construction of the diffusion tensor model from the diffusion weighted images is introduced. Valuable measures are derived from the diffusion tensor providing information regarding the fiber orientation and aspects of the underlying fiber structure. These measures are used in this work. Therefore, they are categorized and demonstrated. The utilization of the DTI-data to reconstruct the white matter fiber microstructure of the brain has followed many paths. Some of these approaches are highlighted in this chapter. This is followed by the introduction of the clinical applications of the DTI modality that attracted a great attention during the last decades.

After the background part, novel methods are proposed to advance the research of glaucoma using visual pathway analysis in the second part of the thesis (Chapters 4-6). The developed systems and algorithms focus on the processing of the optic radiation, a large fiber bundle in the visual pathway. A fully automated system for segmenting the optic radiation is proposed in Chapter 4. In Chapter 5, we propose a framework for providing localization maps of the glaucoma caused fiber disorder on the optic radiation. Chapter 6 examines the ability of DTI to discriminate healthy controls from glaucoma patients.

- Chapter 4: The chapter starts with a short introduction to the problem being considered and an overview to the proposed segmentation algorithm. Then, the various stages of the segmentation algorithm are detailed. The limitations of the Euclidean calculus in processing the diffusion tensor data and the proposed alternatives in the literature are reviewed. An automatic initialization of the optic radiation is suggested and is the input of a statistical level set framework. The mathematical formulation of extending the used statistical level set framework for DTI image segmentation to incorporate Log-Euclidean calculus is given. The algorithm is tested on normal and glaucoma subjects to demonstrate its ability to delineate the optic radiation in normal as well as pathological cases. The segmentation errors and the performance are analyzed in the discussion section.

- Chapter 5: The problem is defined in the introduction section showing the challenges and the current state of the art. The system is outlined in the methods and the utilized approach for morphometry analysis is described. The system is configured to operate on a specified region of interest. This is a crucial step as it requires manual intervention and so it is explained and tested. A registration is incorporated to transform all the subjects' images to a unified domain. This step is evaluated in order to judge the performance of the framework. The framework is primarily applied to show the regional differences between normal and glaucoma groups. These preliminarily maps and their interpretation in addition to the framework analysis are provided in the results and the discussion sections.

- Chapter 6: After an introduction, a classification system is presented. The conventional pipeline for the classification system is shown. This includes feature extraction, feature selection, and classification. The DTI derived features are

categorized according to their statistical order. Then, the importance of the features to the classification task is determined by applying a feature ranking algorithm. The classification is performed on different types of glaucoma and the evaluation of the system is demonstrated in the results section. Finally, the results and potential of the system are discussed.

- Chapter 7: The contributions of this work to the progress of the scientific research in the fields of glaucoma, visual pathway analysis, and DTI processing is summarized in this chapter. The conclusions are drawn from the presented novel approaches in form of methods and systems in addition to their application to the glaucoma disease.

- Chapter 8: In this chapter, the future extension of the glaucoma diagnosis and the potential provided by brain imaging in general and DTI in particular are discussed.

Chapter 2

Glaucoma

2.1 Introduction

The human visual system is responsible for acquiring and processing the visual information. Many diseases affect the visual system causing visual impairments that can reach blindness. Glaucoma is among the visual system diseases and is the second most common cause of blindness in the world with 8.4 million people and affecting 60.5 million people in 2010 [Quig 06]. The number of people with glaucoma and the number of glaucoma caused bilateral blindness are estimated to increase to 79.6 millions and 11.2 millions by 2020, respectively [Quig 06]. These estimations are based only on the two most common forms of glaucoma which are open angle glaucoma (OAG) and angle closure glaucoma (ACG). Other types of glaucoma exist leading to additional visual disorders and vision loss. In addition, glaucoma is a multifactorial disease having a complicated mechanism with many unresolved issues. The vision loss due to glaucoma is usually undetected in its early stages. The reasons for this are primarily the gradual loss of vision and the absence of clear symptoms. Glaucoma is considered in this work for the application of the developed systems. In this chapter, we introduce the necessary background required to understand the glaucoma disease and the motivation behind incorporating visual pathway information in the diagnosis of glaucoma. The anatomy and the function of the various parts of the human visual system are first explained. The glaucoma effect on the entire visual system indicating the recent findings in glaucoma pathophysiology is reviewed. This includes as well the different forms of glaucoma. Furthermore, the state of the art in glaucoma diagnosis systems are discussed with a main focus on the systems based on imaging modalities of the retina.

2.2 The Human Visual System

The human vision involves the processes of the outer world image acquisition, processing, and reception. The image acquisition is performed by the sensory part of the visual system, the eye. The eye focuses and projects the image in its visual field on the retina, the component in the eye responsible for the photoreception. The areas of vision that are captured by the eye are called the visual field. The visual field is usually divided into the left and right hemifields based on their relative position to

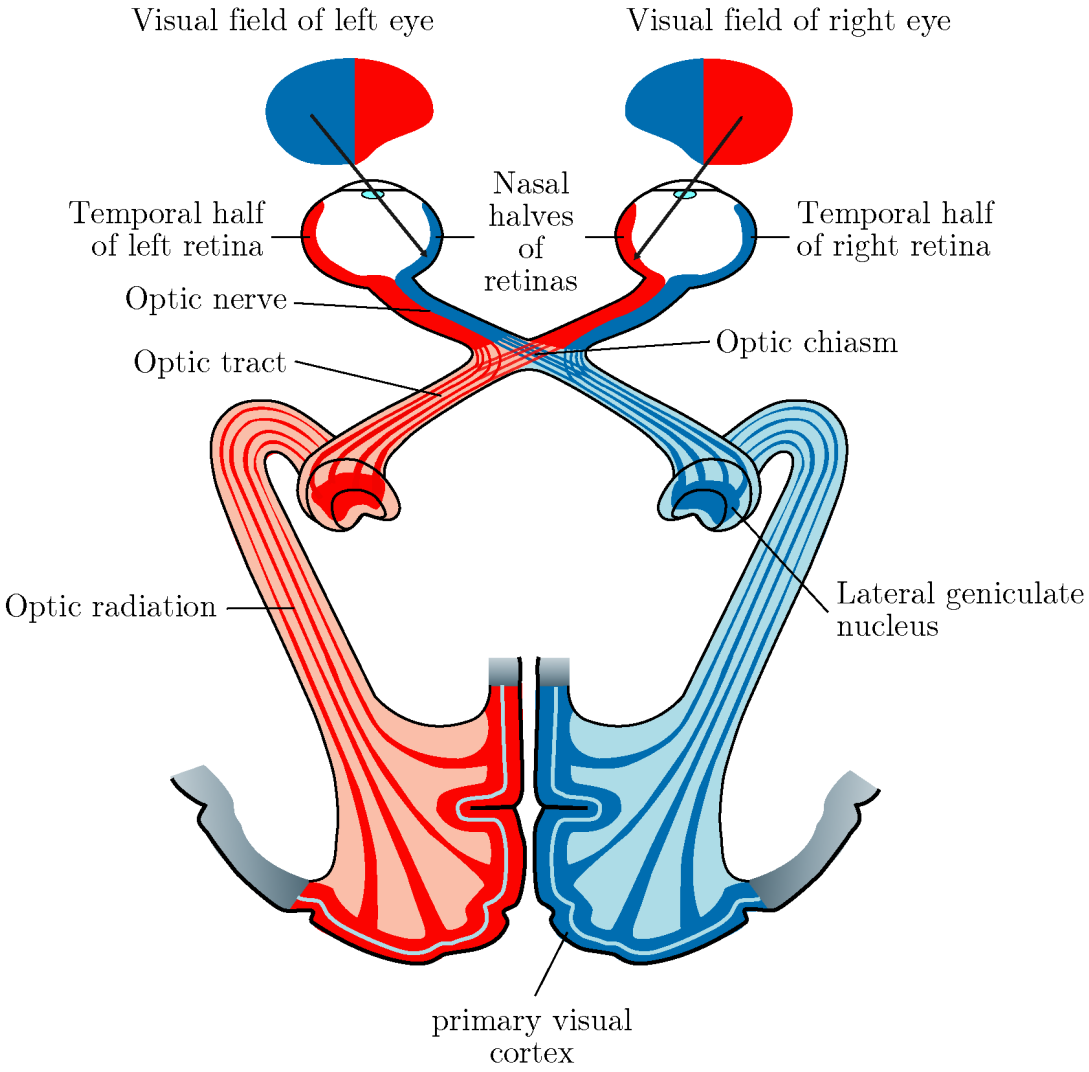

Figure 2.1: The human visual pathway. The visual system consists of the eye, the brain white matter fibers, and gray matter tissues.

the point where the eye is focused. The combined visual field from both eyes has a binocular shape and contains an intersection region seen by both eyes and two monocular regions seen individually by each eye. Each hemifield is further partitioned into nasal and temporal fields. The right hemifield is projected on the temporal half of the left eye's retina and the nasal half of the right eye's retina while the left hemifield is projected on the temporal half of the right eye's retina and the nasal half of the left eye's retina. The picture formed on the retina is neuronally decoded and transmitted to the brain through the optic nerve. The white matter fibers that carry the visual information in addition to the gray matter cortical centers that process this information constitute the visual pathway residing in the brain. The anatomy of the visual system with its two major components, the eye and the visual pathway, is essential to understand the glaucomatous insult. Further details on the function and the anatomy of the visual system can be found in [McCa 82, Nolt 02, Goeb 03, Mart 08]. The structure of the human visual system is illustrated in Figure 2.1.

2.2.1 The Eye

The eye is the interface of the visual system to the outer world. It has a spherical shape. The sensory component of the eye is the retina. The function of the rest of the eye is to provide means of nutrition and protection as well as mechanisms to acquire and focus the image on the retina. The structure of the eyeball is shown in Figure 2.2. The outer tissue of the eye is called the sclera. The sclera is a white, opaque, and dense fibrous tissue that contributes to the eye protection. In contrast to the opaque sclera, the anterior of the eye surrounding tissue is transparent allowing light transmission into the eye. This anterior tissue is referred to as the cornea and like the sclera has no vessels. The amount of light passing into the eye varies according to the strength of the illumination of the scene. This is controlled by the pupil, a circular opening in a diaphragm posterior to the lens known as the iris. In low light conditions, the pupil broadens to increase the amount of light entering the eye and it contracts in bright illumination conditions to reduce the light reaching the retina. The accurate projection of the picture on the retina is obtained by adapting the focus of the lens (accommodation). Similar to the tissues in the path of the light, the lens is transparent and avascular in addition to being elastic. The flexibility of the lens is an important aspect that allows the control of the lens refractive power by adjusting the curvature the biconvex lens. A set of ligaments, zounle fibers, attached to the lens are utilized by the ciliary muscle to adjust the focus of the lens. For example in case of a near object adaptation, the zounle fibers are relaxed by the contraction of the ciliary muscle causing the lens to bend forward and focus on the object nearby.

The ciliary muscle is part of the ciliary body which along with the iris and the choroid form the uvea. The uvea is anterior to the sclera/cornea tissue and contains a dense network of blood vessels. The choroid mainly provides nutrition for the retina. The space between the retina and the lens is occupied with a gelatin-like substance that consists mainly of water, vitreous. The light passes through the transparent vitreous before it reaches the retina. A compartment exists between the iris and the lens called the posterior chamber. The anterior chamber occupies the space between the cornea and the iris. Both chambers are filled with a thick fluid known as the aqueous humor. In addition to supplying the avascular tissues of the eye with nutrition, the aqueous humor plays an important role in preserving the intraocular blood pressure (IOP). Elevation of the IOP is usually correlated with widely spread common types of glaucoma. Therefore, we will describe briefly in the following paragraph the production, circulation, and drainage of the aqueous humor.

Aqueous Humor: The ciliary body forms the aqueous humor into the posterior chamber based on a number of interfering factors including blood flow, transcapillary exchange. The balance between the production and drainage of the aqueous humor through the extraocular venous capillaries maintains the IOP. Disturbance in the IOP affects the blood flow and consequently the production of the aqueous humor. It flows by hydrostatic pressure through the pupil into the anterior chamber. It is discharged into the venous drainage system of the eye via the trabecular meshwork in the iridocorneal angle [McCa 82]. The vertex of the iridocorneal angle is at the location where the iris meets the cornea. The aqueous humor supplies some of the eye structures which are not connected to the blood exchange network such as the lens, the cornea, and the iris with nutrients.

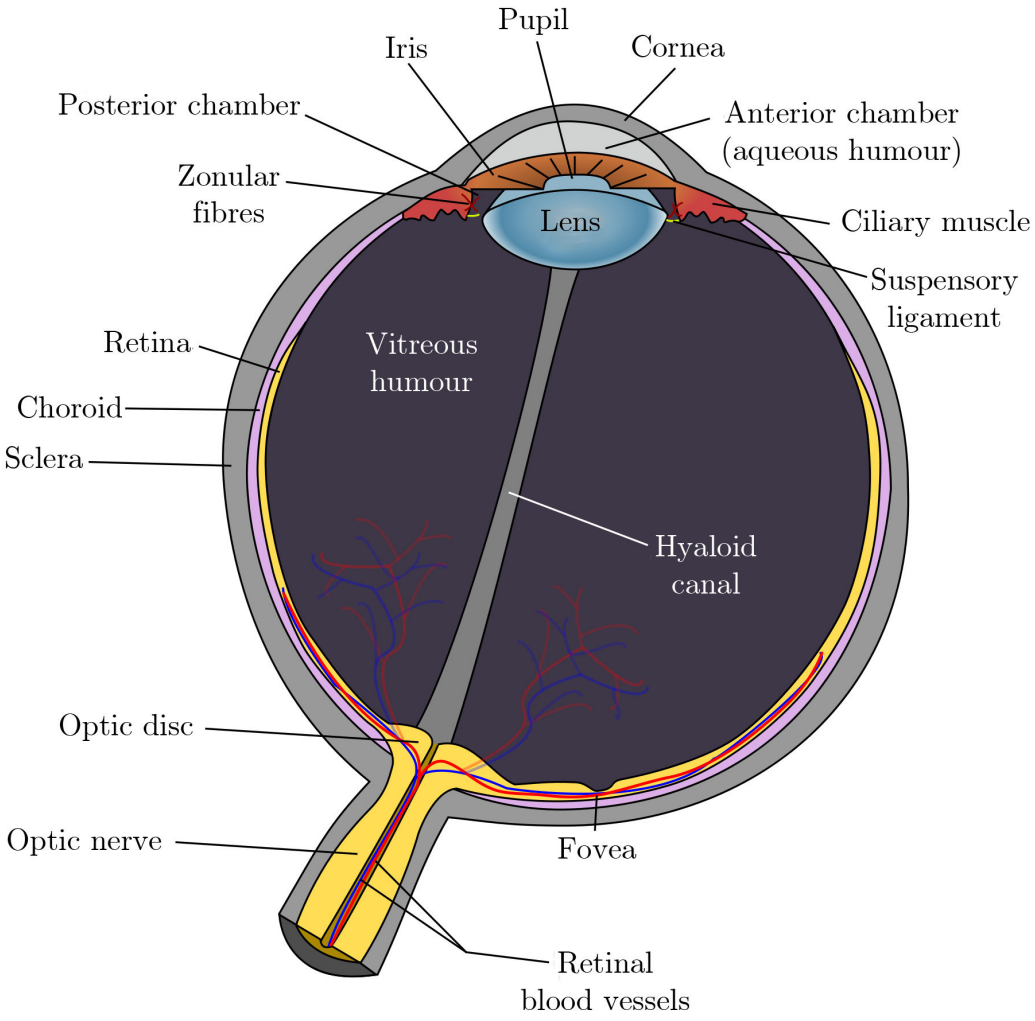

Figure 2.2: Structure of the eye showing the various layers comprising the eyeball. (public domain)

The Retina: Anatomically, the retina consists of five main layers [Goeb 03]. As shown in Figure 2.3 These layers are: (1) outer nuclear layer, (2) outer plexiform layer, (3) inner nuclear layer, (4) inner plexiform layer, (5) ganglion cell layer. The layers are ordered according to their relative position to the center of the eye sphere from the farthest to the nearest. The retina is the innermost part of the eye. The cell bodies of the photoreceptors reside in the outermost layer of the retina, the outer nuclear layer, meaning the light rays have to go through all the retinal layers before they are being absorbed. Excess light which has penetrated the retina is absorbed by the retinal pigment epithelium posterior to the aforementioned retinal layers preventing light reflections within the eye. The rods and the cones are the two primary types of photoreceptors cells. They transduce the light intensities into neural impulses. There are 120 million rods and 6 million cones [Goeb 03]. In daylight, the rods are almost saturated and do not provide any visual information while the three types of cones (with maximum sensitivity at the red, green, blue wavelengths in the spectrum) are stimulated and are able to resolve color information. On the contrary, rods are responsible for dim light vision. Thus, the ability to distinguish between different colors in night (scotopic) vision is lost because of the general insensitivity of rods to colors and the unstimulated cones [Butl 93]. A spot in the retina with an exceptional higher cones density is the fovea. Furthermore, no retinal layers or vessels are on the way of the incident light on the fovea. Thus, the sharpest vision occurs in the center of the visual field due to the special structure of the fovea. The neuronal impulses are transmitted through the synaptic outer plexiform layer to the bipolar and horizontal cells found in the inner nuclear layer. The inner plexiform layer contains synapses that carry the visual information further to the ganglion cells. The visual information arriving at the ganglion cell layer is largely compressed by the different retinal processes. This is evident from the approximately one million neurons in the ganglion cells down from more than 100 million photoreceptors [Nolt 02]. Magnocells (M cells) in the ganglion cell layer are specific for the rods and parvocells (P cells) receives the inputs from the cones [Mart 08]. The axons of the ganglion cells constitute the retinal nerve fiber layer which exits the eye as the optic nerve through the optic disc delivering the neuronal signals to the brain. A main object in the optic disc (also known as optic nerve head (ONH)) is the lamina cribrosa, a net-like structure. The holes in the net of the lamina cribrosa allow the retinal ganglion cells' (RGCs) axons to leave the eye boundary and the central vessels (artery and vein) for blood exchange to communicate with the intraocular blood capillaries. The lamina cribrosa isolates interior of the eye from the its exterior, having different pressure, playing an important role in maintaining the ocular pressure [Jona 03]. The neural part of the optic disc is called the rim while the remainder containing the vascular part has a cup-shaped structure and, therefore, is named the optic cup. The cup is located at the center of the ONH.

2.2.2 The Visual Pathway

The extension of visual system in the brain is referred to as the visual pathway and demonstrated in Figure 2.1. The visual pathway connects the retina to the primary visual cortex transversing the whole brain. The visual pathway consists of five white

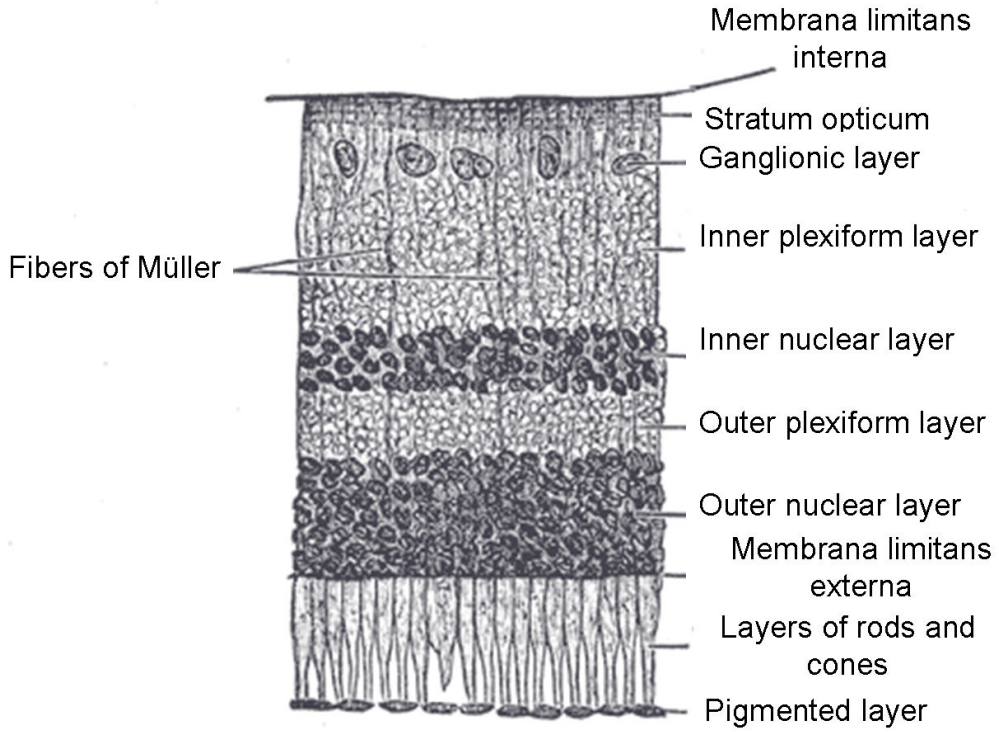

Figure 2.3: The different layers of the retina. From 20th U.S. edition of Gray's Anatomy of the Human Body, 1918 (public domain)

matter components: (1) Optic nerve, (2) optic chiasm, (3) optic tract, (4) lateral geniculate nucleus (LGN), and (5) optic radiation. These bundles transport the visual information to gray matter regions, the primary visual cortex, for processing. Further details on the visual pathway components are given in the following paragraphs.

The Optic Nerve : The one million axons of the retinal nerve fiber layer penetrate the eye boundaries and start the visual pathway in the human brain as the optic nerve. In the brain, myelin sheaths cover the axons. The optic nerve from each eye has ipsilateral (from the same side) and contralateral (from the opposite side) visual field components. These elements are captured by the nasal and the temporal retina halves.

The Optic Chiasm and the Optic Tract : The optic nerve parts corresponding to the temporal retina halves remain in their arising brain hemisphere. The fibers, originating from the nasal retina halves, cross their hemispheres at the optic chiasm. The merge of the nasal fibers arriving from the opposite hemisphere and the temporal fibers from the same hemisphere constitutes the optic tract. This means that the contralateral visual hemifield information (right/left hemifield) is regrouped in the opposite cerebral hemisphere (left/right hemisphere), after passing through the optic chiasm.

The Lateral Geniculate Nucleus : The optic tract fibers pass around the midbrain [Jage 05] and project into the LGN. The LGN is a six layered nucleus. The layers are numbered from the most inferior (1) to the most superior layer (6). After the merge of the contralateral visual field fibers, the LGN manage to discriminate

the inputs from each eye. This is achieved by dedicating three layers exclusively for a single eye and the other three layers for the other eye. These six layers are categorized according to the type of their ganglion cells origin (M or P cells) into: (a) magnocellular (layers 1 and 2), (b) parvocellular (layers 3 to 6) [Nolt 02]. Additionally koniocellular layers are located in the LGN where other cell types (bistratified cells) in the RGCs-layer project to the LGN [Lee 10].

The Optic Radiation: The LGN acts as a relay delivering the visual information to the visual cortex through the optic radiation also known as the geniculocalcarine tract. The optic radiation is a densely packed fiber bundle with a large number of myelinated axons. It is the largest bundle in the human visual pathway. It represents the magnocellular and the parvocellular projections to the occipital cortex [Goeb 03]. The optic radiation follows a rather complicated course with three main paths. The first course is followed by half of the optic radiation fibers going shortly in the anterior direction before they bend forming the Meyer's loop and running posteriorly to the cortex. The rest of the optic radiation fibers follow a direct posterior path to the cortex. The third optic radiation bundle moves laterally before turning posteriorly as well [Wich 04, Hofe 10]. However, the anterior-posterior orientation is the general and common course of the optic radiation. Near the distal end of the optic radiation, it fans out resulting in many small branches to reach the distributed visual processing centers.

The Visual Cortex: The fibers representing the right visual hemifield are linked to the primary visual cortex in the left cerebral hemisphere and vice versa. The primary visual cortex resides deeply in the calcarine sulcus and contains the gray matter centers that are responsible for processing the visual information and scene reconstruction. Moreover, it is thought to be the gate for performing the perception of the acquired scene such as objects identification, movements, etc. The superior visual field is linked to the lower bank of the calcarine sulcus while the inferior part of the visual field is linked to the higher bank of the calcarine sulcus. The central field captured by the fovea is mapped to a relatively large region in the posterior part cortex reflecting the more obtained information and resolution in this field.

2.3 The Glaucoma Disease

Glaucoma is a collection of optic neuropathies. It is a chronic disease that has various forms. Open angle glaucoma is the most common form of glaucoma. It is differentiated from ACG by the appearance of the iridocorneal angle. In the OAG, the iridocorneal angle is open having a normal form. On the other hand, the iridocorneal angle is closed in ACG. Glaucoma is further divided into primary and secondary. Primary glaucoma is characterized by the absence of additional ocular/systemic impairments. Regardless of the common features between primary and secondary glaucoma, secondary glaucoma might proceed differently. In addition, secondary glaucoma is accompanied by ocular/systemic diseases which could lead to the initiation of glaucoma.

The number of glaucoma patients due to the two most widely spread types of glaucoma which are OAG and ACG adds up to 60.5 million people in 2010. POAG percentage is 74% (44.7 millions) while ACG causes the remaining 26% (15.7) glau-

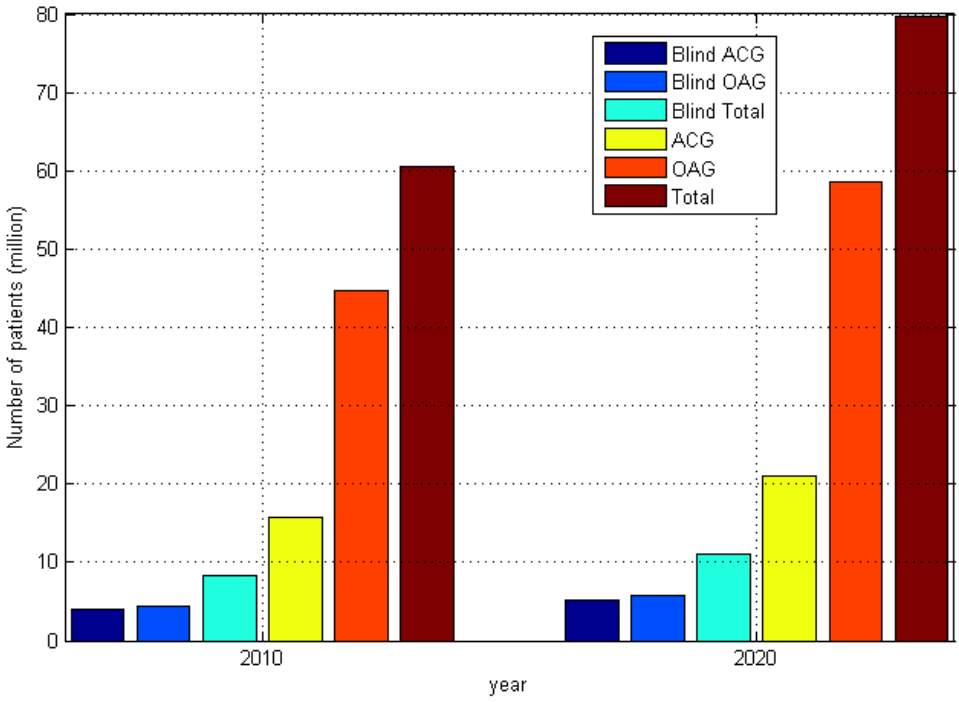

Figure 2.4: The distribution of open angle glaucoma (OAG) and angle closure glaucoma (ACG) in the year 2010 and 2020 according to the estimation in [Quig 06]. The number of people with bilateral blindness is shown for the total and the individual glaucoma types.

comatous damage. The glaucomatous bilateral blindness is estimated to be 8.4 with 4.5 and 3.9 million people by POAG and ACG respectively. The epidemiology of glaucoma is expected to rise significantly in 2020 to 79.6 million people among them are 11.2 million blind people. POAG contributes with 5.9 million vision loss cases (from 58.6 millions) and the ACG share is increased to 5.3 vision loss cases (from 21 millions). The glaucoma distribution numbers are based on the work by Quigley and Broman [Quig 06] and is illustrated in Figure 2.4.

The various entities of glaucoma have common characteristics that are used to identify the presence of the disease. The death of the RGCs and their axons, defects in the visual field, excavation of the optic disc, and optic nerve degeneration. IOP is a highly relevant feature of glaucoma. However, 50% of the people diagnosed with POAG do not have ocular hypertension [Somm 91]. Moreover, another type of OAG is the NTG where the IOP of the patients are always in the normal range. Nevertheless, reducing the IOP level has shown to delay or stop the progression of glaucoma even in NTG [Heij 02]. Despite the attempts aiming to provide a precise definition of glaucoma like the case definition in [Fost 02], the mechanisms of glaucoma are not completely understood and there are many challenges ahead of the scientific community to understand the pathology of glaucoma. Furthermore, it is argued that, due to the complex nature of glaucoma, all the aforementioned characteristics

do not provide a clear identification for glaucoma and still patients could be wrongly diagnosed with glaucoma or glaucoma could go undetected [Kroe 03].

2.3.1 Angle Closure Glaucoma

Angle closure glaucoma is a result of anatomical disorders that lead to obstructing the drainage flow of the aqueous humor through the trabecular meshwork. These disorders could be originally in the relative or absolute sizes of the anterior segment elements [Ritc 95]. The most common form of ACG is the pupillary block where the iridocorneal angle is narrowed or closed pressured by the iris anterior movement due to the accumulation of the aqueous humor in the anterior chamber [Ritc 99]. This increases the IOP either gradually or rapidly causing escalation of the glaucomatous damage. Family history, age, sex, and refractive errors are among the risk factors for ACG [Cong 92].

2.3.2 Open Angle Glaucoma

Several risk factors are suggested for OAG such as advanced age, family history, and ocular hypertension as well as a set of factors for predicting the glaucoma development [Cole 08]. Additional factors are race, thin corneal center, myopia [Dran 01]. Despite the normal appearance of the iridocorneal angle in POAG, the cycle of the aqueous humor is disturbed elevating the IOP. IOP is a prominent risk factor for OAG but it is not a characteristic feature of OAG as NTG patients do not experience any abnormal IOP. The IOP level of 21 mmHg is considered as the threshold between POAG and NTG. OAG patients with IOP greater than 21 mmHg are regarded as POAG while those having IOP less than 21 mmHg are diagnosed with NTG [Shie 08].

The glaucomatous optic neuropathy is accompanied by cupping of the ONH. The loss of the RGCs and axons in the retina progresses to the ONH reducing the thickness of the neuroretinal rim. In addition, the deterioration of the ONH connective tissues leads to a gradual posterior motion of the lamina cribrosa increasing the depth and the size the optic disc cup [Down 11]. The visual field defects in OAG are initiated in the mid peripheral field followed by a development in the peripheral and central fields [Quig 99].

The mechanisms of RGCs dysfunction and the optic nerve degeneration have been investigated in many studies. The pathophysiology behind ganglion cells death is attributed to different mechanisms. A class of these mechanisms is related to the ocular hypertension. The increase of the IOP reduces the axonal transport preventing the RGCs from receiving the neurotrophic factors, essential for the survival and functionality of neurons [Kwon 09]. In addition, the RGCs' axons are suggested to die due to the shortage of the blood perfusion to the optic nerve affecting the retinal vascular nutrition [Fech 94]. Other pathological procedures are thought to be involved in the glaucoma injury. Further information about the various pathogenesis involved in the OAG insult can be found in [Fech 94, Quig 99, Kueh 05, Kwon 09].

The glaucoma injury can not be generally reversed. However, many medical approaches exist for slowing or avoiding the development of glaucoma. Most of the glaucoma therapy strategies target the prevention of neuronal death. This is called

neuroprotection. The most common form of neuroprotection is the reduction of the IOP. The ocular pressure can be lowered by regulating the aqueous humor circulation. This can be performed surgically by providing an alternative drainage path or expanding the existing path for the aqueous humor. Other medical techniques aim to reduce the production of the aqueous humor by the ciliary body or to increment the drainage [Alwa 98]. Additional therapies with anti-glaucoma drugs, surgical, and laser methods are utilized for glaucoma treatment [Wein 04].

2.3.3 Glaucoma and the Visual Pathway

The functional and morphological disorders due to glaucoma at the eye level have been extensively studied. However, the pathogenesis of glaucoma indicates the potential of extending the impairment to the rest of the visual system [Gupt 07]. In experimental glaucoma on primates, the specific pathological features could be artificially initiated. An Example of such techniques is using laser to elevate the IOP. Yücel et al. induced glaucoma in monkeys by increasing the IOP leading to the degeneration of the RGCs and investigated the effect on the LGN and the visual cortex [Yuce 03]. They traced the projections corresponding to the M and P cells to the LGN in addition to the koniocellular layers and spotted transneuronal degeneration at the LGN. This showed that the atrophy is transmitted from diseased RGCs to healthy nerve cells in the visual pathway at the LGN through synaptic connections (i.e., transsynaptic degeneration). Moreover, the damage in the LGN due to elevated IOP occurred prior to any observed optic nerve fiber loss. The visual cortex was shown to be regionally affected as well. These results were supported by the study performed on a human case demonstrating spread atrophy along the visual pathway. This includes the intracranial optic nerve, lateral geniculate nucleus and visual cortex [Gupt 06].

The rapid development of neuroimaging techniques during the last decades allowed the identification of the human visual system in-vivo and non-invasively. This was utilized in recent studies examining glaucoma. The optic radiation was examined in glaucoma patients and the neuronal density was reported to be decreased causing size attenuation compared to normal subjects [Enge 11]. Furthermore, morphometry analysis using magnetic resonance imaging (MRI) aimed to detect volume changes on the visual pathway in glaucoma. The results of this analysis showed localized decreased volume differences along the visual pathway including the optic radiation [Hern 11]. A study produced glaucoma artificially in rats and found correlation between parameters indicating the cerebral optic nerve fibers disorder and glaucoma [Hui 07]. Garaci et al. evaluated the integrity of the white matter fibers and axonal structure of the optic nerve and the optic radiation in the presence of glaucoma. The fibers were compromised and the degree of degeneration in the optic nerve was found to be in correlation to the glaucoma severity [Gara 09].

2.4 Glaucoma Diagnosis

The glaucoma clinical examination has a wide variety of modalities that contribute to the identification of the disease. This variation of modalities arises from the complex nature of the glaucoma pathology where no single modality can provide a definite

decision. For example measuring the IOP as a major risk factor for glaucoma is not sufficient because its increase could be due to other diseases. The examination relies on evaluating the major glaucoma features which are the visual function and the optic disc appearance. In addition, ocular hypertension is an important indicator of the likelihood of having glaucoma and a determining factor for its progression path.

Optic Nerve Head: Instruments are developed for imaging the eye with a main focus on the retina. Fundus cameras take photographs of the interior surface of the eye detailing the vessel tree and the optic disc among other structure. Fundus images can be used to detect the excavation of the optic disc and the reduction of the rim area which are significant signs of glaucoma. One of the most important parameters for glaucoma diagnosis is the cup to disc ratio. Two example fundus images of normal and glaucoma subjects are shown in Figure 2.5. The rim thinning can be observed for the glaucoma case in Figure 2.5b. Despite that fundus images are two-dimensional images, acquiring stereo images can provide three-dimensional information [Naka 07].

Heidelberg retina tomograph (Heidelberg Engineering, Heidelberg, Germany) utilizes the principals of confocal scanning laser ophthalmoscopy to provide information about the topography of the retina surface. The topography is obtained by imaging sections of the retina which are used to reconstruct a three-dimensional view of the ONH. This allows for better representation and quantification of the optic disc. Glaucoma relevant variables are extracted using HRT such as horizontal and vertical cup-to-disc ratio, volume of cup and rim, and average RNFL thickness. The HRT-parameters were shown to be sensitive for glaucoma diagnosis [Ferr 08]. In Figure 2.6 an HRT acquisitions of normal and glaucoma subjects are demonstrated. Glaucomatous signs can be observed in the glaucoma patient.

Optical coherence tomography relies on measuring an interference pattern from a reference light following and a light reflected from the retina. The light used can penetrate the retinal layers providing depth information. The reflected light depends on the tissue structure and, thus, the components of the retina can be separated using OCT. Two-dimensional and three-dimensional images of the retina is obtained by combining depth scans. RNFL is segmented on OCT images as shown in Figure 2.7. The thickness of the RNFL demonstrated high ability to screen glaucoma in its early stages [Bowd 01, Nour 04].

Intraocular Pressure: The instrument used for measuring the IOP is called the tonometer. Different techniques are utilized for tonometry. The main idea behind applanation tonometry, the most common type of tonometry, is to directly apply a force to flatten a region on the cornea. The force required is related to the ocular pressure. This method is relatively accurate and widely integrated in the clinical flow. A less precise variation of this technique is the non-contact tonometry which is usually used for screening purposes. In this procedure, the corneal curvature is reduced by the application of an air pulse and similarly the force is measured. In addition to identifying ocular hypertension risk, tonometry can be used to evaluate the glaucoma treatment and its effect on the IOP.

Visual Function: The glaucomatous vision defects are located on the periphery of the visual field in its early stages. Perimetry is a widely used technique to examine the visual field. It detects the sensitivity of the eyes to identify light spots on a background at various positions in the visual field. Standard perimetry detects general

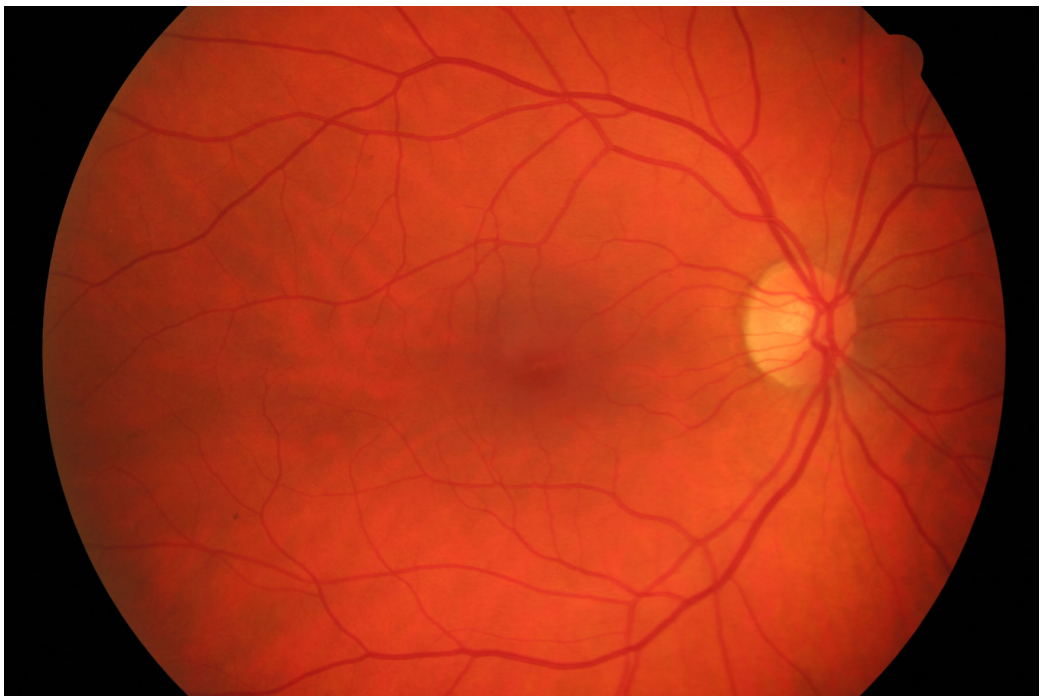

(a) Normal

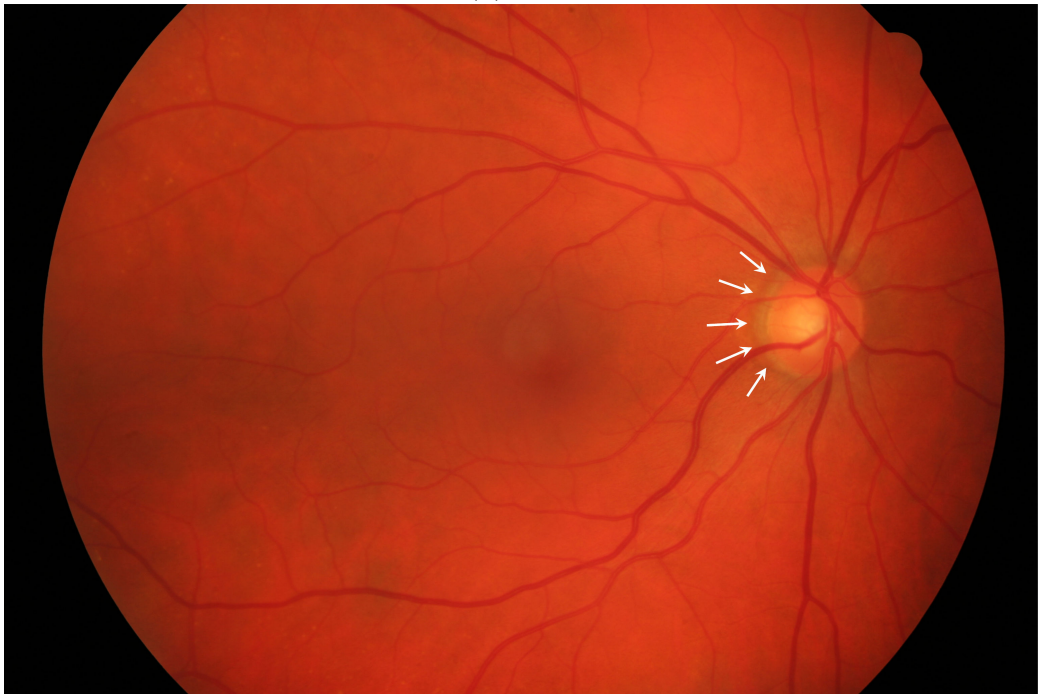

(b) Glaucoma

Figure 2.5: Fundus images showing the background of the retina for a healthy subject (a) and a glaucoma (b) patient. The optic disc region and the vessel tree are clearly visible in the images. (Source: [Buda 11])

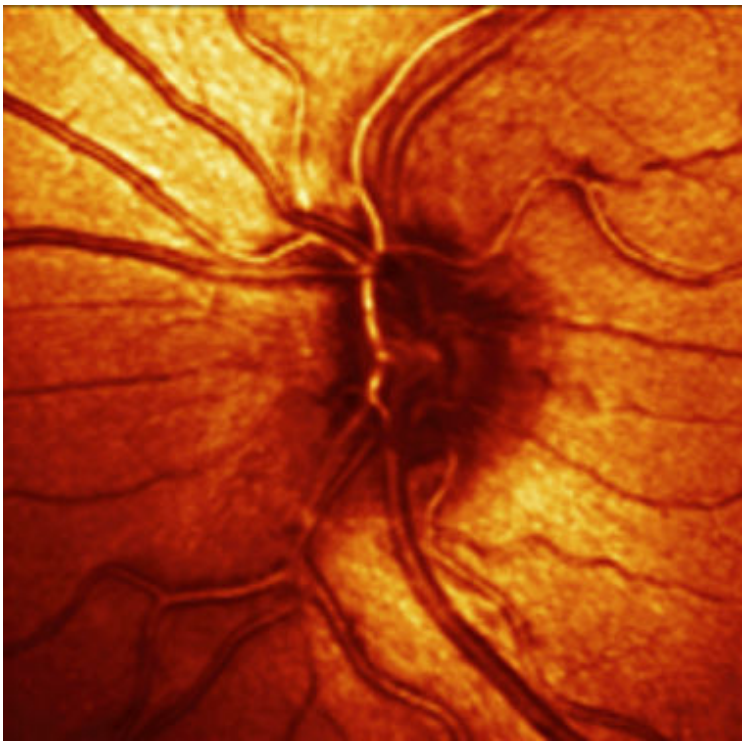

(a) Normal

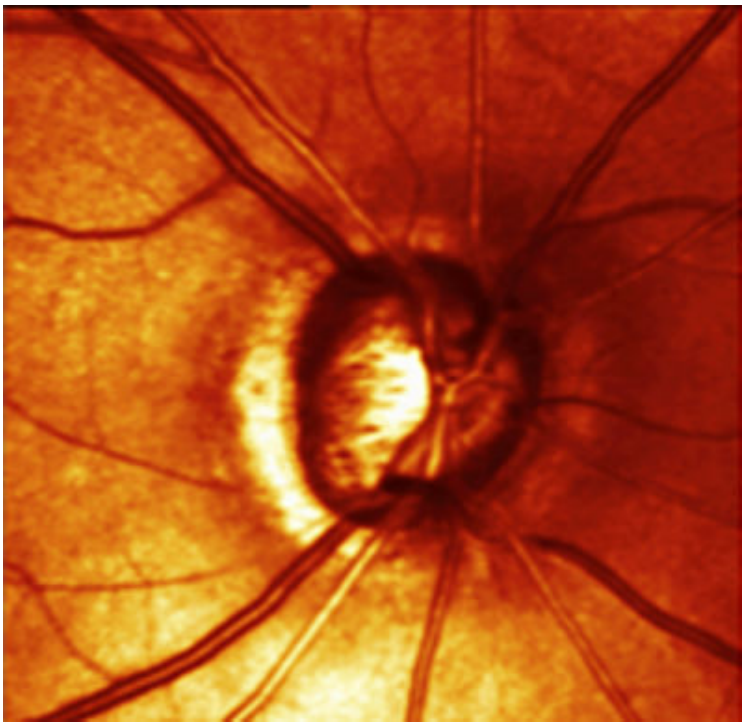

(b) Glaucoma

Figure 2.6: Two sample HRT-II images for a healthy subject (a) and a glaucoma (b) patient. The glaucomatous cupping is present in the optic nerve head. (Source: Erlangen Nuremberg University Hospital)

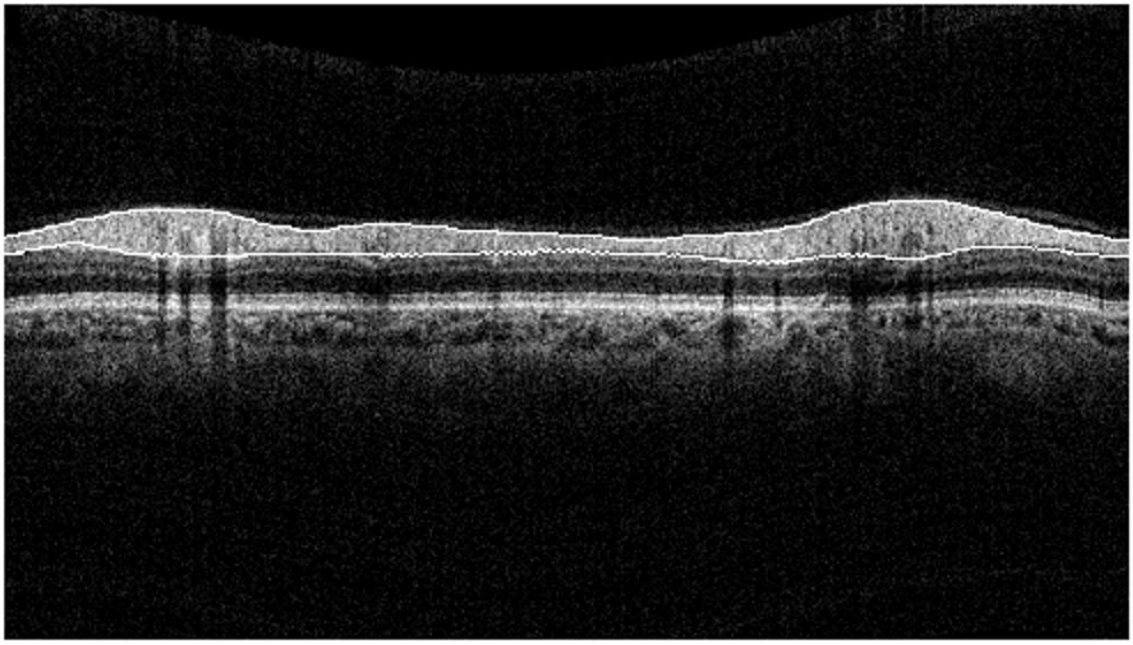

Figure 2.7: An example of a circular optical coherence tomography (OCT) scan around the optic disc. The retinal nerve fiber layer is segmented and the different retinal layers are observed. (Source: Erlangen Nuremberg University Hospital)

localized vision impairments but without relating it to the corresponding ganglion cell group. More advanced methods produce different colors by varying the wavelength of the utilized light. This is used to excite certain types of RGCs and helps to specify the damage occurring to the individual RGCs' classes (e.g. blue objects on a yellow background for stimulating the koniocellular layers). FDT is another test that stimulates a subclass of the M cells. FDT was shown to be able to screen early glaucoma patients and to diagnose moderate and advanced glaucoma by capturing the functional loss in vision [Cell 00]. Sample et al suggested the incorporation of more than one functional test to enhance the glaucoma diagnosis [Samp 00]. Moreover, they pointed out that the structural ONH damage and the functional impairment due to glaucoma have no definite precedence. i.e., in some glaucoma cases visual function loss could be detected before optic disc abnormalities and in other cases the sequence is reversed.

2.5 Conclusion

The glaucomatous impairment progresses slowly due to the underlying mechanisms delaying the patients' awareness of the disease. Early glaucoma detection is essential to limit the irreversible damage to the vision and the visual system. Many issues are still unresolved for glaucoma. Among these issues are the mechanism of progression and the functional or structural damage precedence [Hood 07]. In addition, glaucoma comes in various forms and its pathophysiology is highly complicated.

The availability and development of various eye imaging instruments facilitated the identification of the glaucomatous structural changes. Vision tests and IOP as-

sessment help in identifying glaucoma. However, new directions need to be explored to improve the glaucoma clinical flow and understanding. This could lead to saving the vision of millions of people by adapting the therapy procedures to the new findings. The pathology of glaucoma is not limited the eye but it extends to the visual pathway which is evident from many studies. Thus, a direction with a great potential is the analysis of the visual pathway.

Chapter 3

Diffusion Tensor Imaging

3.1 Introduction

Magnetic resonance imaging is a well established technique in the medical examination routine providing contrast images that distinguish the different tissues. The physical operating principle of the MRI-scanner is based on the properties of the water protons (hydrogen nuclei). The human body consists to a large extent of water molecules. The protons have a net electric charge. Moreover, they rotate inducing a magnetic field. The orientations of the spins are random. Thus, the average magnetic field from spins in a region is approximately zero as spins having different directions cancel each other out. The MRI-scanner utilizes large magnets to align the spins producing a measurable net magnetic field. At saturation, the spins are either in phase or out of phase with the applied magnetic field. An electromagnetic radio frequency (RF) pulse is used. The frequency of the pulse is equal to the precession frequency (Larmor frequency) of the protons. Therefore, its energy is absorbed by the spins elevating them to higher energy states. After the pulse duration, the energy is retransmitted in the form of photons. The rate at which the energy is lost depends on the spin-spin interaction. This can be used to produce relaxation time (T2) weighted images. MRI-images can also be weighted by the rate at which the strength of the net magnetic field parallel to the main applied field is restored after the RF-pulse application (T1-weighting). This reflects the interaction between the spin and the surrounding medium, the tissues. Proton density images have intensities that are related to the concentration of protons in the captured region. Many comprehensive materials exist that describe the foundation of MRI [Tala 91, Lian 00].

The conventional MRI has proven high capabilities in identifying the different tissues in the brain. Various techniques have been suggested to separate the main structures in the brain such as the white matter, the gray matter, and the cerebrospinal fluid [Bala 10]. However, the contrast sensitivity of MRI depends on the tissue type. Therefore, the contrast alone can not be utilized to parcellate the fiber bundles within the white matter. A commonly used approach to overcome this problem and to segment the individual fiber bundles is by incorporating prior anatomical knowledge [Cabe 11]. This knowledge is usually in the form of a preconstructed labeled atlas. The MRI brain images are aligned to the atlas and the labels are assigned to the registered regions. Despite the effectiveness of this approach, the architecture

of the white matter can not be fully resolved. This is due to the high complexity of the cerebral white matter. Taking a closer look at the anatomy of the white matter reveals that it is divided into fiber bundles. A fiber bundle, alternatively called fiber tract or fascicles, is a set of fibers grouped together. The white matter fibers are comprised of axons. The axons are flexible and have cylindrical shapes. The function of the axons is to transport neuronal signals between the neurons, the primary components of the central nervous system that are responsible for information exchange within the human body. In the white matter, the axons are coated with a layer called the myelin sheath [Kueh 03]. In order to know how the structure of the white matter is organized, knowledge is needed about the orientation and the course of the fiber tracts. This requires more information than the one-dimensional intensity provided by the conventional MRI.

By altering the MRI acquisition protocol, images weighted with diffusion can be obtained. A profile describing the molecular displacement within a region can be measured. The simplest and most clinically used model of this random motion is the diffusion tensor. The orientation of the fibers in the brain and the properties of the diffusion process are among the valuable data that are derived from the DTI-data. This complicated type of data created the opportunity to highly advance the neuroimaging field. Fiber reconstruction and their impact on the clinical applications is one of the major achievements made possible only by DTI.

3.2 Diffusion

The physical phenomenon behind DTI is the Brownian motion. The Brownian motion refers to the random displacement of molecules in a fluid medium discovered by Robert Brown in 1827. The molecules undergo a random walk due to continuous collisions from neighboring molecules. This results in a net drift even in a medium containing a single molecular type (e.g., water) which is called self-diffusion. Depending on the boundaries surrounding the random movement of particles, the molecules can have a preferential effective direction. This is called anisotropic diffusion which occurs within the white matter fibers. The cell membranes and myelin sheaths surrounding the axons act as tubes guiding the drifting particles within the axons. Thus, they limit the motion in the direction perpendicular to the axons while increasing the average displacement along the axons resulting in high anisotropy. The diffusion of water-like molecules can be used to identify the fiber orientation which coincides with the average shift. So, the microstructure of the brain white matter can be depicted. In the absence of bounding tissues, the particles can move freely in all directions with equal probability leading to isotropic diffusion.

The mathematical relation between the particle net displacement vector ($\mathbf{R}$) and the diffusion time (τ) was formulated by Einstein [Eins 05]. For the isotropic diffusion case, the equation is given by

$$D_{iso} = \frac{1}{6\tau}\langle \mathbf{R}^T \cdot \mathbf{R} \rangle \tag{3.1}$$

where D_{iso} is a scalar constant called the diffusion coefficient, T is the transpose, and $\langle ... \rangle$ is the ensemble mean.

In the anisotropic case, the previous formulation can be extended to reflect the directionality information. Modeling the probability of a particle at position $\mathbf{r_0}$ to diffuse to position $\mathbf{r}$ ($\mathbf{R} = \mathbf{r} - \mathbf{r_0}$) after a time τ by a normal distribution $p(\mathbf{r}|\mathbf{r_0}, \tau)$ leads to Equation 3.2.

$$p(r|r_0, \tau) = \frac{1}{\sqrt{(4\pi\tau)^3|D|}} e^{-\frac{(\mathbf{r}-\mathbf{r_0})^T \cdot D^{-1} \cdot (\mathbf{r}-\mathbf{r_0})}{4\tau}} \tag{3.2}$$

where $|...|$ is the determinant.

The diffusion tensor is the generalized diffusion coefficient in the anisotropic case which is the covariance matrix of the process. The general form of the relation in Equation 3.1 becomes

$$D = \begin{pmatrix} D_{xx} & D_{xy} & D_{xz} \\ D_{yx} & D_{yy} & D_{yz} \\ D_{zx} & D_{zy} & D_{zz} \end{pmatrix} = \frac{1}{6\tau} \langle \mathbf{R} \cdot \mathbf{R}^T \rangle \tag{3.3}$$

As seen from the above equation, the diffusion coefficient is represented by a second rank tensor to account for the directional dependency of the anisotropic diffusion.

3.3 Diffusion Weighted Imaging (DWI)

The MRI-images can be modulated by the molecular drift of particles. A pulsed-gradient spin-echo (PGSE) acquisition protocol proposed by Stejskal-Tanner is utilized to produce MRI-images with intensities correlated to the amount of diffusion along the sensitizing gradient [Stej 65]. Two gradient pulses with the same strength and opposite directions are inserted in the spin-echo MRI measuring sequences. The first gradient ($\mathbf{g}$) is applied after the 90^0 defocusing pulse and before the 180^0 refocusing pulse. The reversed gradient pulse with a duration δ follows the refocusing pulse. The time difference between the application of the two gradient is $\triangle$ and is equally divided around the 180^0 pulse. If the spins subjected to the applied gradients are static relative to the gradient direction, the two gradient pulses should ideally cancel each other out. Thus, the original MRI signal without the diffusion encoding gradients is not changed. In case of spin shift, the displaced spins will encounter different gradient strengths in their original position and their location after self-diffusion. This will introduce a phase shift at this location leading to attenuation of the measured signal. This signal attenuation is related to the diffusion coefficient by the following equation known as the Stejskal-Tanner equation [Stej 65]

$$S_k(\mathbf{r}) = S_0(\mathbf{r}) e^{-b\hat{\mathbf{g}}_\mathbf{k}^T \cdot D(\mathbf{r}) \cdot \hat{\mathbf{g}}_\mathbf{k}} \tag{3.4}$$

where $\mathbf{r}$ is the position at which the signal is measured, $k = 1$ to N is the index of the applied gradient $\mathbf{g_k}$, $\hat{\mathbf{g}}_\mathbf{k} = \mathbf{g_k}/\|\mathbf{g_k}\|$ is the normalized gradient direction, S_k and S_0 are the diffusion weighted signal and the non-diffusion weighted signal, respectively. D is the diffusion tensor. In case of orientation independent diffusion, D is reduced to a scalar called the apparent diffusion coefficient (ADC) and the exponential term becomes e^{-bD}. The scalar b is the diffusion weighting factor and it is proportional to the squared magnitude of the gradient. Thus, higher gradient strength leads to

greater signal reduction and in turn more contrast. The time allowed for the molecules to diffuse before measurement is also proportional to b. Equation 3.5 indicates the dependencies of b. In order to calculate the diffusion tensor, the MRI-signal in the absence of the diffusion gradients needs to be measured. This is equivalent to setting $b = 0$ in Equation 3.4.

$$b_k = \gamma^2 \delta^2 \left(\triangle - \frac{\delta}{3} \right) \|\mathbf{g_k}\|^2 \tag{3.5}$$

where γ is the gyromagnetic ratio relating the external applied magnetic field to the Larmor frequency and $\|...\|$ is the vector norm.

The white matter organization affects the measured diffusion coefficient which depends on the angle between the diffusion gradients and the fiber tracts. For example, if the applied gradient at a certain location is aligned with the orientation of a coherent fiber bundle, the measured signal reduction and in turn the ADC should be maximized corresponding to the highly anisotropic diffusion for this gradient pair. As the angle increases, ADC decreases for this location. This diffusion weighting procedure could be repeated along many directions to obtain a diffusion profile. This profile at a voxel is described by the gradient direction and the corresponding ADC. Examples of diffusion weighted images of a brain slice and the encoding gradients are demonstrated in Figure 3.1. The acquisition of diffusion weighted images along many gradients is time consuming. Therefore, other scanning sequences are also used that reduce the scanning time such as echo planar imaging (EPI) [Bamm 99].

3.4 Modeling the Diffusion Process: The Diffusion Tensor

The result from the DWI acquisitions is a set of volume images. The individual three dimensional (3D) images correspond to a scan along a certain diffusion encoding gradient direction. Each 3D-image is divided into voxels where each voxel corresponds to a volume in the scanned space. Thus, the measured ADC-value is the average diffusion coefficient within a specified volume. At the voxel level, the diffusion process is sampled by the ADC values and the encoding directions pairs. The most common mathematical formalism for extracting quantitative data from the diffusion process is the diffusion tensor [Bass 94]. The average displacement within a voxel is modeled by a Gaussian process (Equation 3.2) with zero mean and represented by the diffusion tensor. The tensor inherits the properties of the covariance matrix. Thus, it is a 3×3 matrix that is symmetric and positive-definite. Due to the symmetry, dual off-diagonal elements are equal (e.g., $D_{xy} = D_{yx}$). Thus, six parameters need to be estimated in order to completely describe the Gaussian approximation of the diffusion process. These are the three diagonal elements and the three upper (or lower) off-diagonal elements.

The calculation of the six individual elements of the diffusion tensors requires at least six diffusion weighted images acquired along six non-collinear directions. In addition, a non-diffusion weighted image is necessary to compute the MRI-signal reduction. A linear system of equations can be derived from the Stejskal-Tanner

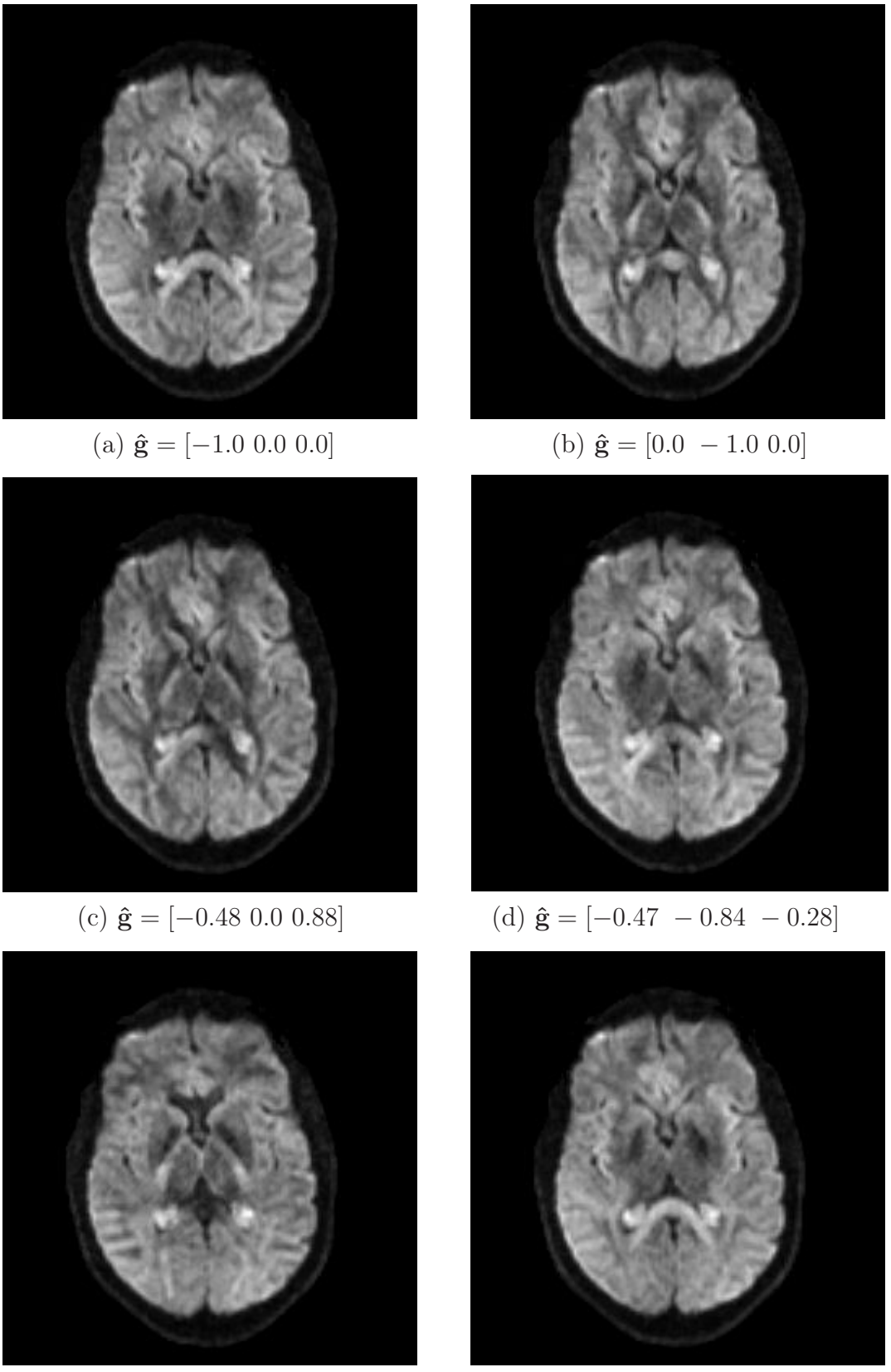

(a) $\hat{\mathbf{g}} = [-1.0\ 0.0\ 0.0]$ (b) $\hat{\mathbf{g}} = [0.0\ -1.0\ 0.0]$

(c) $\hat{\mathbf{g}} = [-0.48\ 0.0\ 0.88]$ (d) $\hat{\mathbf{g}} = [-0.47\ -0.84\ -0.28]$

(e) $\hat{\mathbf{g}} = [-0.55\ -0.43\ -0.71]$ (f) $\hat{\mathbf{g}} = [-0.11\ -0.27\ -0.96]$

Figure 3.1: Examples of diffusion weighted images of the same axial brain slice acquired along six non-collinear diffusion synthesizing gradients

equation where each gradient application results in a linear equation with regard to the diffusion tensor elements. Typically more than six DWI-images are obtained and the linear system becomes the following over-determined system of equations

$$\begin{pmatrix} \hat{g}_{1x}^2 & \hat{g}_{1y}^2 & \hat{g}_{1z}^2 & 2\hat{g}_{1x}\hat{g}_{1y} & 2\hat{g}_{1x}\hat{g}_{1z} & 2\hat{g}_{1y}\hat{g}_{1z} \\ \hat{g}_{2x}^2 & \hat{g}_{2y}^2 & \hat{g}_{2z}^2 & 2\hat{g}_{2x}\hat{g}_{2y} & 2\hat{g}_{2x}\hat{g}_{2z} & 2\hat{g}_{2y}\hat{g}_{2z} \\ \vdots & \vdots & \vdots & \vdots & \vdots & \vdots \\ \hat{g}_{nx}^2 & \hat{g}_{ny}^2 & \hat{g}_{nz}^2 & 2\hat{g}_{nx}\hat{g}_{ny} & 2\hat{g}_{nx}\hat{g}_{nz} & 2\hat{g}_{ny}\hat{g}_{nz} \end{pmatrix} \cdot \begin{pmatrix} D_{xx} \\ D_{yy} \\ D_{zz} \\ D_{xy} \\ D_{xz} \\ D_{yz} \end{pmatrix} = \frac{-1}{b} \begin{pmatrix} \ln\left(\frac{S_1}{S_0}\right) \\ \ln\left(\frac{S_2}{S_0}\right) \\ \vdots \\ \ln\left(\frac{S_n}{S_0}\right) \end{pmatrix} \tag{3.6}$$

where $\hat{g}_{ix}$, $\hat{g}_{iy}$, and $\hat{g}_{iz}$ are the x, y, and z components of the normalized i^{th} gradient direction $\hat{\mathbf{g}}_\mathbf{i}$, respectively.

The above linear system is in the form of $G \cdot \mathbf{D_v} = \frac{-1}{b}\mathbf{S}$ where G is the matrix containing the gradients, $\mathbf{D_v}$ is the vector form of the six components of the diffusion tensor, and $\mathbf{S}$ is the vector containing the ln of the attenutation ratio along the applied gradients. This equation system has a unique solution in case of equal number of equations and unknowns (i.e., n = 6). The solution could be simply obtained by inversing the non-singular G-matrix and multiplying the result by the right hand side. In case of an over-determined system, least square methods should be incorporated to obtain the solution. Singular value decomposition (SVD) is utilized in this work to solve the linear system of equations [Skar 00]. This is performed by calculating the pseudo-inverse matrix ($G^\dagger$) from the decomposed matrix G. Then, the tensor elements are estimated by multiplying $G^\dagger$ by $\mathbf{S}$-vector divided by -b. The following equations show the mathematical formulation of the solution procedure

$$G = U \cdot \Sigma \cdot V^T \tag{3.7}$$

where U is an n $\times$ n matrix and its columns are the eigenvectors of the matrix $G.G^T$, Σ is an n $\times$ 6 diagonal matrix with its diagonal containing the singular values of the matrix $G^T.G$, and V is an 6 $\times$ 6 matrix and its columns are the eigenvectors of the matrix $G^T.G$.

$$G^\dagger = V \cdot \Sigma^\dagger \cdot U^T \tag{3.8}$$

where $\Sigma^\dagger$ is an 6 $\times$ n diagonal matrix. The reciprocals of the diagnonal elements of Σ^T are the diagonal elements of $\Sigma^\dagger$.

$$\mathbf{D_v} = \frac{-1}{b} G^\dagger \cdot \mathbf{S} \tag{3.9}$$

The diffusion tensor components are estimated voxelwise. The frame of reference for the DWI-images and diffusion tensors is the scanner coordinate system. The spectral decomposition of the diffusion tensor can be utilized to determine the local fiber coordinate system. The local frame of reference at each voxel has three orthonormal axes. The first axis should ideally coincide with the fiber orientation at this location. The other two axes lie in the plane perpendicular to the major axis spanning the

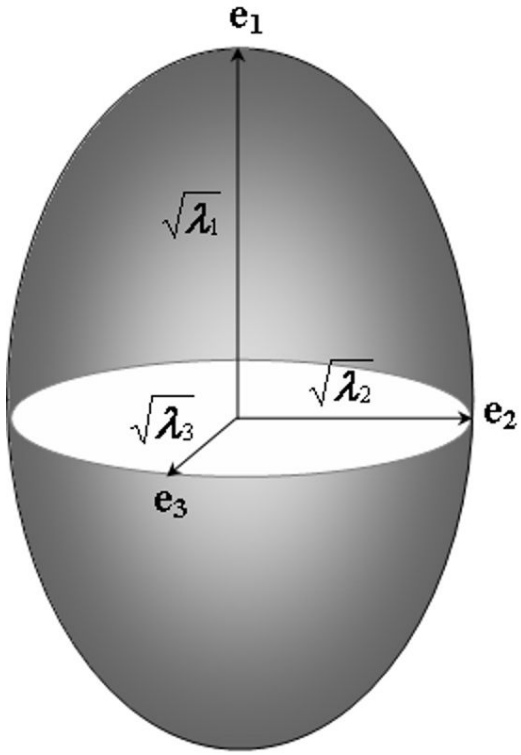

Figure 3.2: The geometrical representation of the diffusion tensor as an ellipsoid. The spectral components of the diffusion tensor are shown by the three eigenvalues and eigenvectors.

fiber cross section. The eigenvalue decomposition of the diffusion tensor yields three eigenvalues and three eigenvectors as shown in Equation 3.10.

$$D = \left[\begin{array}{ccc} \mathbf{e_1} & \mathbf{e_2} & \mathbf{e_3} \end{array} \right] \cdot \begin{pmatrix} \lambda_1 & 0 & 0 \\ 0 & \lambda_2 & 0 \\ 0 & 0 & \lambda_3 \end{pmatrix} \cdot \left[\begin{array}{ccc} \mathbf{e_1} & \mathbf{e_2} & \mathbf{e_3} \end{array} \right]^T \tag{3.10}$$

where $\mathbf{e_1}$, $\mathbf{e_2}$ and $\mathbf{e_3}$ are the diffusion tensor eigenvectors corresponding to λ_1, λ_2 and λ_3 which are the diffusion tensor eigenvalues in a descending order.

An ellipsoid is a widely used graphical representation of the diffusion tensor. The ellipsoid has its center at the voxel position. The three orthogonal main axes of the ellipsoid have the same directions as the three eigenvectors of the diffusion matrix. The lengths of these axes are proportional to the square root of their associated eigenvalues as depicted in Figure 3.2. Additionally, each point on the ellipsoidal surface has the same probability of molecular displacement.

The eigenvector corresponding to the largest eigenvalue is referred to as the principal diffusion direction (PDD). This vector plays an important role in identifying the fiber structure as it contains the information related to the fiber orientation. Moreover, it provides an alternative way of visualizing the DTI-data rather than plotting the 3D-ellipsoids in the 3D-space. The magnitude of the x, y, z-Cartesian components of the PDD are used as the red, green, and blue colors of an RGB-image, respectively [Paje 99]. So, the main diffusion direction can be represented in a simple

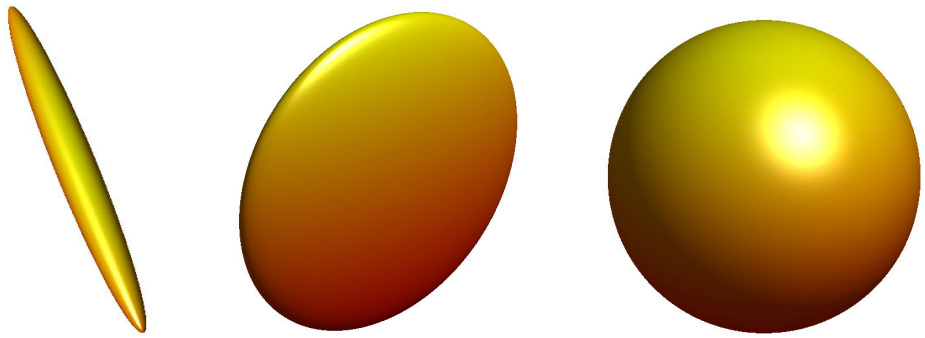

Figure 3.3: The degree of diffusion anisotropy ranging from highly anisotropic (linear tensors) in coherent medium to isotropic (spherical tensors) in fluid medium.

manner. Typically, the direction weighted images are multiplied by an anisotropy index to reduce the importance of the direction information in near isotropic voxels. In the color-coded diffusion direction images included in this thesis, the red color refers to the left-right direction, the green color is the anterior-posterior direction, and the superior-inferior orientation is represented by the blue color. The images are weighted by the fractional anisotropy index that will be described in Section 3.5.2.

In highly organized tissue structures, the diffusion tensor has a cigar like shape. This structure reflects a greater diffusion along the fiber direction and, so, the diffusion ellipsoid elongates with the extreme at $\lambda_1 > 0$ and $\lambda_2 = \lambda_3 = 0$. In the absence of bounding structures, the molecules are free to diffuse in any direction leading to a diffusion iso-surface with a spherical shape as demonstrated in Figure 3.3. This corresponds to $\lambda_1 = \lambda_2 = \lambda_3$ at the perfectly isotropic diffusion case.

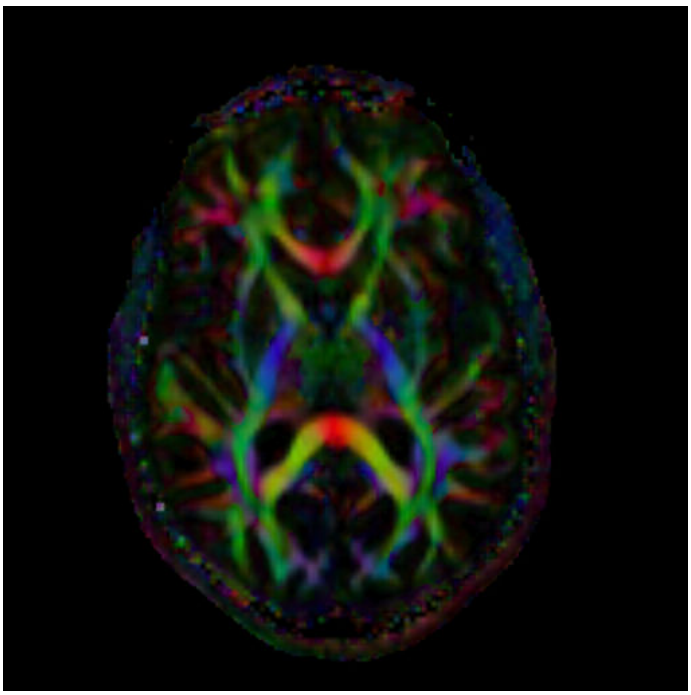

Figure 3.4: A principal diffusion direction color coded image of an axial brain slice. The red, green, and blue colors correspond to the left-right, anterior-posterior, and superior-inferior directions. The image is weighted with the fractional anisotropy.

The diffusion tensor model involves an averaging of the diffusion profile performed on a certain volume, the voxel size. This volume typically contains large number of axons, considering the currently achievable DTI-image resolutions. The axons within a voxel could be homogenous or heterogeneous depending on the intravoxel fiber architecture. For example, if all the fibers within a voxel are belonging to a coherent fiber bundle, then the fiber orientation should be aligned with the major axis of the diffusion ellipsoid in this voxel. On the other hand, if a voxel contains intersecting or branching fibers, the PDD will not reflect the fiber orientation. These fiber situations are referred to as intravoxel orientational heterogeneity (IVOH) [Tuch 02]. More complicated models have been suggested to better resolve the aforementioned problematic situations. Higher order tensors are proposed to approximate the diffusion profile that ranges from two-tensor to generalized tensor models [Liu 04, Pele 06, Schu 08]. Fiber orientation density function is an alternative to the diffusion tensors [Tour 04, Schu 08]. High-angular-resolution diffusion and Q-ball imaging are different approaches that can resolve intravoxel fiber populations [Tuch 02, Tuch 04]. However, the proposed models are complex and require DWI-images along a large number of synthesizing gradients. This increases the acquisition time in the uncomfortable MRI-scanner significantly and, therefore, the diffusion tensor remains the most adopted model in the clinical routine.

3.5 Diffusion Tensor Imaging Derived Measures

Diffusion tensor imaging provides rich information describing various aspects of the diffusion process. In addition, the fiber orientation can generally be identified from the diagonalization of the diffusion tensor. Indices are derived from the tensors that are related to the characteristic of the underlying fiber architecture. These indices have been utilized in medical studies and were shown to correlate to various neurological diseases. In this section, we give an overview of the most commonly used DTI-measures. Some of these measures will be used in subsequent chapters as glaucoma abnormality features. We classify them into three main categories: Diffusivity measures, anisotropy parameters, and coherence indices.

3.5.1 Diffusivity Measures

This class includes parameters that quantify the voxelwise diffusivities. They are calculated from the eigenvalues of the diffusion tensor. Therefore, they are rotationally invariant. i.e., they are independent from the diffusion tensor ellipsoid orientation in the space. The mean diffusivity (MD) is the average isotropic part of the diffusion within a voxel [Bass 96]. It is the mean of the three eigenvalues or equivalently one third of the trace of the diffusion tensor as indicated by Equation 3.11. It is thought to be related to the bounding medium and the freedom of the particles to move, which can be significantly affected in pathological cases such as the presence of lesions.

$$MD = \hat{\lambda} = \frac{tr(D)}{3} = \frac{D_{xx} + D_{yy} + D_{zz}}{3} = \frac{\lambda_1 + \lambda_2 + \lambda_3}{3} \tag{3.11}$$

The axial diffusivity (AD) represents the estimated amount of diffusion along the fiber direction. The fiber orientation is assumed to be in the direction of the PDD. Thus, AD is the largest eigenvalue (λ_1) as Equation 3.12 shows. In other words, AD is half the length of the main axis of the diffusion tensor ellipsoid. Higher values of AD should be expected for coherent fiber bundles. In this case, the molecules are guided by the fibers which increase the probability of displacement longitudinal to the fibers.

$$AD = \lambda_1 \tag{3.12}$$

The average diffusion normal to the PDD is the radial diffusivity (RD). In Equation 3.13, RD is computed by averaging λ_2 and λ_3. This means that RD is the average of the half lengths of the two minor axes of the ellipsoid. The diffusion within a fiber cross section is suggested to be limited by the cell membranes among other restricting objects. This may be reflected in the RD leading to its sensitivity to fiber degeneration processes caused by various neuronal diseases.

$$RD = \frac{\lambda_2 + \lambda_3}{2} \tag{3.13}$$

The diffusivity measures can be visualized as grayscale images reducing the complexity of the tensor ellipsoid. The representation in Figure 3.5 shows the areas with different diffusivities in a brain image with respect to the normalized diffusivity parameters (MD, AD, and RD) in addition to an anatomical image. Moreover, manual inspection can be used to compare healthy and diseased subjects indicating the disease specific regions with changes in the diffusivities.

3.5.2 Anisotropy Parameters

The diffusion captured by DWI ranges from isotropic to anisotropic. This depends on the medium and the regularity of the fibers. In general, non-isotropic Brownian motion is a function of direction. The geometry of the diffusion tenor ellipsoid, more specifically the eccentricity, is an indicator of the deviation degree from the isotropic diffusion. The parameters in this category are proposed to estimate the anisotropy at the voxel scale. The anisotropy measures are functions of the lengths of the axes of the diffusion tensor ellipsoid. The most widely used anisotropy index is the fractional anisotropy (FA). Equation 3.14 defines the mathematical formula for the computation of FA using the diffusion tensor eigenvalues [Bass 96]. For a restriction-free molecular motion, the shape of the diffusion ellipsoid is spherical. This corresponds to equal eigenvalues and FA is zero. The maximum value of FA is one which is reached for completely anisotropic diffusion (i.e., $\lambda_1 > 0$ and $\lambda_2 = \lambda_3 = 0$).

$$FA = \sqrt{\frac{3}{2}} \frac{\sqrt{\left(\lambda_1 - \hat{\lambda}\right)^2 + \left(\lambda_2 - \hat{\lambda}\right)^2 + \left(\lambda_3 - \hat{\lambda}\right)^2}}{\sqrt{\lambda_1^2 + \lambda_2^2 + \lambda_3^2}} \tag{3.14}$$

The relative anisotropy (RA) is another parameter for the diffusion anisotropy. As shown in Equation 3.15, RA is the standard deviation of the eigenvalues (corresponding to the anisotropic part of the diffusion) divided by the trace of the diffusion

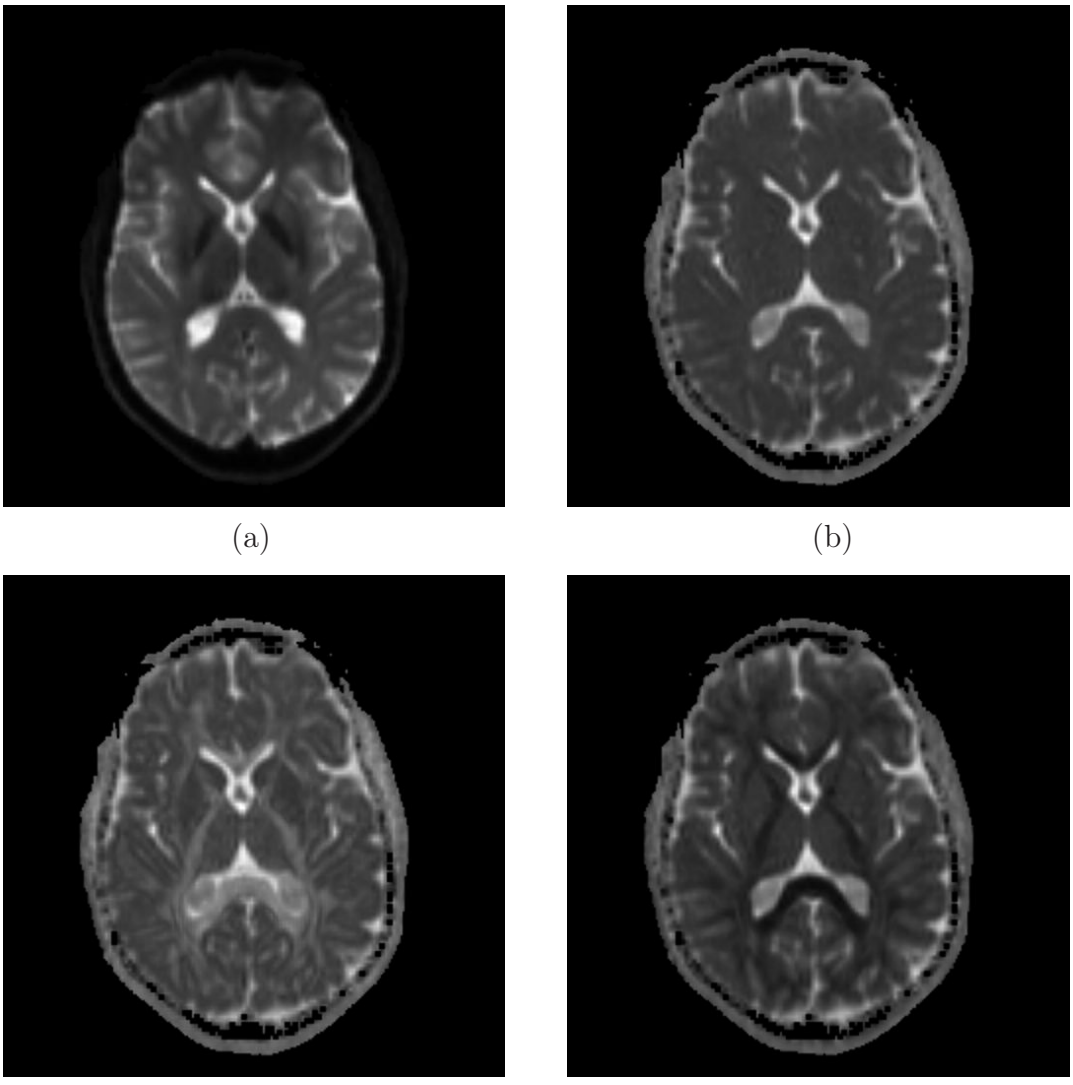

(a) (b)

(c) (d)

Figure 3.5: (a) A non-diffusion weighted MRI axial brain image. Brain images showing the diffusivity maps of the: (b) Mean Diffusivity (MD),(c) Axial Diffusivity (AD), and (d) Radial Diffusivity (RD).

tensor, proportional to the average isotropic diffusion [Bass 96]. FA and RA share a similar nominator and they can be deducted from each other. The range of RA is from 0 (isotropic diffusion) to $\sqrt{2}$ (complete anisotropic diffusion). The anisotropy indices add other possibilities of DTI-data visualization as illustrated in Figure 3.6. The coherent white matter tracts have higher anisotropy, which corresponds to brighter voxels in the FA and RA weighted images.

$$RA = \sqrt{3}\frac{\sqrt{\left(\lambda_1 - \hat{\lambda}\right)^2 + \left(\lambda_2 - \hat{\lambda}\right)^2 + \left(\lambda_3 - \hat{\lambda}\right)^2}}{\lambda_1 + \lambda_2 + \lambda_3} \tag{3.15}$$

The volume of the diffusion tensor ellipsoid is $4\pi\lambda_1\lambda_2\lambda_3/3$. In case of isotropic diffusion, all the axes are equal and the volume becomes $4\pi\hat{\lambda}^3/3$. The ratio between the ellipsoid volume to the volume of the average sphere is called the volume ratio (VR) (Equation 3.16) [Bass 95]. This parameter is also used as an anisotropy measure. Nevertheless, the scale of VR is reversed in comparison to FA and RA. It has a value of one for the isotropic case and a value of zero for infinite anisotropy.

$$VR = \frac{\lambda_1\lambda_2\lambda_3}{\hat{\lambda}^3} \tag{3.16}$$

Indices were developed to distinguish between prolate, oblate, and spherical tensors [West 04]. Prolate tensors (Figure 3.3a) characterize homogeneous regions with high anisotropy and relatively high certainty of fiber orientation coincidence with the PDD. The linear anisotropy index (C_L) given by Equation 3.17 quantifies the degree of the tensor ellipsoid elongation. Intravoxel crossing and branching fibers result in reduced average anisotropy and uncertainty of the underlying fiber orientation. These situations are characterized by oblate tensors (Figure 3.3b). For this type of tensors, the planar anisotropy index (C_P) is proposed. As seen in Equation 3.18, C_P is a weighted difference between the second and third eigenvalues. A perfect planar tensor has $\lambda_1 = \lambda_2, \lambda_3 = 0$ and $C_P = 1$. Finally, near spherical tensors have spherical anisotropy index (C_S)-values of approximately one by setting $\lambda_1 \approx \lambda_2 \approx \lambda_3$ in Equation 3.19.

$$C_L = \frac{\lambda_1 - \lambda_2}{3\hat{\lambda}} \tag{3.17}$$

$$C_P = \frac{2(\lambda_2 - \lambda_3)}{3\hat{\lambda}} \tag{3.18}$$

$$C_S = \frac{3\lambda_3}{3\hat{\lambda}} \tag{3.19}$$

The linear, planar, and spherical anisotropy parameters are used as grayscale intensities for the acquired images (Figure 3.7). The different types of tensors can be detected from the images. The three parameters sum to one. An RGB-image can be generated by weighting each of the three colors with the three parameters. This facilitates the discrimination of voxels by examining the dominant color. All the parameters in this category are derived from the eigenvalues. Therefore, they have the same rotational invariance property as the diffusivity parameters.

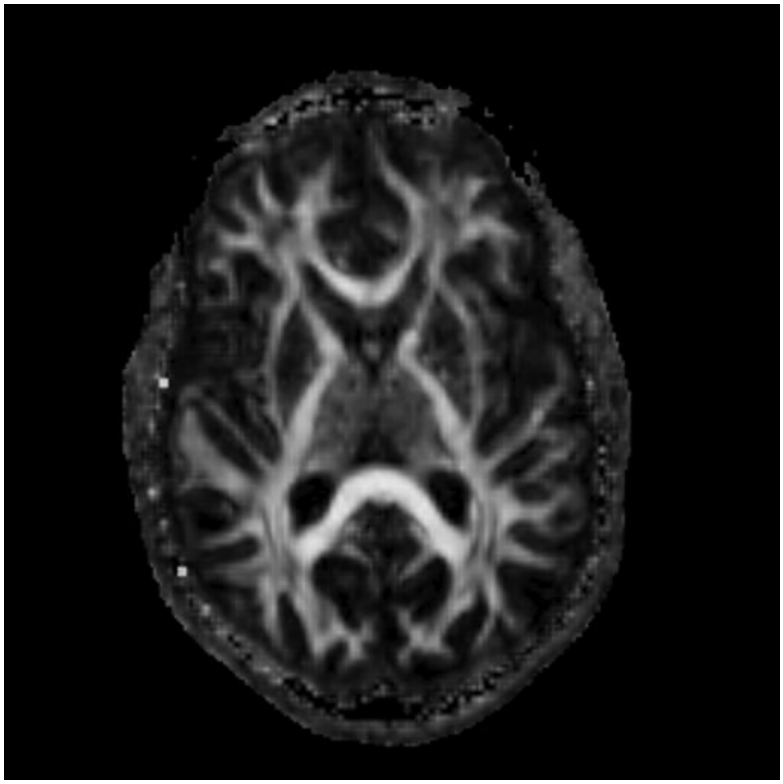

(a) Fractional Anisotropy

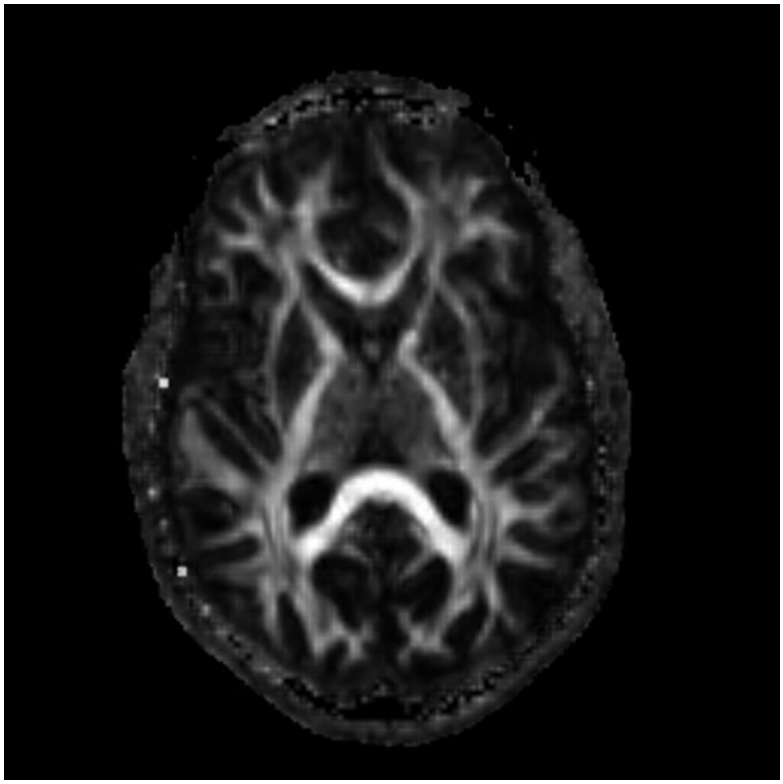

(b) Relative Anisotropy

Figure 3.6: Fractional anisotropy and relative anisotropy shown on an axial brain slice

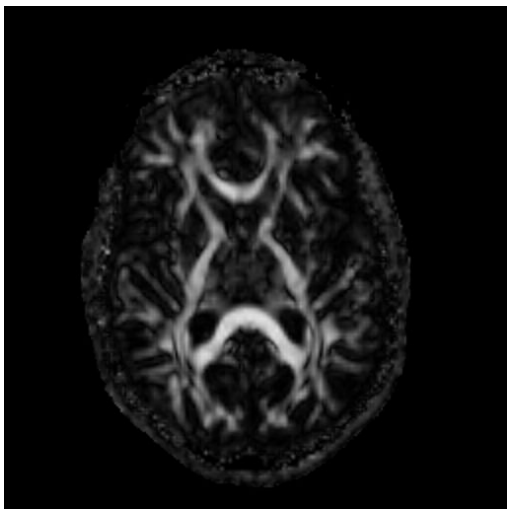

(a) Linear Anisotropy

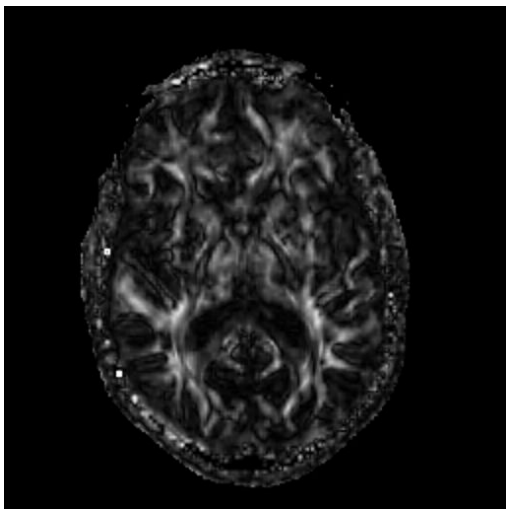

(b) Planar Anisotropy

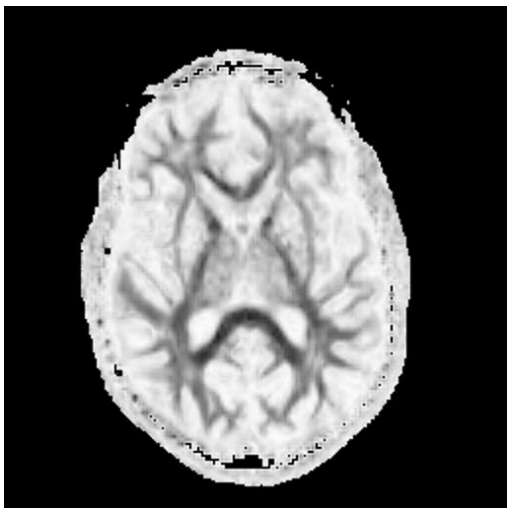

(c) Spherical Anisotropy

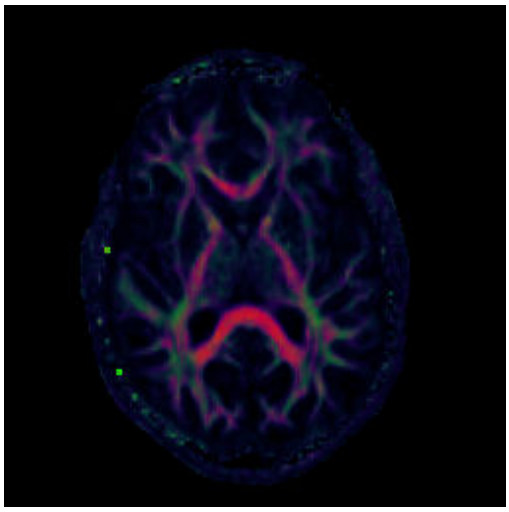

(d) Color Coded Anisotropy

Figure 3.7: Axial brain images of the (a) linear, (b) planar, and (c) spherical anisotropy measures corresponding to tensors with prolate, oblate, and spherical geometry, respectively. An RGB-image representation of the anisotropy parameters C_L (red), C_P (green), and C_S (blue) weighted by FA is shown in sub-image (d).

3.5.3 Coherence Indices

The DTI-derived scalars in the previous class are hypothesized to reflect the coherence of the fibers. However, we discriminate these parameters from the coherence indices. This category utilizes more information than the eigenvalues. This information may include the eigenvalues but also additional information is utilized such as the eigenvectors. Moreover, although the coherence indices are computed voxelwise, the computation involves a neighborhood around the voxel under consideration. The coherence index (CI) examines the degree of PDD alignment with its neighboring voxels [Klin 99]. The angles between the adjacent vectors and the PDD at the examined voxel are estimated from their dot product. Equation 3.20 identifies the CI in 2D-images where the neighborhood is 3×3. This could be extended to 3D-images in a straightforward manner. If the 8 neighboring voxels belong to a regular fiber bundle with a dominant orientation, the standard deviation of the PDD in the neighborhood should be minimal. This leads to a maximum coherence.

$$CI(i,j) = \frac{1}{8} \sum_{k=i-1}^{i+1} \sum_{l=j-1}^{j+1} \mathbf{e_1}(i,j) \cdot \mathbf{e_1}(k,l) - 1 \tag{3.20}$$

Pierpaoli et al. proposed a more general coherence parameter called the lattice index (LI) [Pier 96b, Skar 00]. LI uses all the orientational information from the three eigenvectors. In addition, it weights each vector with the corresponding eigenvalue providing a more comprehensive measure that uses the complete tensor information.

3.6 Fiber Identification

The direction vectors within the diffusion tensor and their relation to fiber organization in the brain open new possibilities in the field of neuroanatomy. The fiber pathways can be identified in the brain space in-vivo which is a unique advantage exclusive to DTI. The complex data and brain anatomy pose many challenges in capturing the anatomical details of the white matter structure. This encouraged many researchers to address this problem using different approaches. Therefore, a wide spectrum of fiber tracking algorithms exists, famously known as tractography. The methods tested on real DTI-data suffer from the lack of a ground truth which limits the effectiveness of the validation. Therefore, synthetic DTI-data are generated to test and compare the different tracking algorithms [Leem 03, Peng 09, Berg 05, Clos 09]. Some of these phantoms attempt to simulate the complex fiber situations. Quantification of the errors is also possible. In this section, we review the state of the art of the algorithms developed for determining the white matter fibers' pathways. The tractography methods are classified into streamline tractography, connectivity maps, and segmentation. Examples from each group are illustrated and the techniques are briefly described. More details and other algorithms can be found in fiber tracking reviews [Bass 02, Mori 02, Bamm 03, Zhan 05, Nuci 07].

3.6.1 Streamline Tractography

The fiber identification in this category follows a straightforward and intuitive approach. Streamline techniques start with an initial voxel, usually referred to as a seed point, or a region at which the fiber construction begins. The seed point is placed by experts on the targeted tract. The main idea is to regard the individual fibers as integral curves in the space. The general problem can then be stated as [Bass 00]

$$\frac{d\mathbf{s}(t)}{dt} = \mathbf{m}(t) \tag{3.21}$$

where $\mathbf{m}$ is the unit tangent of the integral curve $\mathbf{s}$ at location t. In homogenous tracts, the tangent to the integral path should be parallel to PDD. i.e., $\mathbf{m}(t) = \mathbf{e_1}(\mathbf{s}(t))$.

One of the earliest attempts to construct the fibers were proposed by Conturo et al. [Cont 99]. The tracking is performed by following the PDD starting from the seed point. This is equivalent to an Euler's integration of the fiber curve. Smaller integration steps than the acquired DTI-resolution could be used to reduce the accumulation error. This requires estimating the diffusion tensor at non-grid locations by interpolation. The process continues until some stopping criteria are satisfied. In this case, the criterion was a lower limit for the degree of anisotropy as an indication of arriving at a gray matter tissue. Due to the symmetry of the diffusion tensor, the diffusion could be either in the direction of the PDD or its opposite. Therefore, the tracking starts bidirectionally with the PDD reversed if the pathways turns more than 90^0. The numerical solution of Equation 3.21 can then be written as

$$\mathbf{s}(t+1) = \mathbf{s}(t) + \triangle t \times \mathbf{e_1}(\mathbf{s}(t)) \tag{3.22}$$

where $\triangle t$ is the integration step.

A more robust integration method with less accumulation error is the Runge-Kutta (RK). Higher order variants of RK includes second and fourth order have been suggested [Bass 00, Tenc 02]. The fourth order RK estimates the next point on the pathway from the Equation

$$\mathbf{s}(t+1) = \mathbf{s}(t) + \triangle t \times \mathbf{V}(t+1) \tag{3.23}$$

where

$$\mathbf{V}(t+1) = \frac{\mathbf{k_1}}{6} + \frac{\mathbf{k_2}}{3} + \frac{\mathbf{k_3}}{3} + \frac{\mathbf{k_4}}{6} \tag{3.24}$$

$$\mathbf{k_1} = \frac{\mathbf{V}(t) \cdot \mathbf{e_1}(\mathbf{s}(t))}{|\mathbf{V}(t) \cdot \mathbf{e_1}(\mathbf{s}(t))|}\mathbf{e_1}(\mathbf{s}(t)) \tag{3.25}$$

$$\mathbf{k_2} = \frac{\mathbf{V}(t) \cdot \mathbf{e_1}(\mathbf{s}(t) + \triangle t/2 \times \mathbf{k_1})}{|\mathbf{V}(t) \cdot \mathbf{e_1}(\mathbf{s}(t) + \triangle t/2 \times \mathbf{k_1})|}\mathbf{e_1}(\mathbf{s}(t) + \triangle t/2 \times \mathbf{k_1}) \tag{3.26}$$

$$\mathbf{k_3} = \frac{\mathbf{V}(t) \cdot \mathbf{e_1}(\mathbf{s}(t) + \triangle t/2 \times \mathbf{k_2})}{|\mathbf{V}(t) \cdot \mathbf{e_1}(\mathbf{s}(t) + \triangle t/2 \times \mathbf{k_2})|}\mathbf{e_1}(\mathbf{s}(t) + \triangle t/2 \times \mathbf{k_2}) \tag{3.27}$$

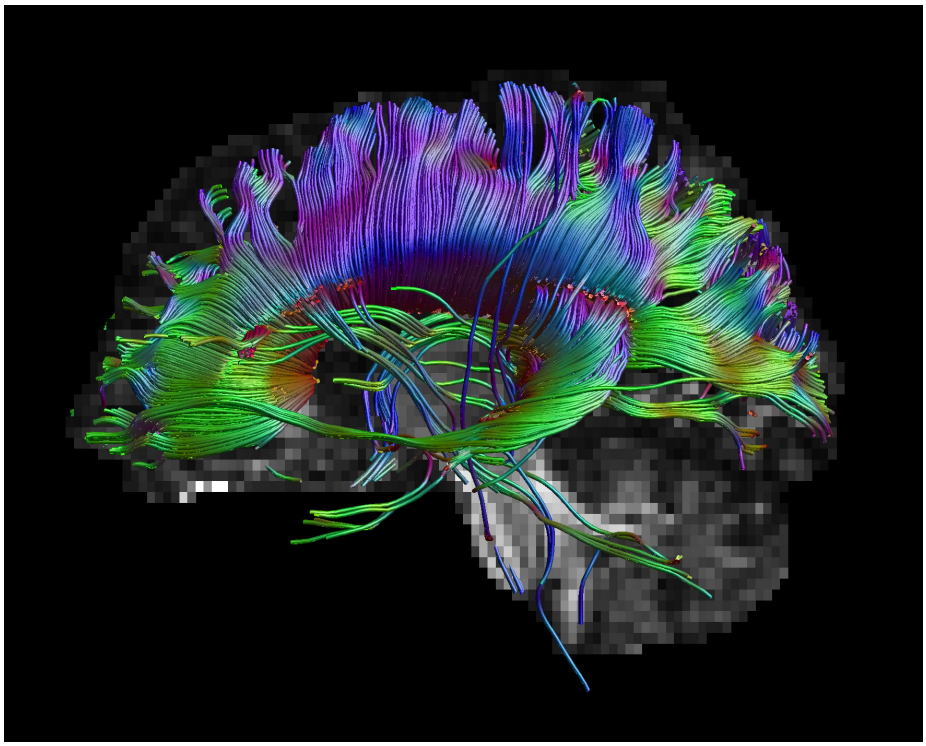

Figure 3.8: Streamline tractography example with the Runge-Kutta implementation in the ExploreDTI software tool [Leem 09].

$$\mathbf{k_4} = \frac{\mathbf{V}(t) \cdot \mathbf{e_1}(\mathbf{s}(t) + \triangle t \times \mathbf{k_3})}{|\mathbf{V}(t) \cdot \mathbf{e_1}(\mathbf{s}(t) + \triangle t \times \mathbf{k_3})|} \mathbf{e_1}(\mathbf{s}(t) + \triangle t \times \mathbf{k_3}) \tag{3.28}$$

This implementation of the fourth order Runge-Kutta has the advantage that the angle between neighboring voxels never exceeds 90^0. So, the solution of the PDD sign problem is inherently included in the implementation. In addition to the RA, this method uses a maximum change of curvature to terminate the tracking. An example of an RK based fiber tracking is shown in Figure 3.8 using the ExploreDTI software tool [Leem 09].

The diffusion tensor deflection (TEND) tractography is another example of this class [Laza 03]. This algorithm uses the diffusion tensor to limit the curvature change and, thus, ensures a smooth fiber construction. By multiplying the tensor with the incoming vector from the previous step ($\mathbf{v_{in}}$), the result is an output vector ($\mathbf{v_{out}}$) that is deflected as given by Equation 3.29. The steering of $\mathbf{v_{out}}$ will depend on the geometry of the diffusion tensor. For example, if $\mathbf{v_{in}}$ is parallel to the PDD at the current voxel, $\mathbf{v_{out}}$ will be in the same direction as $\mathbf{v_{in}}$. However, in general the amount of deflection will depend on the tensor anisotropy and the angle between the PDD and the incoming vector.

$$\mathbf{v_{out}} = D \cdot \mathbf{v_{in}} \tag{3.29}$$

Several streamline fiber tracking methods have been introduced [Bass 02, Bamm 03, Zhan 05]. Streamline tractography suffers from propagation errors that accumulate

while traversing the whole tract. Moreover, this category is unable to resolve fiber crossings or branching as it follows a specific direction. The stopping criteria are additional challenges, because voxels with IVOH could have reduced anisotropy and ambiguous fiber orientation.

3.6.2 Connectivity Maps

The aforementioned problems in tractography and the diffusion tensor model [Tour 02] motivated studies to estimate the uncertainties in the constructed fibers [Behr 03]. The degree of confidence associated with the anatomical connections suggested the utilization of probabilistic tractography techniques. This type of tractography generates connectivity maps. In contrast to deterministic fiber tracking where the voxels are connected in a straightforward manner, connectivity maps give a probability that two voxels are linked together. A connectivity map generated by the ExploreDTI tool is shown in Figure 3.9.

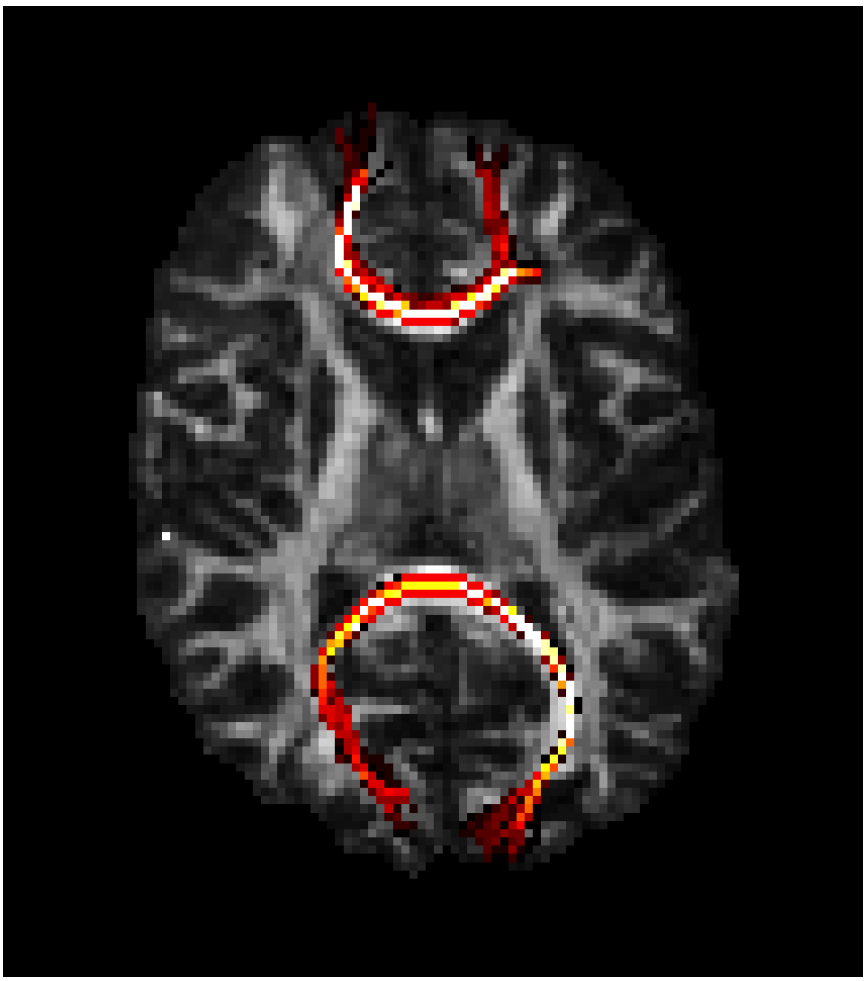

Figure 3.9: A connectivity map generated by ExploreDTI starting with a seed region placed on the corpus callosum. Yellow colors reflect higher degrees of confidence than red colors. The tracking is performed by a wild bootstrap algorithm [Jone 08].

The random vector perturbation (RAVE) tractography is based on perturbing the PDD [Laza 02]. The perturbation is related to the anisotropy of the diffusion tensor. It is modeled along the ellipsoid's two minor axes by Gaussian distributions with zero means. The standard deviation is proportional to λ_2/λ_1 along $\mathbf{e_2}$ and λ_3/λ_1 along $\mathbf{e_3}$. Tracts are constructed using the perturbed vectors from a common seed point leading to a group of tracts. The ratio between the number of tracts connecting two points (or regions) to the total number of tracts is the estimated connection probability. A non-parametric probabilistic approach uses bootstrap techniques was proposed by Lazar and Alexander [Laza 05]. From a collection of repeated DTI-measurements, samples are drawn randomly on a voxelwise basis and the bootstrap intensity value is their average. The diffusion tensors are extracted for each bootstrap iteration. The set of DTI-images are utilized to create a distribution of fiber pathways starting from the same location. The connection probability is calculated in an identical manner to the RAVE method.

Other algorithms that belong to this class were also suggested [Park 03, Yoru 05, Jone 08]. This category allows for the intersection and divergence of fibers. However, a major issue in connectivity maps is that they present probabilities rather than tracts. To overcome this issue, usually a threshold on the probabilities is set. The connections above this threshold are considered actual tracts while all other connections are excluded. This requires a careful selection of the threshold and an expert's intervention. Practically, this solves the problem only partially as undesired tracts remain or desired tracts are removed.

The fast marching tractography (FMT) is based on wave front propagation [Park 02a, Park 02b]. The wave starts at a seed point and a time is assigned to each voxel in the brain space. At a certain step, the neighboring voxels of a point in the wave front are considered. The six voxels with a unit distance are examined excluding the voxels that have already been part of the wave. The time of wave arrival (T) to a candidate voxel is calculated from Equation 3.30. The voxel with minimum arrival time is added to the wave. The process continues until the whole space is spanned.

$$T(\mathbf{r}) = T(\mathbf{r}') + \frac{|\mathbf{r} - \mathbf{r}'|}{F(\mathbf{r})} \tag{3.30}$$

where $\mathbf{r} = [r_x, r_y, r_z]$ and $\mathbf{r}'$ are the position vectors of the neighboring point and the closest point to it in the wave, respectively. $F(\mathbf{r})$ is the speed of wave propagation from $\mathbf{r}'$ to $\mathbf{r}$. For each candidate voxel, the perpendicular direction $\hat{\mathbf{n}}(\mathbf{r})$ to the wave front is defined using Equation 3.31.

$$\hat{\mathbf{n}}(\mathbf{r}) = \frac{\nabla \mathbf{f}(\mathbf{r})}{\|\nabla \mathbf{f}(\mathbf{r})\|} \tag{3.31}$$

where $\nabla \mathbf{f}(\mathbf{r})$ is computed from the 3×3×3 neighborhood around the candidate point as given by the following equations

$$\nabla \mathbf{f}(\mathbf{r}) = \sum_{i=-1}^{1} \sum_{j=-1}^{1} \sum_{k=-1}^{1} \mathbf{C_{i,j,k}}(r_x - i, r_y - j, r_z - k) \tag{3.32}$$

$$\mathbf{C_{i,j,k}}(r_x - i, r_y - j, r_z - k) = \begin{cases} i, j, k & \text{if } (r_x - i, r_y - j, r_z - k) \in S(p) \\ 0 & \text{if } (r_x - i, r_y - j, r_z - k) \notin S(p) \end{cases} \tag{3.33}$$

where $S(p)$ is the set of voxels that are already added to the wave.

The speed function $F(\mathbf{r})$ can be modeled in different ways. Parker et al. [Park 02b] suggested the formulation in Equation 3.34. The speed at the neighboring point is the minimum of the speed function at the closest wave point ($\mathbf{r}'$) and the cosine of the angle between $\hat{\mathbf{n}}(\mathbf{r})$ and the PDD at $\mathbf{r}'$. Thus, the speed is maximized if the PDD is in the direction of the normal to the wave front.

$$F(\mathbf{r}) = min(F(\mathbf{r}'), |\mathbf{e_1}(\mathbf{r}') \cdot \hat{\mathbf{n}}(\mathbf{r})|) \tag{3.34}$$

The fiber trajectories are found by seeking the pathways with maximum speed. Each point in the image space is considered as a potential termination point of the tract. The speed is determined from the seed point to each candidate end. FMT has the advantages of both streamline and connectivity maps. It shares with the streamlines techniques the ability to provide individual fibers. Furthermore, it allows for fiber intersection and branching. The average speed along the estimated brain connections can be used as a confidence measure.

3.6.3 Segmentation

Segmentation is adopted in DTI by grouping the voxels with common similarities to form a fiber bundle. Many of the commonly used segmentation algorithms have been extended to DTI. Zhukov et al. used level sets on volumes of scalar DTI-derived anisotropy and diffusivity measures to identify fiber bundles [Zhuk 03]. Complete diffusion tensor based distance measures are proposed as similarity criteria for fiber bundle delineation [Wang 05, Arsi 06, Flet 07]. More details of these measures and the segmentation will be discussed in Chapter 4. Snakes and livewire frameworks for segmentation are proposed utilizing the Log-Euclidean distance measure between diffusion tensors [Hama 06]. This group of algorithms targets fiber bundles having high regularity.

3.7 Clinical Application

Diffusion weighted imaging is proven to be effective in the early diagnosis and investigation of cerebral diseases such as acute stroke [Mose 90, Lans 00] and abscesses [Cart 04]. Diffusion tensor derived parameters such as the degree of anisotropy and the diffusivity parameters are used to evaluate certain neural pathologies and were found to be sensitive to white matter abnormalities. Axonal degeneration evaluated by diffusion tensor derived parameters were evident in the temporal lobe for mild cognitive impairment and Alzheimer disease patients [Huan 07, Chen 09]. In relapsing-remitting multiple sclerosis, reduced anisotropy accompanied by increased isotropic apparent diffusion were observed correlating to the signature of Wallerian degeneration [Henr 03]. The process of normal human brain maturation and aging affecting the structure of myelin were monitored using DTI [Sala 05, Hupp 01].

3.8 Conclusion

Diffusion tensor imaging provides a valuable set of information describing the fiber microstructure. The Brownian motion of the water-like molecules is used to modulate the MRI-signal resulting in diffusion weighted images. The nature of the diffusion depends on the structure where it is measured. Tubular structures guide the diffusion leading to a more anisotropic diffusion and greater attenuation. Therefore, the fiber structure can be captured by measurements along different directions. The diffusion profile within a voxel is approximated by a Gaussian distribution with the diffusion tensor corresponding to the covariance matrix. The diagonalization of the tensors gives the main fiber orientation as well as parameters describing the diffusion process and the fiber structure. Therefore, it was utilized for the identification of different fiber structures. The rich data ranges from scalars and vectors to the tensors. Various visualization techniques are proposed. This includes grayscale intensity images corresponding to the DTI-derived measures, RGB-images illustrating the diffusion direction or the geometries of the diffusion tensors, complex techniques such as ellipsoids or glyphs. DTI-derived parameters are used to detect the fiber abnormalities in the presence of pathologies. Despite the great capabilities offered by DTI, the diffusion tensor faces problems at voxels with multi-fiber orientations. Moreover, voxels could be comprised of more than one tissue (e.g., white matter and gray matter) and the averaging process will not lead to the adequate description of the diffusion for this class of voxels. Thus, additional models of the diffusion process are suggested that overcome the tensor problems. However, these models are complex and require increased scanning times and, thus, are not clinically practical. DTI is utilized in this thesis to identify the visual system.

Chapter 4

Segmentation of the Optic Radiation

The algorithm and the results presented in this chapter have been published in
A. El-Rafei, J. Hornegger, T. Engelhorn, A. Dörfler, S. Wärntges, and G. Michelson. "Automatic segmentation of the optic radiation using DTI in glaucoma patients". In: Computational Vision and Medical Image Processing - VipIMAGE 2009. International Conference VipIMAGE 2009 - II ECCOMAS Thematic Conference on Computational Vision and Medical Image Processing, Portugal, pp. 293-298, Taylor and Francis, 2009.
A. El-Rafei, T. Engelhorn, S. Waerntges, A. Doerfler, J. Hornegger, and G. Michelson. "Automatic segmentation of the optic radiation using DTI in healthy subjects and patients with glaucoma". In: Tavares JMRS, Jorge RMN, editors. Computational Vision and Medical Image Processing, Computational Methods in Applied Sciences, pp. 1-15, Springer, 2011.

4.1 Introduction

The analysis of the glaucoma effect on the visual pathway requires the identification of the bundles comprising the pathway. The optic radiation is selected as the traget of the studies performed in this thesis. The reason is that the optic radiation is the largest object in the pathway. The other fibers have relatively small sizes and irregular regions such as the intersection at the optic chiasm. Therefore, the reliability of the identification is limited and is subject to many factors. In this work, we focus on the homogenous fiber bundle of the optic radiation, that is described by tensors sharing common orientation and a degree of similarity. We aim to provide a system for the automatic identification of the optic radiation in normal subjects and glaucoma patients. DTI is used to segment the optic radiation, as it is the only imaging modality that allows the identification of white matter fiber structure non-invasively.

Many algorithms were proposed for the identification of white matter tracts using DTI as discussed in Chapter 3. The dominant category is streamline tractography which is based on following the fiber tracts using the main diffusion direction. As the fiber pathway is integrated during the tracking process, tractography errors are accumulated. Connectivity maps were suggested to explore the probability of a selected seed point being connected to its surrounding neighborhood which can be the whole brain. The main disadvantage of connectivity maps is that they do not pro-

vide a straightforward plausible visualization of the results. The split and merge technique [Bozk 07] attempts to avoid the accumulated errors of tractography by identifying short tracts. This is done by limiting the tracking process to a certain number of steps. Then, it provides a degree of membership of the extracted tracts belonging to the same fiber. The practicality of the split and merge technique is limited because it does not describe the complete fiber pathway. Segmentation approaches of DTI [Zhuk 03, Wang 05, Hama 06] are more suitable for identifying coherent densely packed bundles of axons. The segmentation avoids the drawbacks from both connectivity maps and tractography such as tracking accumulation errors and the need to merge the individual tracts to obtain fiber bundles. Furthermore, it relies on the coherence within the fiber bundle of interest. Therefore, the segmentation approach is adopted in this work.

Some neuronal diseases such as glaucoma compromise the status of the visual pathway. The understanding of the pathological mechanisms is essential in order to provide the appropriate treatment. Therefore, fiber tracking methods aim to parcellate the architecture of the cerebral part of the visual system. Staempfli et al. modified the FMT described in Section 3.6.2 [Stae 06]. Depending on the anisotropy at the candidate and front voxels, different speed functions were used. This technique is referred to as advanced fast marching tractography (aFMT). It was shown that the performance is superior to FMT at locations with IOVH. The aFMT was used to reconstruct the visual system [Stae 07]. Seed regions were manually placed on the right and left optic nerve as well as on the optic chiasm. A three-stage probabilistic approach (ConTrack) was suggested to estimate the most likely connections between two cerebral regions [Sher 08b]. The user identified two anatomical regions of interests (ROIs) where he wanted to locate the connecting fibers. The algorithm started by generating large number of samples linking the two ROIs. The system weighted each sample fiber in a process called scoring. Finally, the score determined the most probable tracts. However, an additional user intervention was required to visually validate the selection. ConTrack was applied to find the fibers of the optic radiation. The two ROIs were identified on the LGN and the primary visual cortex [Sher 08a]. The optimal DTI configuration leading to accurate optic radiation tracking was investigated [Stie 11]. Tractography initiated at different seed regions were examined in this study including the optic chiasm and the occipital lobe. The results were found to be dependent on the initialization.

Most of the proposed white matter identification algorithms did not address the problem of algorithm initialization including the aforementioned methods. They rely on the interaction of medical experts to select the seed points or the region of interest of the desired fiber tracts in tractography algorithms. In addition, the initialization of the segmentation engines to include the desired fiber bundle is performed by a human operator. This is a rather time consuming process and might limit the number of subjects in clinical studies that involves DTI. Furthermore, inconsistencies between operators could arise leading to different results. The proposed segmentation system utilizes the physiological properties of the optic radiation to produce a robust initialization of the proposed segmentation system in both healthy and pathological subjects with glaucoma.

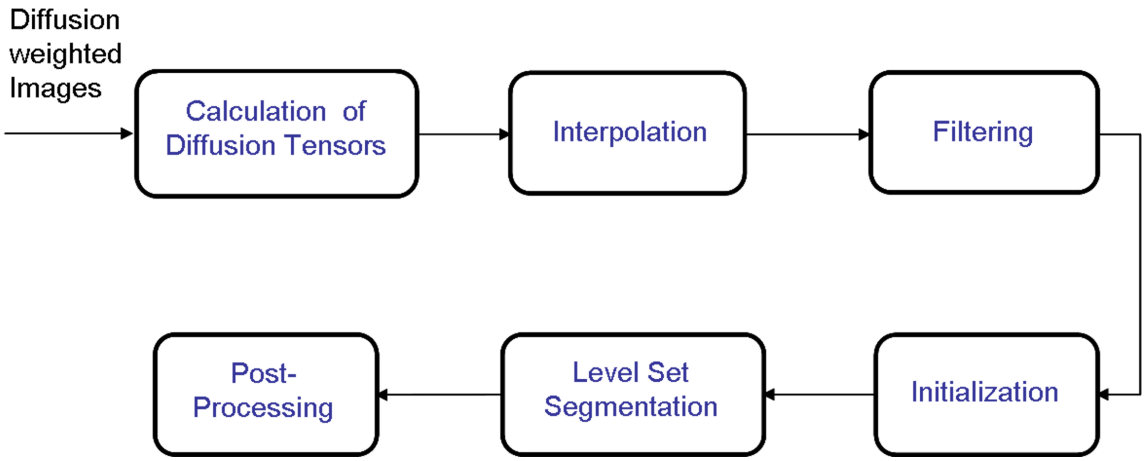

Figure 4.1: Schematic of the segmentation algorithm. The system identifies the optic radiation in a segmentation based approach from diffusion tensor data. The diagram demonstrates the processing steps that comprise the system.

The proposed segmentation system utilizes the complete tensor information in a statistical level set frame work that takes into account the Riemannian nature of the tensor space. The algorithm is validated on DTI-images of the subjects indicated in Section 4.2. It consists of the following steps shown in Figure 4.1: First the diffusion tensor and related anisotropy measures are calculated from the diffusion weighted images. The calculated diffusion tensor data is transformed into the Log-Euclidean framework and interpolated as presented in Section 4.3.1. In Section 4.3.2, DTI-data is regularized to increase the coherence of the optic radiation fiber bundle before obtaining an initial estimate of the optic radiation using thresholding and connectivity analysis. The midbrain is initially identified using a similar analysis to that of the optic radiation. The system extends the statistical level set framework for DTI segmentation developed by Lenglet et al. [Leng 06] to be used in conjunction with the Log-Euclidean dissimilarity distance as detailed in Section 4.3.3. The optic radiation is obtained by iteratively evolving the level set function. Finally, the output from the level set framework is adjusted in a post-processing step based on the relative location of the optic radiation and the midbrain. Sections 4.4 and 4.5 contain the results and discussion, respectively.

4.2 Materials

Eighteen subjects were examined by ophthalmologists and categorized into two age matched groups. The first group represented the subjects that were diagnosed with primary open angle glaucoma and the other group represented the normal subjects. The glaucoma group contained 9 subjects with a mean±standard deviation age of 66±11.8 years with 7 females and 2 males, while the normal group contained 9 subjects with a mean±standard deviation age of 67.1±8.1 years with 6 females and 3 males. Further ophthalmological and neuroradiological examinations were performed

and did not provide indications of microangiopathy or irregularly developed optic radiation.

The subjects were scanned using a 3T-MRI scanner. The diffusion weighted images were acquired using a single-shot, spin echo, EPI as an imaging sequence with repetition time (TR) 3400 ms, echo time (TE) 93 ms, field of view (FoV) 230 x 230 mm^2, acquisition matrix size of 128 x 128 reconstructed to 256 x 256, seven signal averages, and partial Fourier acquisition of 60%. The axial slices had a thickness of 5 mm and 1 mm intraslice resolution. Diffusion weighting were applied with a maximal b-factor of 1000 s/mm^2 along 15 icosahedral directions complemented by one scan with b = 0. The diffusion tensors were calculated from the measured diffusion weighted images along with fractional anisotropy, eigenvectors and eigenvalues on a voxel by voxel basis.

4.3 Methods

The steps of the system are detailed in this section. The input to the system is the acquired diffusion weighted images. The diffusion tensors are calculated using singular value decomposition. The diffusion tensor is analyzed using the eigenvalue-decomposition to determine the PDD. The degree of anisotropy is measured by FA. Figure 4.1 demonstrates the algorithm application flow to the DWI-images. The results are segmented optic radiations on DTI-volumes.

4.3.1 Interpolation in the Space of Diffusion Tensors

The diffusion tensors are 3 x 3 symmetric positive definite matrices. The space of diffusion tensors is a convex subset of the vector space $\mathbb{R}^{(3)^2}$ and does not form a vector space using a Euclidean metric [Flet 07, Penn 06]. Thus, the decomposition of the diffusion tensors may result in non-physical negative eigenvalues. Moreover, the Euclidean framework is not appropriate for dealing with tensors. The swelling effect is an example where the average of diffusion tensors with the same determinant could result in a mean tensor with a larger determinant [Coro 06]. Thus, the Riemannian nature of the tensor space should be taken into account when handling the diffusion tensors.

Dissimilarity metrics have been proposed to overcome the limitations of the Euclidean framework. An information theoretic measure called the J-divergence is proposed [Wang 05] based on the symmetric Kullback-Leibler divergence between two Gaussian probability densities. The J-divergence distance between two diffusion tensors are given by Equation 4.1 and is affine-invariant. i.e., the distance between tensors are independent from affine transformation of the coordinate system.

$$d_J\left(D_1, D_2\right) = \frac{1}{2}\sqrt{tr\left(D_1^{-1}D_2 + D_2^{-1}D_1\right) - 2n} \tag{4.1}$$

where n is the size of the diffusion tensors D_1 and D_2.

Fletcher and Joshi [Flet 07] delt with the space of diffusion tensors as a curved manifold called Riemannian symmetric space. They derived a Riemannian metric on the space of diffusion tensors. The proposed metric accounts for the positive

definiteness constraint. This ensured that the eigenvalues of the diffusion tensors were positive.

The Log-Euclidean framework proposed by Arsigny et al. [Arsi 06] provides a Riemannian framework to deal with the diffusion tensors. Using this framework, the diffusion tensor space of positive semi definite matrices can be transformed into the space of symmetric matrices, i.e., a vector space. Additionally, all operations performed on vectors can be used on the vector form of the diffusion tensor in the Log-Euclidean framework. Despite the similar properties of the Log-Euclidean metric compared to other dissimilarity distances such as the J-divergence distance or the Riemannian metric by Fletcher and Joshi, the Log-Euclidean framework has a significantly lower computational cost as it involves vector operations.

The Log-Euclidean distance d_{LE} between tensors D_1 and D_2 is defined by

$$d_{LE}\left(D_1, D_2\right) = \| \log\left(D_1\right) - \log\left(D_2\right) \| \tag{4.2}$$

where log is the matrix logarithm given by

$$D = \left[\begin{array}{c} \mathbf{e_1}\ \mathbf{e_2}\ \mathbf{e_3} \end{array} \right] \cdot \begin{pmatrix} log(\lambda_1) & 0 & 0 \\ 0 & log(\lambda_2) & 0 \\ 0 & 0 & log(\lambda_3) \end{pmatrix} \cdot \left[\begin{array}{c} \mathbf{e_1}\ \mathbf{e_2}\ \mathbf{e_3} \end{array} \right]^T \tag{4.3}$$

In this thesis, we have used the similarity invariant metric in Equation 4.4.

$$d_{LE}\left(D_1, D_2\right) = \left(tr\left(\left[\log\left(D_1\right) - \log\left(D_2\right)\right]^2\right)\right)^{\frac{1}{2}} \tag{4.4}$$

The interpolation of the DTI-data is necessary in order to obtain a volumetric identification of the optic radiation. The interpolation of the tensors using the Euclidean calculus results in the non-physical swelling effect. This effect is also evident in interpolating two tensors, where it is possible to get an interpolated tensor that has a larger determinant than the original tensors. Interpolation in the Log-Euclidean framework avoids the swelling effect at a computationally attractive cost. The diffusion tensor D is interpolated trilinearly at non-grid position $\mathbf{r}$ as the Log-Euclidean weighted sum of N tensors in a neighborhood of the non-grid position $\mathbf{r}$. The weights (w) are inversely proportional to the spatial distances between the non-grid position and the locations of the tensors in the neighborhood. The used interpolation formula is

$$D\left(\mathbf{r}\right) = \exp\left(\frac{\sum_{i=1}^{N} w_i\left(\mathbf{r}\right) \log\left(D\left(\mathbf{r}_i\right)\right)}{\sum_{i=1}^{N} w_i\left(\mathbf{r}\right)} \right) \tag{4.5}$$

where exp and log are the matrix exponential and logarithm, respectively. i is the index of the neighboring voxels.

4.3.2 Initial Estimation of the Optic Radiation and the Midbrain

In this step, the optic radiation and the midbrain are initially identified. The diffusion tensor data is regularized by applying Perona-Malik diffusion filtering [Pero 90].

Perona and Malik proposed an anisotropic filtering technique based on controlling the heat flow according to the presence of edges. The edges are estimated by the magnitude of the image gradient. The heat-diffusivity is non-linearly inversely proportional to the magnitude of the image gradient, i.e., the flow is limited at large image gradients indicating the presence of an edge with high probability. Conversely, it is increased at small image gradients. The evolution of the image $f(x, y, z) : \Omega \subset \mathbb{R}_3 \rightarrow \mathbb{R}$ is governed by the following diffusion equation

$$\frac{\partial f}{\partial t} = div(\rho(\|\nabla f\|)\nabla f) \tag{4.6}$$

where $\rho = e^{-\frac{\|\nabla f\|^2}{k}}$ or $\rho = \frac{1}{1+\|\nabla f\|^2/k}$.

The anisotropic filtering is applied componentwise to the transformed Log-Euclidean vector form of the diffusion tensors. Regularization is performed to reduce the noise and to increase the coherence inside the fiber bundles while preserving the boundaries of the fiber bundles.

The initial estimation of the optic radiation is based on the fact that the main fiber bundle of the optic radiation is dominated by a diffusion in the anterior-posterior direction. Moreover, the optic radiation is a massive fiber bundle which occupies a significant part of the brain white matter. This physiological information regarding the diffusion direction and the size of the optic radiation gives a unique discrimination of the optic radiation from other fiber bundles.

The image is analyzed on a voxel by voxel basis to create a binary mask representing the initial optic radiation. The vector corresponding to the main diffusion direction (PDD) has three components: the anterior-posterior component (AP), the left-right component (LR), and the superior-inferior (SI) component. The three components at each voxel are compared and the foreground voxels of the binary mask are selected to have a dominant AP component. The foreground voxels satisfy the inequalities given by Equation 4.7. i.e., the AP-component is greater than a user specified factor (AP_{thres}) of the sum of the other two components and an FA value greater than 0.2. The fractional anisotropy threshold is used to ensure the coherence of the fiber bundle and that the partial volume effects [Alex 01] are avoided. In DTI, partial volume effects are the result of the limitation of the tensor model in describing complex fiber situations such as fiber crossing or branching situations within a voxel. This results in a reduced FA and a misleading tract orientation. The remaining voxels that do not satisfy the selection criteria are set as the background of the binary image.

$$AP > AP_{thres} \times (LR + SI) \qquad and \qquad FA > 0.2 \tag{4.7}$$

A three dimensional 6-neighborhood connectivity analysis is performed on the binarized image. Connected objects are determined and the left and right parts of the optic radiation are initially identified as the largest objects dominated by diffusion in the anterior-posterior direction. This estimation will be used in the segmentation step as an initialization of the level set. The estimation of the optic radiation is demonstrated in Figure 4.2.

The analysis applied to estimate the optic radiation is similarly applied to identify the midbrain. The analysis takes into account that the midbrain is characterized by

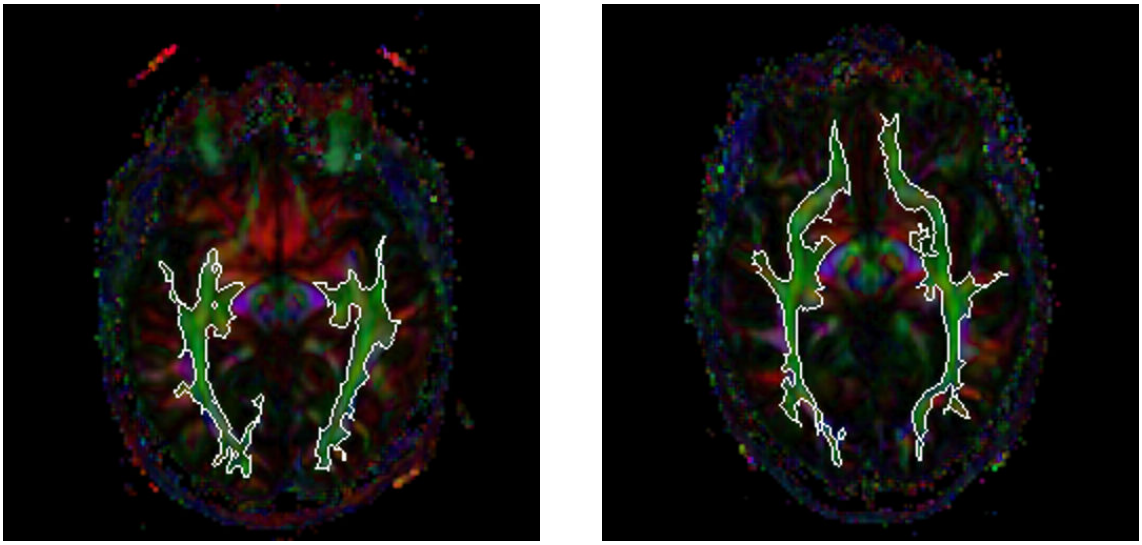

Figure 4.2: The initial estimation of the optic radiation using thresholding and connectivity analysis in two axial brain images

diffusion in the superior-inferior direction and is located in the neighborhood of the centers of the axial brain slices. The relative position of the estimated midbrain to the optic radiation will be used in a later step to refine the segmentation of the optic radiation. The segmented midbrain is shown in Figure 4.3.

4.3.3 Segmentation Using a Statistical Level Set Framework

The segmentation is performed in two steps. First, the DTI-image is segmented using a statistical level set framework. The initially estimated optic radiation as described in Section 4.3.2 is used as the initial surface. Second, the results from the level set framework are adjusted based on anatomical information regarding the white matter organization of the midbrain and the optic radiation.

We extend the surface evolution framework developed by Lenglet et al. [Leng 06] to work with the Log-Euclidean dissimilarity measure given in Equation 4.4. The diffusion tensor D at voxel $\mathbf{r}$ is mapped to the space of 3×3 symmetric matrices by taking its logarithm. Then, it is transformed into a 6-dimensional vector form ($\mathbf{B}(\mathbf{r})$) using the mapping (vec) in Equation 4.8. In this subsection, we present briefly the mathematical formulation of the level set framework in the case of the Log-Euclidean framework. For further details see [Leng 06, Arsi 06]. Using the notation in Equation 4.8, the mean $\boldsymbol{\mu_{LE}}$, covariance matrix Cov_{LE} and Gaussian distribution between diffusion tensors $P_{LE}\left(\mathbf{B}(\mathbf{r_i})\right)$ can be defined as

$$\mathbf{B}(\mathbf{r}) = vec\left(\log\left(D(\mathbf{r})\right)\right) \tag{4.8}$$

$$\boldsymbol{\mu_{LE}} = \frac{1}{N}\sum_{i=1}^{N}\mathbf{B}(\mathbf{r_i}) \tag{4.9}$$

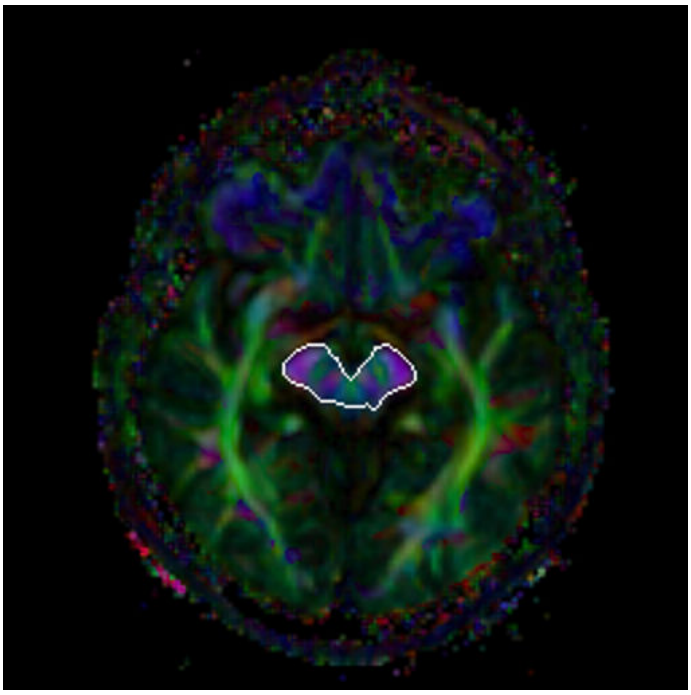

Figure 4.3: Midbrain initial segmentation on a direction color coded image

$$Cov_{LE} = \frac{1}{N-1}\sum_{i=1}^{N}\left(\mathbf{B}(\mathbf{r_i}) - \boldsymbol{\mu_{LE}}\right)\left(\mathbf{B}(\mathbf{r_i}) - \boldsymbol{\mu_{LE}}\right)^T \tag{4.10}$$

$$\begin{aligned} P_{LE}\left(\mathbf{B}(\mathbf{r_i})\right) = & \frac{1}{\sqrt{(2\pi)^6 |Cov_{LE}|}} \\ & \times \exp\left(-\frac{\left(\mathbf{B}(\mathbf{r_i}) - \boldsymbol{\mu_{LE}}\right)^T Cov_{LE}^{-1}\left(\mathbf{B}(\mathbf{r_i}) - \boldsymbol{\mu_{LE}}\right)}{2}\right) \end{aligned} \tag{4.11}$$

The spatial gradient of the diffusion tensor in the vector space is given by

$$\begin{aligned} |\nabla \mathbf{B}(\mathbf{r})|^2 = \frac{1}{2}\sum_{k=1}^{3}\sum_{s=\pm 1} tr\Big(& \left(\mathbf{B}(\mathbf{r}) - \mathbf{B}(\mathbf{r} + s \times \mathbf{i_k})\right) \\ & \times \left(\mathbf{B}(\mathbf{r}) - \mathbf{B}(\mathbf{r} + s \times \mathbf{i_k})\right)^T \Big) \end{aligned} \tag{4.12}$$

where i_k, k=1, 2 ,3 denotes the canonical basis of $\mathbb{R}_3$. $s \in \{1, -1\}$ and denotes the forward and backward approximations of the gradient.

The idea of the statistical surface evolution is to seek the optimal partitioning of the tensor image ($\mathbf{B}$ in the Log-Euclidean case) by maximizing a posteriori frame partition probability for the diffusion tensor image with image domain Γ. This is done in a level set framework, where the image is partitioned into three regions based on a level set function ϕ: inside Γ_{in}, outside Γ_{out}, or on the boundary Γ_b. The boundary is defined by the zero-crossings of ϕ. The probability distributions of the tensors inside (p_{in}) and outside (p_{out}) regions are modeled by Gaussian distributions of the tensors in their respective regions using Equation 4.11. The partition probability is given by

$$P(\mathbf{B}|\phi) = \prod_{\mathbf{r}\in\Gamma_{in}} p_{in}(\mathbf{B}(\mathbf{r})) \prod_{\mathbf{r}\in\Gamma_{out}} p_{out}(\mathbf{B}(\mathbf{r})) \prod_{\mathbf{r}\in\Gamma_b} p_b(\mathbf{B}(\mathbf{r})) \tag{4.13}$$

The boundary probability distribution p_b is selected to have a value of approximately one for high gradients of the diffusion tensors (using Equation 4.12 for gradient calculations) and a value of approximately zero for low gradients as the following relation indicates.

$$p_b\left(\mathbf{B}(\mathbf{r})\right) \propto \exp\left(-g\left(|\nabla\mathbf{B}(\mathbf{r})|\right)\right) \tag{4.14}$$

where $g(u) = 1/(1+u^2)$.

This leads to the energy minimization formulation:

$$\begin{aligned} &E(\phi, \boldsymbol{\mu_{LE_{in/out}}}, Cov_{LE_{in/out}}) \\ &= \nu \int_\Gamma \delta(\phi)|\nabla\phi|dx + \int_\Gamma \delta(\phi)|\nabla\phi| g(|\nabla\mathbf{B}(\mathbf{r})|)dx \\ &- \int_{\Gamma_{in}} \log(p_{in}(\mathbf{r}))dx - \int_{\Gamma_{out}} \log(p_{out}(\mathbf{r}))dx \end{aligned} \tag{4.15}$$

where δ is the Dirac delta function.

The following Euler-Lagrange equation is used to evolve the level set function

$$\begin{aligned} \frac{\partial\phi}{\partial t} = \delta(\phi)\Bigg(&\left(\nu + g(|\nabla\mathbf{B}(\mathbf{r})|)\right) div\left(\frac{\nabla\phi}{|\nabla\phi|}\right) \\ &+ \frac{\nabla\phi}{|\nabla\phi|}\cdot\nabla g(|\nabla\mathbf{B}(\mathbf{r})|) + \log\left(\frac{p_{in}}{p_{out}}\right)\Bigg) \end{aligned} \tag{4.16}$$

The level set function in Equation 4.16 is evolved iteratively to obtain the desired segmentation and the statistics are updated after each iteration.

The output from the level set framework contains the fiber bundle of the optic radiation and additional bundles connected to it such as traces of the optic tract. The reason for this is that the optic tract is connected to the optic radiation and the diffusion direction is also anterior-posterior in the connection area so traces of the optic tract are segmented as well. The LGN connects the optic radiation to the optic tract and is located laterally to the midbrain. Therefore, the LGN position can be used to separate the optic tract from the optic radiation. Based on this anatomical information, the segmented region is automatically adjusted in order to confine the segmentation results to the part representing the optic radiation. The relative position of the segmented optic radiation to the midbrain is used instead of the relative position to the LGN. The reason for this is that the midbrain is larger, more reliable to identify and in turn more robust. Moreover, the LGN is located adjacently lateral to the midbrain. The midbrain is previously identified in the initialization step. The plane corresponding to the anterior boundary of the segmented midbrain is selected as the separation level between the optic radiation and the optic tract. The segmentation results anterior to the selected plane are eliminated leaving the optic radiation and approximately eliminating the part corresponding to the optic tract.

Table 4.1: The segmentation accuracy of the normal subjects and glaucoma patients

Subjects' Class	Number of Subjects	Segmentation Accuracy	
		Mean	Standard Deviation
Normal Subjects	9	82.71%	6.43%
Glaucoma Patients	9	82.76%	7.55%

4.4 Results

The segmentation system was applied to the DTI-datasets and the optic radiation in the two groups was identified. The left side of Figure 4.4 shows the final segmented optic radiation on non-diffusion weighted axial slices with b = 0 from two sample subjects. The color coded fractional anisotropy representation of the DTI-data is demonstrated on the right side of the figure.

The segmentation results were evaluated by comparing them with a manual segmentation of the optic radiation main fiber bundle performed by a physician experienced in neuroimaging. The accuracy of the segmentation system is calculated as the percentage of the overlap volume between the automatic segmentation results and the manual segmentation to the total volume of the manually segmented optic radiation. The segmentation accuracy is summarized in Table 4.1. The accuracy of the segmentation is 82.71% for the normal subjects and 82.76% for the glaucoma group.

4.5 Discussion

The presented algorithm is able to capture the complicated structure of the optic radiation as evident from the results. Despite the variable course of the optic radiation, the system accuracy is 82.7%. Moreover, the system is fully automated and operates in the Log-Euclidean space. Employing the Euclidean metric for measuring the similarity between diffusion tensors ignores the Riemannian nature of the tensor space and does not represent adequately the dissimilarity between tensors. The Log-Euclidean distance measure avoids the inefficiencies of the Euclidean framework while maintaining almost the same complexity of calculations. This is due to the ability to transform the tensors in the Log-Euclidean space into vectors. Therefore, all computations can be performed using the Euclidean calculus on the mapped vectors.

The analysis of the segmentation errors showed that the errors typically occur in the region where the optic radiation branches in the proximity of the visual cortex. Due to the branching of the optic radiation in this region, the incoherence increases leading to reduced anisotropy and unreliability in determining the fiber orientation direction. Moreover, the anterior-posterior direction in this region is no longer the dominating diffusion direction and the dissimilarity between the tensors in the main fiber bundle and the tensors in this region is relatively high. Another source of errors is the relatively small coherent fiber bundles intersecting the optic radiation and sharing the diffusion direction and tensor similarity near the intersection location. Figure 4.5 shows the mentioned classes of errors on a sample subject as indicated by arrows. If the overlap is measured only on the central axial slice containing the

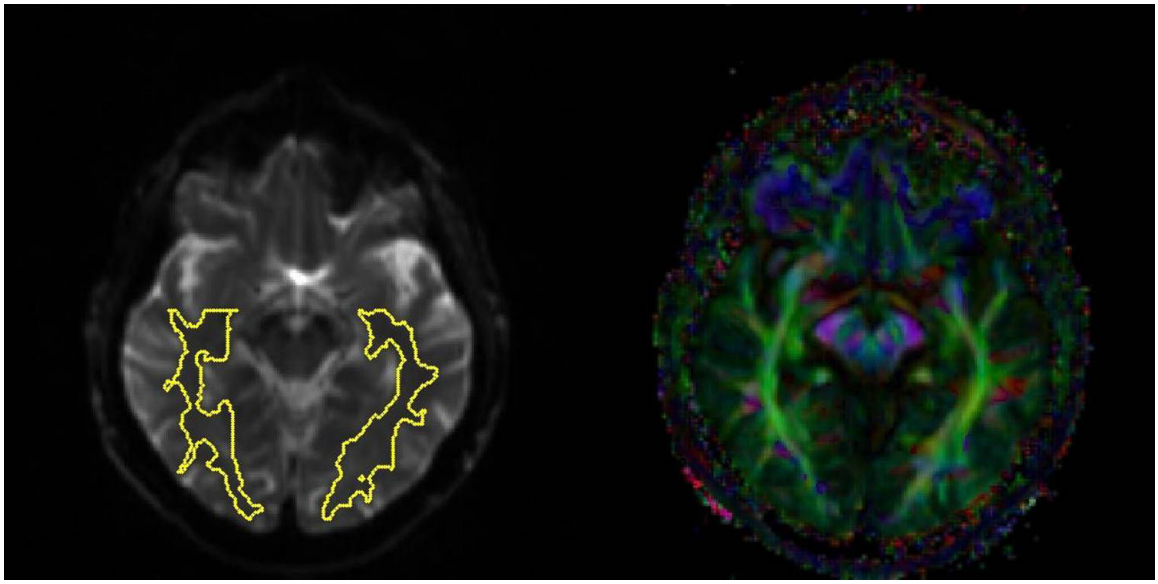

(a)

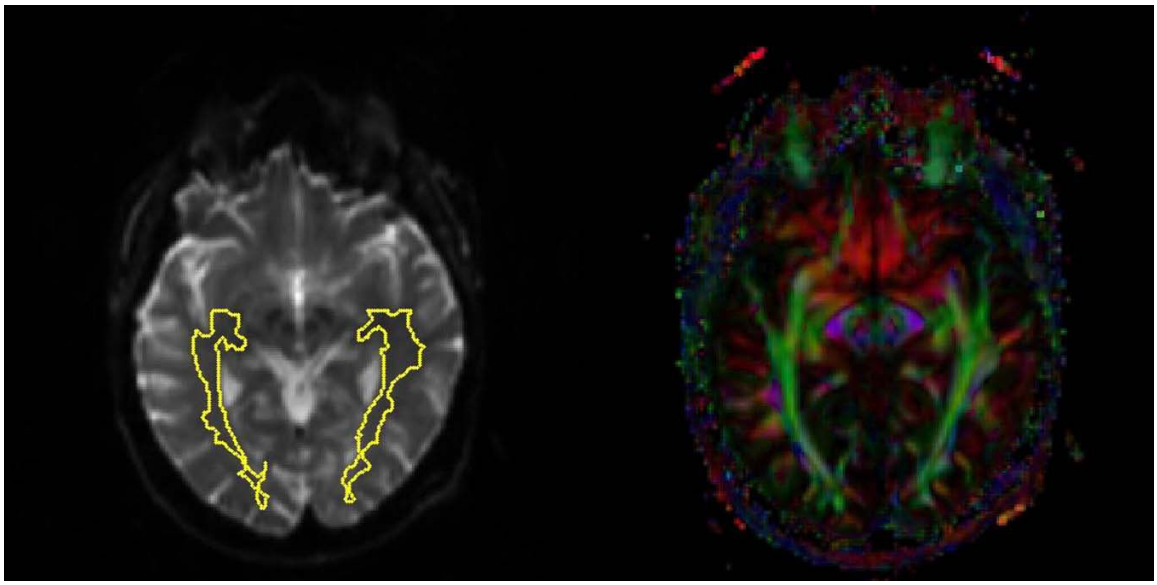

(b)

Figure 4.4: Segmentation of the optic radiation in two sample subjects shown on a non-diffusion weighted image (b=0) on the left side. The color coded fractional anisotropy image is shown on the right side. The main fiber bundle of the optic radiation and the lateral geniculate nucleus (LGN) of the visual pathway are clearly identified.

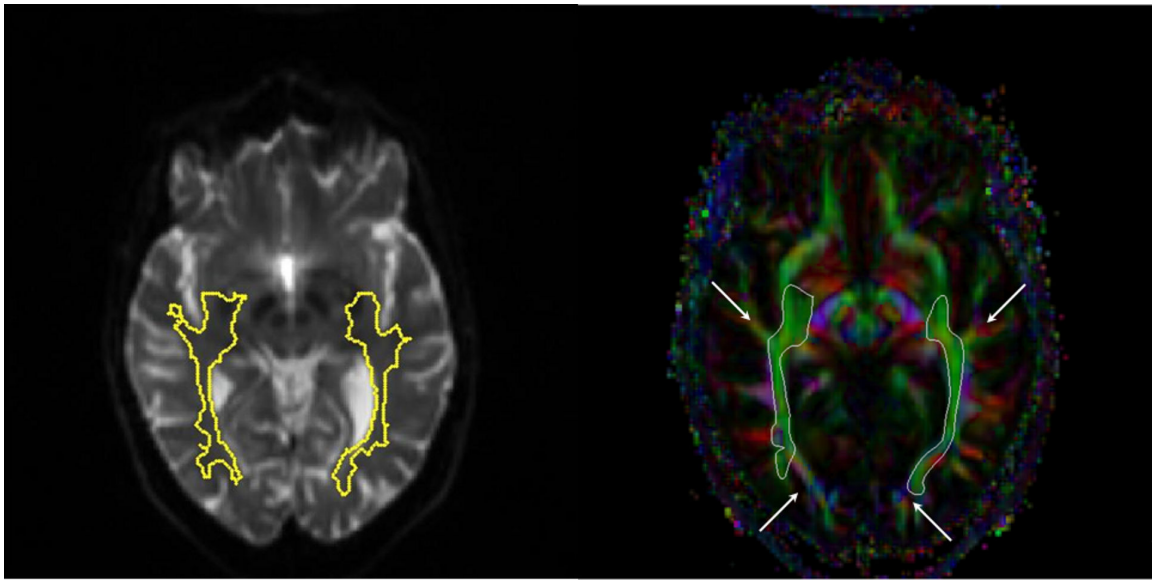

Figure 4.5: The errors of segmentation of the optic radiation demonstrated on a sample subject as indicated by arrows. The left image shows the manual optic radiation segmentation of a medical expert on an axial brain slice.

LGN, the mean accuracy increases to 86.34%. The errors increase in the slices that are away from the center of the optic radiation due to the limited interslice resolution and the increased IOVH.

The effect of glaucoma on the visual system specifically the optic nerve and the optic radiation was investigated in [Gara 09]. The correlation between glaucoma and diffusion tensor derived parameters such as FA and MD was studied. FA was found to be significantly lower in the glaucoma group when compared to the normal subjects. On the other hand, the MD was significantly higher in glaucoma patients than in the normal subjects. This yields that the diffusion tensors within the optic radiation are generally affected by the presence of the neurologic pathology of glaucoma. Despite these findings, the proposed automated segmentation algorithm has approximately the same accuracy for normal subjects and glaucoma patients. This robustness is due to the dependence of the system on the physiological and anatomical properties which are slightly affected by glaucoma.

The selection of the seed region is crucial to a correct fiber tracking. The seed points should be placed with great attention from an expert in the neuroanatomy and DTI. Furthermore, the user should ensure that the tracking results started from the selected region span the entire target fiber. The algorithm could face some problematic situations trying to connect two areas belonging to the same tract with fiber heterogeneity in between. Whole brain tractography is an alternative approach where each voxel in the brain space is considered a seed point. This results in redundancy and significantly increased runtime. Moreover, it does not eliminate the requirement of user intervention. An experienced user should locate a region where most of the individual traced fibers pass through. These fibers are then regarded as the targeted bundle. Fiber clustering methods utilizes the similarity between neighboring fibers to group them into bundles [Ding 03, Mobe 05, ODon 06, Zhan 08]. However, this adds

an additional challenge and potential source of errors, especially when considering bundles with intersecting or diverging tracts such as the visual system. Relatively small number of studies attempt to propose algorithm initialization. The initialization of the presented system leads to a decreased number of system iterations and the necessity for an experienced operator. It overcomes the mentioned problems reducing the inter-operator variations.

The high individual variability of the brain fiber structure and the special nature of DTI-data require great attention when dealing with the segmentation of major fiber bundles. The diffusion tensor contains information about the diffusion direction and the degree of diffusion properties. Most tractography methods rely on the PDD to reconstruct the white matter fibers and do not completely utilize all the data in the tensors. In addition, the segmentation based on anisotropy measures alone or only diffusion directions results in a loss of information and inaccuracy in segmentation. Therefore, the whole tensor is incorporated in the proposed algorithm. In the following chapters, the segmentation system will be used to facilitate the glaucoma analysis in the optic radiation region.

Chapter 5

Voxel Based Morphometry Analysis of the Optic Radiation in Glaucoma

This chapter contains the work and results previously introduced in the article
A. El-Rafei, T. Engelhorn, S. Waerntges, A. Doerfler, J. Hornegger, and G. Michelson. "A framework for voxel-based morphometric analysis of the optic radiation using diffusion tensor imaging in glaucoma". Magnetic Resonance Imaging, Vol. 29, No. 8, pp. 1076-1087, 2011.

5.1 Introduction

The high prevalence and damage irreversibility of glaucoma require greater attention to provide more appropriate therapies. Despite the extensive research on glaucoma and the valuable findings described in Chapter 2, the causes of glaucoma remain uncertain and the pathophysiology mechanism is not yet fully understood. Localizing the glaucoma effect on the visual system could provide more insight into the mechanism and progression of glaucoma. The effect of glaucoma on the optic radiation is studied through diffusion tensor-derived parameters only globally and it has not been localized so far. The complexity of diffusion tensor imaging accompanied by inherited uncertainty and the complicated inter-subject variable structure of the optic radiation make localizing the effect of glaucoma on the optic radiation a difficult task. In this chapter, we propose a framework that is able to capture the local changes of the optic radiation due to neuronal diseases. The framework is applied to the glaucoma disease.

Different approaches exist for tracking the white matter fibers from DTI data, some of these are summarized in Chapter 3.6. Algorithms were customized to reconstruct the human visual pathway [Stae 07] and to identify parts of it such as the optic radiation [Sher 08a, El R 11a]. This enables the analysis of the effects of ophthalmological and systemic neurological diseases on the visual pathway. In this work, the optic radiation is identified on diffusion tensor images. The diffusion process is sensitive to the underlying fiber structure, and consequently the diffusion tensor-derived parameters are expected to change in cases of white matter tracts damage due to neurological disorders. Thus, they are commonly utilized to detect the degradation in the cerebral white matter health when examining patholo-

gies [Pier 96a, Hors 02, Song 03, Hami 08]. Increased radial diffusivity is hypothesized to reflect the demyelination degree and this assumption was validated in clinical studies on mouse brain [Song 03, Song 05]. MD represents the magnitude of the diffusion within a voxel. FA indicates the degree of deviation from isotropic diffusion at each voxel. In clinical applications, FA is widely assumed to represent the organization degree of white matter fibers reflecting white matter integrity. Reduced FA values could be interpreted as compromised fiber coherence (degree of cellular structure alignment within a voxel) and possible defects in myelin [Pier 96a, Hors 02, Hami 08].

Analysis of diseases using DTI follows two major approaches. The analysis is performed between a diseased group and a control group. Histogram analysis represents the first approach and is based on statistically analyzing the different features of the histogram of diffusion tensor-derived parameters on a specified region of interest [Vals 05, Nave 07]. Features of the histogram may include mean, median, location of the peak, etc. This approach gives the global significant differences between the two examined groups but it lacks the ability to localize these differences. Voxel-based morphometric analysis examines the local changes of tensor derived-parameters to produce a map of significant abnormalities in the presence of neurological diseases such as optic neuritis, amyotrophic lateral sclerosis [Cicc 05, Thiv 07]. Studying hemispheric asymmetry due to aging effect or pathologies such as schizophrenia is another application of voxel-based analysis [Arde 07, Taka 10b, Taka 10a].

Voxel-based morphometry (VBM) is commonly used in a whole brain analysis for localizing the abnormalities in the presence of pathologies. Brain images from different subjects involved in the study are transformed to a unified coordinate system by registering them to a template. This allows for inter-subject voxel-wise comparisons because each location in the unified coordinate system should include corresponding voxels from all subjects. Due to the complex structure of the brain and the highly inter-subject brain structure variability, the registration is imperfect and significant voxels could arise from the misalignment of images. Smoothing is incorporated to reduce the inter-subject variability and misalignments by replacing the image intensity value by a weighted average from neighboring voxels. Smoothing increases the partial volume effects. A previous study showed that the morphometry analysis depends on the degree of smoothing [Jone 05]. The tract-based spatial statistics (TBSS) approach is proposed to avoid the mentioned problems of conventional VBM [Smit 06]. This approach is one of the well established and applied techniques in morphometry analysis using DTI. TBSS operates on FA images in a multi-step method. First, the FA brain images from different subjects are aligned using non-rigid registration. Then, the mean of the registered FA images is computed and a skeleton of the white matter tracts is calculated from it. Finally, the different subjects are projected onto this alignment invariant tract. The statistical analysis is performed on the voxels of the skeleton. TBSS does not require smoothing and is completely automated and thus observer independent. However, TBSS processes FA images which are affected by white matter degeneration caused by diseases such as glaucoma. The spatial accuracy of the TBSS analysis is limited by the skeleton and therefore does not provide detailed significant locations. In addition, it compares skeletons of the extremely variable complete brain white matter structures.

The proposed framework for the localization of the glaucomatous damage on the optic radiation is object oriented. It processes the optic radiation rather than the whole brain. Whole brain analysis is subject to many sources of inaccuracies and therefore avoided. The framework uses a semi-automated algorithm for identifying the optic radiation to limit the user intervention and increase the reliability of the results. In addition, relying on diffusion tensors or related parameters in the calculation of the similarity in the registration step is not suitable for dealing with glaucoma. This is because different parameters were shown to be affected by glaucoma and consequently the whole diffusion tensors. Thus, an automated shape-based registration approach is incorporated to overcome this limitation. The analysis is restricted to the main fiber bundle of the optic radiation where there is a high degree of shape similarity. This simplifies and facilitates the registration leading to improved inter-subject alignments.

5.2 Materials

5.2.1 Subjects

The performed case-control study included 23 subjects categorized into control and glaucoma groups. The control group consisted of 10 subjects (3 males and 7 females with a mean age of 62.8±13.6 years) while 13 patients (6 males and 7 females with a mean age of 64.7±11.5 years) diagnosed with primary open angle glaucoma (7 patients) and normal tension glaucoma (6 patients) constituted the glaucoma group. Subjects in both groups were randomly selected from the patients in the clinic of the Department of Ophthalmology at the University Erlangen-Nuremberg. The criteria for POAG diagnosis were having an IOP $>$ 21 mmHg associated with an open anterior chamber angle, optic disk cupping and visual field defects $>$ 2 dB. Criteria for diagnosis of normal tension glaucoma were the same as POAG except for an IOP $<$ 21 mmHg. The subjects in the normal groups did not show any abnormalities of the glaucoma specific examination results. The acquired MRI and DTI datasets were utilized for neurological examinations to detect cerebral diseases or irregularly developed optic radiations.

5.2.2 Magnetic resonance and diffusion tensor imaging

A 3T high-field scanner (Magnetom Tim Trio, Siemens, Erlangen, Germany) was used to obtain anatomical T1-weighted images using 3D-MPRAGE (3D-Magnetization Prepared Rapid Gradient Echo) imaging sequence. The strength of the applied gradient field was up to 45 mT/m (72 mT/m effective). The imaging sequence parameters were TR = 900 ms, TE = 3 ms, and FoV = 23 × 23 cm^2. The acquisition matrix size = 512 × 256 reconstructed to 512 × 512 with interslice resolution of 1.2 mm.

Diffusion weighted images were acquired along 20 directions using a maximal b-factor of 1,000 s/mm^2. Additional non-diffusion weighted scan was performed with b = 0. The scanning image sequence protocol was a single-shot, spin echo, EPI with TR = 3,400 ms, TE = 93 ms, FoV = 23 × 23 cm^2, and partial Fourier acquisition = 60%. The acquisition matrix size was 128 × 128 reconstructed to 256 × 256 and

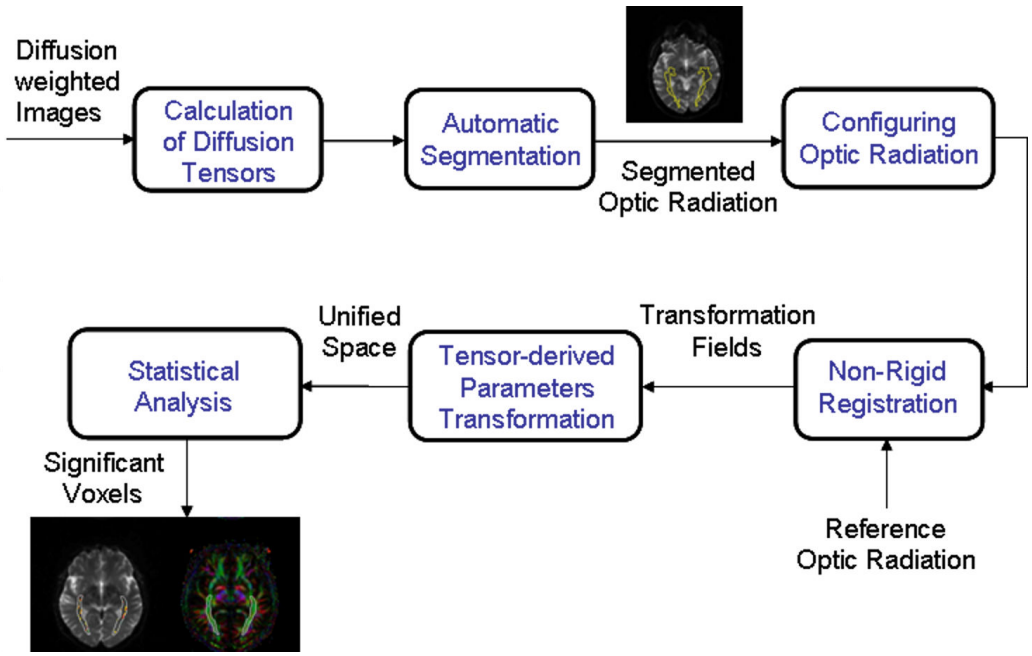

Figure 5.1: Schematic of the analysis framework. The system analyzes the diffusion tensor images of the optic radiation to produce localization maps showing regions with significant differences between glaucoma and control groups. The schematic illustrates the different steps including optic radiation identification and configuration, registration, and statistical analysis.

the number of signal averages was 4. The axial intra-slice spatial resolution was 1.8 $\times$ 1.8 mm^2 with a slice thickness of 5 mm.

5.3 Methods

The schematic of the proposed framework is illustrated in Figure 5.1. The main idea of the system is to spatially normalize the optic radiations from different subjects to a unified space. The identification of the optic radiation is performed automatically. The analysis is confined to the main bundles of the optic radiation. Thus, the inter-subject variability is reduced to be able to accurately compare the fiber bundles from different subjects. This is done manually by removing the highly variable fiber structures and correcting the segmentation errors. The segmented optic radiations from all subjects are non-rigidly registered to a reference template. After the registration, all the segmented regions occupy the same space enabling location-based analysis. The diffusion tensor-derived parameters' images are transferred to the common space using the transformation fields obtained from the registration step. Finally, a statistical analysis is performed to detect the regions which show significant differences between glaucomatous and normal optic radiation groups. The software used in this work was mainly developed by the author under the Matlab environment (Mathworks, Inc., Natick, MA, USA). In the following subsections, the various steps are described in detail.

5.3.1 Automated identification of the optic radiation

The diffusion tensors were calculated from the diffusion weighted images. The brain images were interpolated by upsampling the diffusion tensors at non-grid locations. The individual components of the diffusion tensors were trilinearly interpolated in the Log-Euclidean space [Arsi 06]. The spectral components of the interpolated diffusion tensors were obtained using eigenvalue decomposition. The decomposition results included the eigenvalues of the interpolated diffusion tensors which were used to calculate the diffusivity parameters (AD, RD, and MD) and the anisotropy index (FA).

The previously developed algorithm for automated segmentation of the optic radiation based on DTI data and introduced in Chapter 4 [El R 11a] was used to identify the optic radiation. The algorithm is automated and thus eliminates the necessity for user intervention avoiding inter-user variability. Moreover, the ability of the algorithm to identify the optic radiation in both normal and glaucoma subjects with high efficiency was demonstrated. Therefore, it is suitable to be incorporated into the proposed framework and specifically for the glaucoma analysis.

5.3.2 Configuring the optic radiation

In the axial slice that includes the largest part of the LGN and clearly identifies the intersection between the optic tracts and the optic radiation, there is a high degree of shape similarity of the optic radiation among normal and glaucoma subjects. Therefore, it was selected for further analysis. The manual configuration targeted the minimization of the inter-personal variability by restricting the analysis to the main fiber bundle of the optic radiation in order to benefit from the shape similarity between subjects. The results of the segmentation were compared to a white matter Atlas reconstructed using DTI [Waka 04]. The comparison showed that most of the errors were over-segmentation errors. The occipital part of corpus callosum medially proceeding the optic radiation and traces of the optic tracts were included in the segmentation. Based on the comparison, the segmentation errors were manually corrected by two DTI experts.

The LGN is a small object relative to the limited spatial resolution of the DTI data. Thus, its appearance differs among different subjects which results in shape inconsistency and could lead to inaccuracies in the registration. Therefore, the lateral geniculate nuclei were excluded from the analysis and manually removed from the segmentation. The lateral geniculate nuclei can be easily identified by tracing the optic radiation and locate its intersection with the optic tracts near the anterior end of the optic radiation. The branching part of the optic radiation to the primary visual cortex was eliminated from the analysis due to significant inter-subject variability and measurement uncertainties in this region.

The complex structure of the white matter fibers complicates the configuration process. Moreover, measurement uncertainties arise from partial volume effects as well as limitation of the diffusion tensor model in describing complex fiber situations such as branching or crossing of fibers. The linear, planar, and spherical anisotropy indices [West 04] can be used to detect local fiber homogeneity and heterogeneity (Section 3.5.2). To reduce the inter-operator variability and to systematize the con-

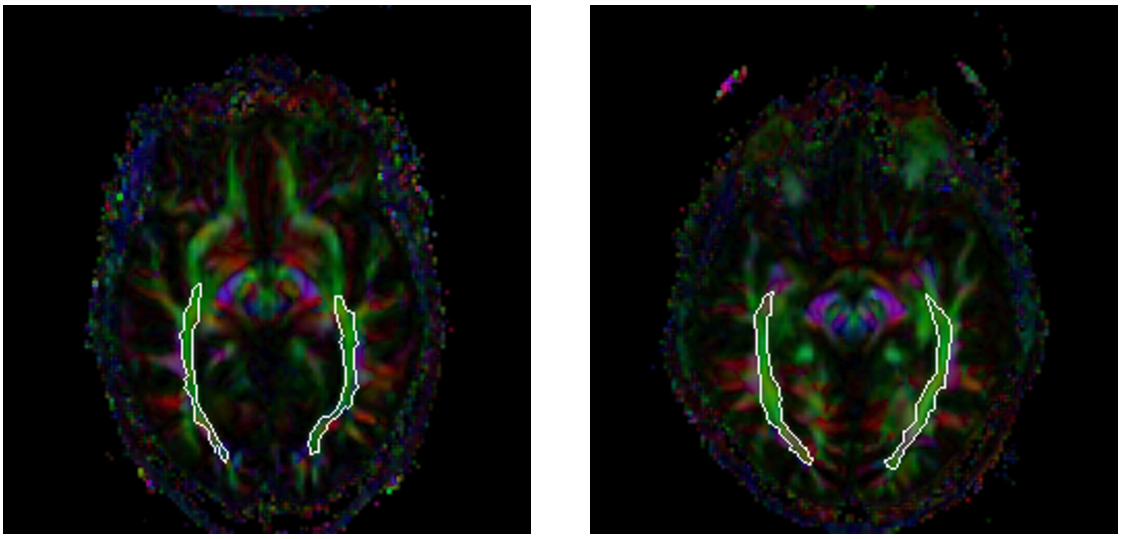

Figure 5.2: The optic radiation on an axial brain slice of two sample subjects after the manual segmentation. The lateral geniculate nucleus (LGN) and the branching to the visual cortex were removed.

figuration process, a graphical user interface (GUI) was developed to facilitate the user interactions. The GUI enables accurate manipulation of the segmentation results on a variety of DTI-derived measures including FA, MD, C_L, and C_P images as well as PDD-color coded images. Thresholding of the mentioned parameters can be performed to visualize only the voxels above or below a certain parameter value. This can be used in conjunction with the linear and planar anisotropy indices to localize branching and intersecting fibers of the optic radiation and facilitate the manipulation procedure. For example, the branching parts of the optic radiation can be identified in a systematic way by increasing C_L threshold gradually until the branching fibers are disconnected from the main fiber bundle of the optic radiation. Then these parts can be manually eliminated. Segmented optic radiation can be visualized on the anatomical diffusion weighted images for further comparison with the known anatomy.

5.3.3 Registration

The optic radiations from different subjects were transformed to a unified space of a reference template. This allowed for voxel-wise comparison and in turn significant region analysis. The sizes of the segmented optic radiations from different subjects were calculated and the normal subject with the maximum optic radiation area in the LGN-slice was selected as the reference subject. A non-rigid registration [Ruec 99] was incorporated to transform the optic radiations from all the subjects into the reference optic radiation space. The used non-rigid registration algorithm did not require any landmarks and was fully automated. The transformation consisted of two parts representing an affine transform and a free-form deformation (FFD). The affine transform modeled the global mapping between the subject to be registered and the reference while the free-form deformation modeled the finer local mapping. In the

affine transform, 12 degrees of freedom were utilized to account for the translation, rotation, scaling and shearing. Prior to the FFD calculation, the optimal affine transformation was estimated by minimizing the sum of squared differences (SSD) between the binary masks of the optic radiations from the subject to be registered and the reference subject. In the free-form deformation part, B-splines were used to describe the image domain. The B-splines were calculated on a mesh of control points covering the image domain. The deformation of the mesh points deformed the corresponding B-splines and consequently the shape of the optic radiation. The FFD transformation was obtained by optimizing the locations of the mesh control points in order to maximize a cost function that corresponded to the image similarity based on the SSD between images. The cost function also included a smoothing term to ensure the smoothness of the free-form transformation. The optimization of the cost function was performed in a hierarchical approach by decreasing the spacing between the mesh control points to align coarse to fine structures. The hierarchical optimization along with the smoothing term in the cost function provided smooth deformation fields and preserved the topology of the optic radiations. The registration operated on the binary masks of the segmented optic radiation from different subjects to align them with the binary mask of the reference optic radiation. The transformation fields for each subject were stored. Working with binary images made the registration independent from the diffusion tensors affected by glaucoma and focused on the shape similarity.

5.3.4 Statistical analysis

The transformation fields obtained from registration were used to transform the diffusion tensor-derived diffusivity parameters (axial, radial, and mean diffusivities) and FA to the unified space. This enabled voxel-wise comparison between the normal and glaucoma groups with regard to all examined parameters.

For each of the tensor-derived parameters, each voxel in the reference optic radiation was analyzed using nonparametric Wilcoxon rank sum test. A minimal smoothing was applied to the diffusion tensor indices prior to the statistical analysis using a 3×3 Gaussian filter with a standard deviation of 0.5. The voxels were considered to show a significant difference with respect to the parameter under investigation if the p-value (uncorrected for multiple comparisons) was less than 0.05 corresponding to 95% confidence interval.

5.3.5 Reliability assessment of the inter-operator configuration of the optic radiation

The manual configuration of the automatically segmented optic radiation is operator dependent. Inter-operator variabilities could arise leading to false significant regions. Thus, the inter-operator reliability needs to be evaluated. The automatically segmented optic radiation was demonstrated on the GUI created by the authors to two experts in the visual system neuroanatomy and diffusion tensor imaging. The experts performed independently the manual configuration of the optic radiation to remove the branching parts of the optic radiation to the primary visual cortex and to exclude

the LGN. The directional-color-coded images were used as the basis for the manipulation process with the possibility to examine the other tensor-derived indices maps or anatomical images. The operators utilized the GUI capabilities to threshold the anisotropy indices and to monitor the branching regions of the optic radiation for a systematic approach for the manual manipulation. The final optic radiations identified by both operators were compared using the percentage of voxel overlap [John 06] using the following equation:

$$Overlap(\%) = \frac{V_{ox1} \cap V_{ox2}}{V_{ox1}} \times 100 \tag{5.1}$$

where V_{ox1} and V_{ox2} are the processed optic radiations from the first and the second operators, respectively.

The percentage of voxel overlap along with the intersection to union ratio (IU-ratio) [John 06] as given by Eq. (5.2) were calculated for each subject and used to evaluate the reliability between operators.

$$IUratio(\%) = \frac{V_{ox1} \cap V_{ox2}}{V_{ox1} \cup V_{ox2}} \times 100 \tag{5.2}$$

A third alternative metric for assessing the matching between the manipulated optic radiations from the two operators was the modified Hausdorff distance (MHD) [Dubu 94]. The directed modified Hausdorff measure $d(A, B)$ between region A and region B is the average of the Euclidean distances between each point on the boundary of A to its nearest neighbor on the boundary of B. The modified Hausdorff distance is the maximum of the directed distances $d(A, B)$ and $d(B, A)$.

5.3.6 Evaluation of registration accuracy

An important aspect of the proposed framework is the ability of the registration algorithm to align the optic radiations from different subjects to the reference. The residuals of the registration were used to represent the degree of misalignment between the registered subjects and the reference. The overlap, the intersection to union ratio and the modified Hausdorff distance between the reference and the registered optic radiations were used as measures of the registration accuracy as well as the post-registration degree of alignment.

5.4 Results

DTI-brain scans of the subjects were performed. The proposed framework was applied to the DTI datasets and the significant regions were extracted. Figure 5.3 shows the reference optic radiation and the regions that indicated significant differences with respect to the FA, radial, and mean diffusivities.

The FA analysis showed that the glaucoma group had mainly significant voxels with decreased FA in comparison to the normal group. Moreover, the significant differences were located in the middle part with regard to anterior-posterior orientation of the optic radiation as shown in Figure 5.4. Radial and mean diffusivities had localized higher values in the glaucoma group than in the normal subjects. The

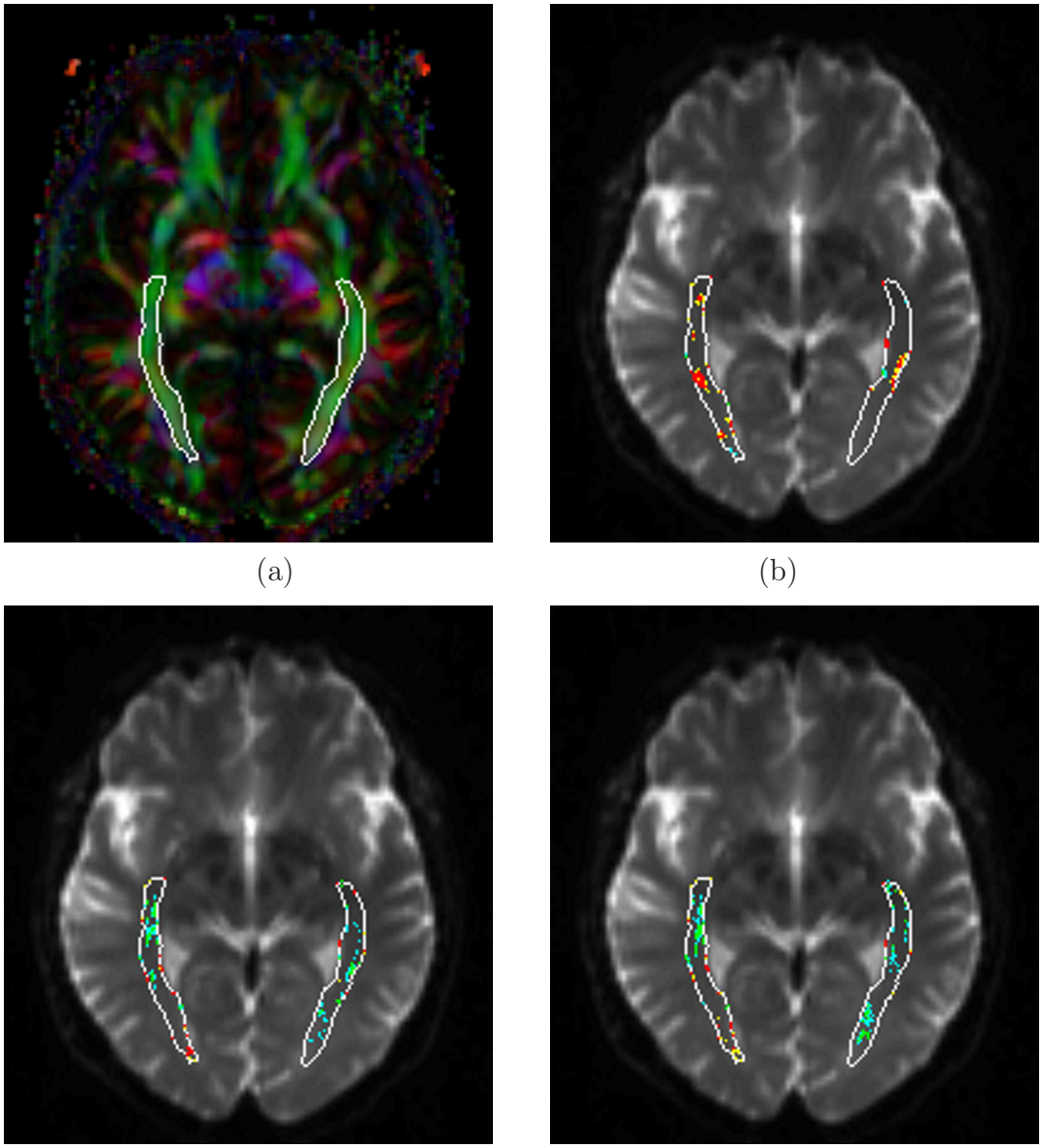

(a) (b)

(c) (d)

Figure 5.3: Optic radiation of the reference subject (a) and the significant optic radiation voxels based on the analysis of: (b) Fractional anisotropy (FA), (c) Radial Diffusivity (RD), and (d) Mean Diffusivity (MD) in the presence of glaucoma. The significant regions are marked and the color code is as follows: Red: control group's mean value greater than glaucoma group's mean value with p-value < 0.05, Yellow: control group's mean value greater than glaucoma group's mean value with $0.05 \leq$ p-value < 0.1, Green: control group's mean value less than glaucoma group's mean value with p-value < 0.05, Cyan: control group's mean value less than glaucoma group's mean value with $0.05 \leq p$-value < 0.1.

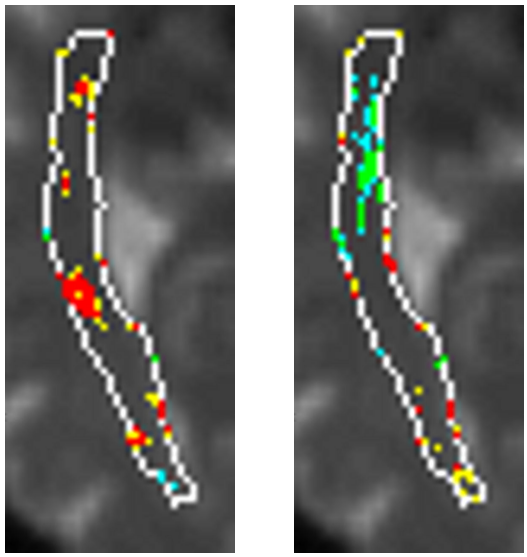

Figure 5.4: Concentration of significant regions on the right optic radiation according to the fractional anisotropy analysis (left) and according to the mean diffusivity analysis (right). Color code is as follows: Red: control group's mean value greater than glaucoma group's mean value with p-value < 0.05, Yellow: control group's mean value greater than glaucoma group's mean value with $0.05 \leq p$-value < 0.1, Green: control group's mean value less than glaucoma group's mean value with p-value < 0.05, Cyan: control group's mean value less than glaucoma group's mean value with $0.05 \leq p$-value < 0.1.

proximal part of the right optic radiation near the Meyer loop contained a concentration of significant voxels with increased radial and mean diffusivities. In addition, a significant abnormality region could be observed in the posterior part of the left optic radiation with regard to MD analysis. This region was characterized as well by increased MD. Figure 5.4 focuses on the optic radiation to show the concentration of voxels with increased MD values in the proximal part. The effect on the AD was scattered and no remarkable localization could be detected (not shown).

5.4.1 Inter-operator configuration of the optic radiation reliability results

The overlap, IUratio and the MHD of the two experts processed optic radiations were calculated for each subject. The mean and the standard deviation (SD) were calculated for the glaucoma, control groups and all subjects. The results of the reliability analysis are summarized in Table 5.1. Table 5.1 shows that the mean overlap in all groups was more than 88%. The correlation between operators as measured by overlap among all subjects is 93.41% with a standard deviation of 5.62%. Subvoxel agreement between operators was indicated by a Hausdorff distance of 0.43 mm for all subjects.

Table 5.1: Reliability analysis of the inter-operator configuration of the optic radiation

Group	Overlap(%)		IUratio(%)		Modif. Hausdorff(mm)	
	Mean	SD	Mean	SD	Mean	SD
Glaucoma patients	96.82	2.66	90.22	3.82	0.29	0.13
Normal subjects	88.97	5.38	85.05	5.21	0.61	0.39
All subjects	93.41	5.62	87.98	5.09	0.43	0.31

Table 5.2: Registration accuracy analysis

Group	Overlap(%)		IUratio(%)		Modif. Hausdorff(mm)	
	Mean	SD	Mean	SD	Mean	SD
Glaucoma patients	94.69	2.25	89.38	3.95	0.34	0.13
Normal subjects	93.21	1.55	87.36	1.92	0.41	0.07
All subjects	93.85	1.98	88.24	3.07	0.38	0.11

5.4.2 Registration accuracy evaluation results

The registered optic radiations from all subjects were overlaid on the reference optic radiation. The overlap, IUratio and MHD were calculated for all individual subjects. Table 5.2 demonstrates the results of the accuracy analysis. The mean residuals (complement of the overlap) from the registration of all subjects did not exceed 7%. For the glaucoma and normal groups, the IUratio means were 87.36% and 89.38%, respectively. A maximum MHD of 0.41 mm for the normal group indicated the subvoxel degree of alignment achieved.

5.5 Discussion

The presented framework provides localized abnormality maps of the optic radiation in glaucoma. The application to groups of normal and glaucoma subjects indicates the potential localization capabilities of the system. Furthermore, the system analyzes different relevant diffusion tensor parameters characterizing different properties of the underlying white matter fiber structure of the optic radiation. Thus, regional structural changes of the underlying white matter in the presence of glaucoma could be investigated.

Complexity of the white matter architecture of the human visual system and its variability among subjects complicate the voxel-based analysis. Common VBM approaches aiming to match the highly variable complete brain fiber structure, such as the implementation in statistical parametric mapping (SPM) - (Wellcome. Department of Cognitive Neurology, University College. London, London, UK) and TBSS [Smit 06], face the challenge of large registration residuals and misalignments. Therefore, whole brain analysis is avoided. Object oriented analysis (e.g., the work by Xu et al. [Xu 02] to analyze the callosal fibers) concentrating on a single object reduces the matching complexity from the whole brain to a specified object. The object oriented approach is adopted in this work with the optic radiation as the object to be analyzed. Using tractography to identify the white matter fibers results in a network of individual fibers which is highly dependent on the user intervention

for selecting the seed points or regions of interest. Additionally, the reconstructed fiber tracts may need to be clustered in order to provide fiber bundles. This could lead to another source of errors and affects the voxel-wise comparison. Therefore, a segmentation technique is used for the reconstruction of the optic radiation. So, the optic radiation is represented as a segmented region which facilitates the registration and reduces the sources of errors.

The validity of the results produced by the framework depends on the accurate identification of the corresponding optic radiation regions in all subjects, the consistency between operators, and the ability to efficiently align the optic radiations to the reference. Therefore, the validation of these issues is crucial to the reliability of the results and to indicate the system efficiency. The optic radiation has a highly complex fiber system [Ture 00, Sinc 04] that makes the identification and isolation of its fiber structure a difficult task. This problem is mitigated by restricting the analysis to the main coherent fiber bundle of the optic radiation. The utilized segmentation algorithm targets the coherent bundle. This is emphasized by the anisotropic filtering and the initialization of the optic radiation using a FA threshold of 0.3. The FA threshold primarily aims to avoid the inclusion of voxels with intravoxel fiber orientational heterogeneity [Tuch 02] and to disconnect the optic radiation from interfering tracts by the attempt to exclude the voxels representing crossing and branching situations. Moreover, the manual configuration procedure ensures that corresponding optic radiation bundles from different subject are to be compared. i.e., the coherent optic radiation bundles following the LGN and projecting to the primary visual cortex (without the heterogeneous branching tracts) on the LGN-slice.

The optic radiation is automatically determined to eliminate the necessity of user intervention. The manual configuration of the optic radiation is performed by two experts in a simple systematic approach. The LGN is clearly located at the termination region of the optic tract and the beginning of the visual pathway axons projecting to the visual cortex through the identified optic radiation. The branching fibers of the optic radiation near the posterior end of the optic radiation are located in the proximity of the primary visual cortex. The fiber structure in branching and crossing situations is characterized by reduced anisotropy due to the limitation of the diffusion tensor model. Thus, increasing the anisotropy threshold gradually and monitoring the branching region can facilitate the systematic elimination of the highly variable branching bundles. However, the user intervention in this region is limited because the output from the automated segmentation consists mainly of the coherent fiber bundle of the optic radiation. Following these approaches in manually configuring the optic radiation, a high degree of consistency between operators is achieved. Subvoxel inter-operator agreement measured by the modified Hausdorff distance can be attributed to the minimized intervention of operators in the LGN and near the posterior end of the optic radiation. This leaves the majority of the optic radiation unaltered and reduces the average shape deviation.

The robust semi-automated identification of the optic radiation and relying on the remarkable shape similarity for the registration contribute to the high degree of structure alignment. An average overlap between reference and registered optic radiation of greater than 93% is achieved with a subvoxel accuracy of 0.4 mm. Furthermore, glaucoma has been shown to affect tensor-derived parameters such as FA and MD

in the optic radiation [Gara 09] which in turn affects the whole tensor. Thus, the dependence on the tensor or tensor-derived measures in the registration could result in inconsistency of the analysis among different parameters. This issue is resolved by depending on the segmented optic radiation shape similarity among subjects with and without glaucoma. A registration based on shape similarity ensures consistency when using the obtained transformations to transfer any tensor-derived parameters to the unified space for voxel-wise comparisons.

The decreased FA values of the glaucoma group indicate that the fiber coherence and directionality of water self-diffusion are degraded compared to the normal group. This could be related to an impaired integrity of white matter tracts as suggested by previous studies [Pier 96a, Hors 02, Hami 08]. The concentration of the significantly decreased FA voxels in the middle between the anterior and posterior parts of the optic radiation demonstrates the localized glaucoma effect in that region. The water diffusion in the direction perpendicular to the PDD is thought to be restricted by the myelin sheaths and the axonal cell membranes [Beau 02]. This transverse diffusion is represented by the RD. The process of demyelination in the presence of neurological pathologies was suggested to be associated with increased RD by Song et al. [Song 03, Song 05]. The increased radial diffusivity in the glaucoma group concentrated in the proximal part of the right optic radiation suggests a possible demyelination process near the Meyer loop. Mean diffusivity represents the average of the water self-diffusion which is related to the obstacles restricting the diffusion. The locations of significant increase in MD are similar to the results from the RD analysis on the right optic radiation. However, an additional major abnormality area can be located in the posterior part of the left optic radiation.

The localization analysis shows approximately symmetric regions on both the middle parts of the left and right optic radiation with respect to FA analysis. However, the abnormalities on the left optic radiation are differently located than the abnormalities on the right optic radiation regarding the RD and MD analyses. The asymmetry in the RD and MD results could be attributed to the hemispheric white matter asymmetry reported previously [Pele 98, Park 04]. Moreover, glaucoma is commonly an advanced age disease [Tuck 98]. This is reflected in the selection and age matching of the subjects in this study. Aging is associated with brain atrophy which was shown to be asymmetric in both brain hemispheres [Dolc 02, Arde 07]. As a part of the white matter, the optic radiation could be concerned with the hemispheric asymmetry. Another factor affecting the symmetry of the results could be the limited spatial resolution of the DTI modality which makes the asymmetric acquisition of a complex fiber structure with variable course such as the optic radiation [Hofe 10] unavoidable.

Recently, the average FA and MD in the optic radiation was reported to be decreased and increased, respectively in the presence of glaucoma [Gara 09]. The performed analysis is generally in agreement with these findings and additionally provides a localization map of the deleterious effect of glaucoma on the optic radiation.

The selection of the slice that represents the optic radiation and the manual post-processing may influence the results of the analysis. This influence is reduced by co-registering the DTI images with the anatomical MRI images for the validation of the segmentation and slice selection. However, the slice selection is done by two

DTI experts to ensure consistency and reliability of the selection. The small sample size used in this study restricts a strong conclusive statement about the localization results of differences in diffusivity and anisotropy parameters between the normal and glaucoma groups. Potential significant voxels with p-value ≥ 0.05 and < 0.1 are also shown in Figure 5.3 and Figure 5.4. The significant regions corresponding to a p-value ≥ 0.05 and < 0.1 are in the neighborhood of the 0.05 p-value analysis regions as shown in Figure 5.4. Nevertheless, the focus of this work is on the localization framework.

Chapter 6

Glaucoma Classification Using Visual Pathway Analysis

The classification using visual pathway analysis concept along with preliminarily results were published in

A. El-Rafei, T. Engelhorn, S. Waerntges, A. Doerfler, J. Hornegger, and G. Michelson. "Glaucoma Classification Based on Histogram Analysis of Diffusion Tensor Imaging Measures in the Optic Radiation". In: Real P,Diaz-Pernil D, Molina-Abril H, Berciano A, Kropatsch W, editors. Computer Analysis of Images and Patterns, Lecture Notes in Computer Science, pp. 529-536, Berlin: Springer, 2011.

6.1 Introduction

The current methods for glaucoma detection target the retina, or more generally the eye, as indicated in Section 2.4. Images can be obtained that show the structure of the retina. Analysis is performed on these images to capture the glaucomatous morphological changes. The information provided by the imaging modalities was the basis of various systems and algorithms that were developed to screen and detect glaucoma [Mede 04]. Bock et al. proposed the glaucoma risk index (GRI) for screening glaucomatous eyes [Bock 10]. The system is based on processing fundus images and extracting the classification features from the optic disc. Appearance-based features of the optic disc were used which included pixel-intensities, Fourier coefficients, and interpolating spline coefficients. Principal component analysis (PCA) reduced the number of features to be considered in each features category. Finally, a two-stage classification setup is utilized. The achieved accuracy with this system was 80% and an area under the Receiver Operating Characteristic (ROC) curve of 0.88. Heidelberg retina tomograph III provides a glaucoma probability score (GPS) and Moorfields regression analysis (MRA). The GPS score is the result of a classification based on the morphological parameters measured by HRT-III. The HRT-III analysis differentiated between glaucoma and normal subjects with a maximum area under the ROC curve (AUC) of 0.934 in [Burg 07]. The RNFL thickness in different quadrants were investigated for glaucoma diagnosis in [Lu 08]. The highest AUC was 0.92. In a preliminarily study, it was shown that using OCT parameters and a support vector machine (SVM) classifier, 0.98 AUC can be achieved for glaucoma class recog-

nition [Burg 05]. However, the determination of the degree and type of glaucoma can not be achieved efficiently using a single type of analysis. Furthermore, the screening and the damage prediction need to be improved, which are essential to the preventative treatment of the disease. The pathological process of glaucoma suggests the inclusion of the visual pathway information in the examination flow. Therefore, we propose a classification system for glaucoma that is based on the aspects of the optic radiation tracts in this chapter.

A system for the classification of different entities of glaucoma is proposed. The system is based on DTI-derived measures that are related to the status of the white matter architecture and can, therefore, detect fiber disorders. Moreover, a feature ranking algorithm is used to investigate the importance of the different DTI-derived parameters in classifying different entities of glaucoma. Previously, the authors have investigated the ability of visual pathway analysis to differentiate between healthy subjects and patients having POAG using only a set of histogram features. The preliminarily results were presented in [El R 11c]. In this chapter, we extend the analysis to three groups of subjects: Healthy, POAG, and NTG. The aim is to determine the sensitivity of the different DTI derived parameters in detecting different types of glaucoma as well as the efficiency and generalization of the system. In addition, the feature set is enlarged to include various texture features that can be categorized into three feature sets: Histogram, co-occurrence matrix, and Laws features. This will lead to a highly improved classification rates which will be shown in the results section. The classification of glaucoma using visual pathway analysis represents a novel perspective in glaucoma diagnosis. It could lead to significant improvements in the clinical flow and consequently the therapy of glaucoma.

6.2 Materials

6.2.1 Subjects

The system was applied to a group of control subjects and a group of glaucoma patients. The glaucoma group was further divided into two categories representing two types of glaucoma. The first type was POAG and the second was NTG. The POAG category included 39 patients (19 females and 20 males) with an average age (mean $\pm$ SD) of 61.74 ± 8.32 years while the NTG group consisted of 18 patients (13 females and 5 males) with an average age of 62.33 ± 9.44 years. This resulted in a total of 57 glaucoma patients with an average age of 61.93 ± 8.61 years. The identification of OAG was performed by ophthalmological examinations. The patients of OAG were characterized by an open anterior chamber angle, cupping of the optic disc, and visual field defects > 2 dB. The untreated IOP was measured and used to differentiate between POAG and NTG patients where POAG patients were associated with an elevated IOP > 21 mmHg while NTG subjects had normal IOP < 21 mmHg. Twenty seven normal subjects constituted the control group (17 females and 10 males) with an average age of 58.52 ± 10.10. The three different categories were age matched to exclude the aging effects from the analysis. Table 6.1 summarizes the different groups. The subjects were selected randomly from the patients in the clinic of the Department of Ophthalmology at the University Erlangen-Nuremberg. The control

Table 6.1: Categories of subjects

Group	Subjects	Age		Sex	
		Mean	SD	Male	Female
Glaucoma	57	61.93	8.61	25	32
POAG	39	61.74	8.32	20	19
NTG	18	62.33	9.44	5	13
Control	27	58.52	10.1	10	17
All subjects	84	60.83	9.2	35	49

group was examined and did not show an impairment of the neuronal parts of the visual system. Moreover, the brains of the subjects were scanned to produce MRI and DTI datasets. These datasets were examined by neuroradiologists to check for any abnormalities in the optic radiations and to exclude patients with cerebral diseases.

6.2.2 Brain imaging

MRI and DWI-images were acquired for the subjects involved in this work using the same acquisition protocols in Chapter 5. The high resolution T1-weighted images were utilized for the anatomical examinations. This included the validation of the automatic segmentation and manual configuration of the optic radiation in addition to the detection of other cerebral diseases or abnormalities in the visual pathway. Diffusion-weighted images are used for optic radiation identification and for feature extraction.

6.3 Methods

The proposed classification system processes the diffusion weighted images to calculate the diffusion tensors and their derived parameters. The optic radiation is automatically segmented to minimize the operator intervention. Then, a specified region of interest (ROI) on the segmented optic radiation is manually identified. Different diffusion tensor derived measures are used for the extraction of features. For each DTI-measure, statistical based features including histogram, co-occurrence matrix, and Laws features are computed on the selected ROI. The features are then ranked to determine the best discriminating features between the diseased and the normal groups. An SVM classifier with a recursive feature elimination technique is utilized for feature ranking. The high performing feature sets are the input to an SVM classifier to identify the different groups. The system is applied to three different categories of subjects: control, POAG, and NTG groups. The classification accuracy of the system is evaluated using a 10-fold cross validation scheme and the most significant features for differentiating between the different groups are determined. In Figure 6.1, the flow and the various steps of the system are demonstrated.

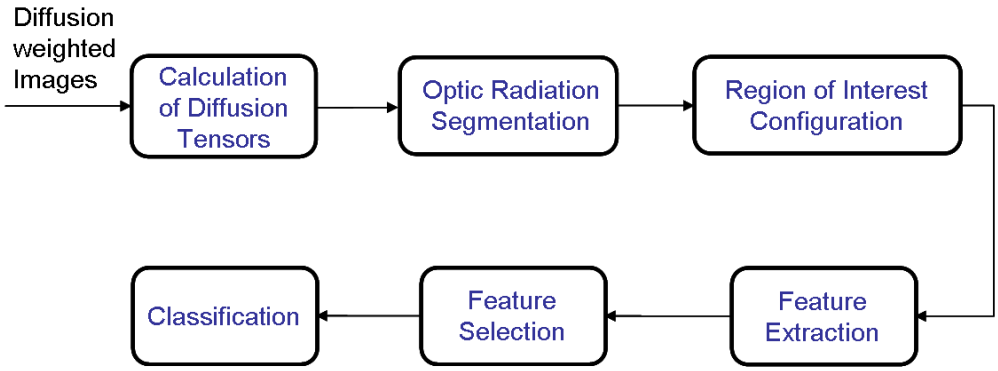

Figure 6.1: Schematic of the classification system. The system discriminates glaucoma patients from healthy subjects by features extracted from the diffusion tensor derived parameters of the optic radiation. The different stages of the system are illustrated in the schematic.

6.3.1 Semi-automated identification of the optic radiation

The automatic segmentation and region of interest configuration of the optic radiation are very similar to the procedure followed in Chapter 5. Therefore, they are combined in this subsection and the differences are highlighted. The eigenvectors and eigenvalues of the tensors are computed. The eigenvalues are used to calculate FA, AD, RD, and MD. The main diffusion direction is the PDD described by the major diffusion ellipsoid axis. The system we presented in Chapter 4 is used for delineating the optic radiation automatically. It is worth mentioning that the initialization alone provided accurate segmentations in many subjects that were sufficient for proceeding with the manual ROI selection. However, in some cases it was necessary to evolve the level set to obtain the appropriate delineation.

The manual ROI determination followed approximately the same steps demonstrated in the previous chapter. This is performed in two manual steps: First, the optic tract is traced and its intersection with the optic radiation at the LGN is identified. Then, the axial slice that contains the largest part of the LGN is selected for additional processing. Second, the segmentation is examined and matched to a DTI-white matter atlas by two DTI-experts. Based on the examination, the segmentation errors are corrected. The optic radiation branches near its distal end to the primary visual cortex are removed from the analysis to avoid the inclusion of voxels with wrongly reduced anisotropy. In the case of the VBM analysis, shape similarity was the important factor. Therefore, LGN was eliminated from the analysis. For classification purposes, LGN is retained as a part of the visual system. In Figure 6.2, an example of a configured ROI is shown on an FA image. This process is aided by the GUI developed by the author for segmentation modification in a standard manner. This reduces the inter-operator variability and ensures the consistency of the selected ROI.

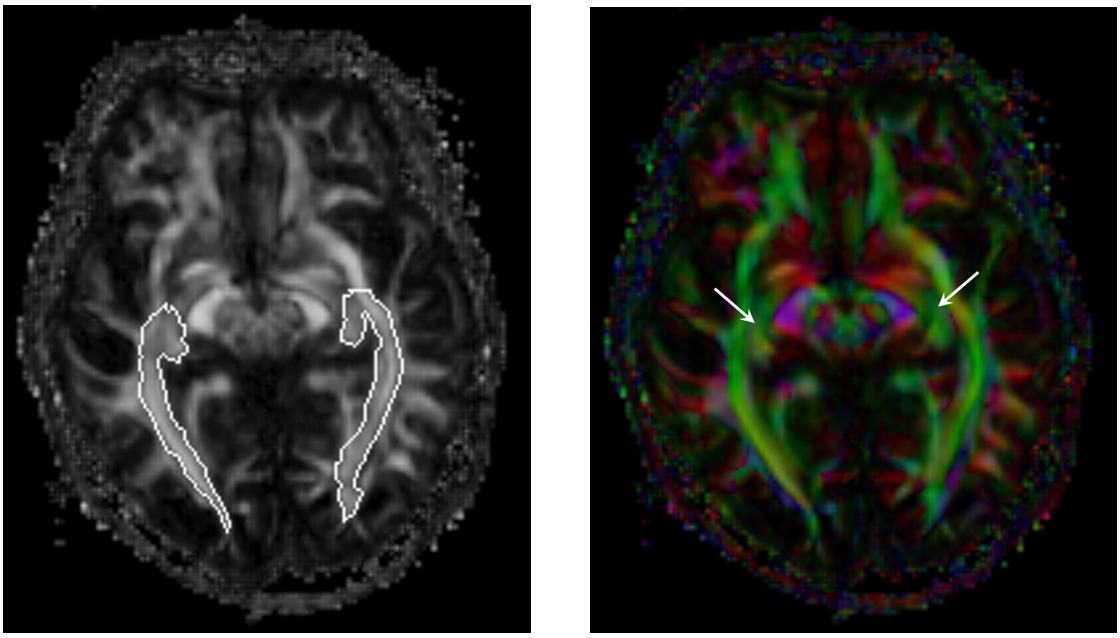

Figure 6.2: Region of interest (ROI) identified on the optic radiation demonstrated on a fractional anisotropy image (left). The diffusion direction coded ROI-axial slice (right) indicates the main anterior-posterior diffusion direction in the optic radiation. The intersection of the optic tracts and the optic radiation in the lateral geniculate nuclei is clear and shown by white arrows on the selected slice on the right image.

6.3.2 Assessment of the inter-operator reliability for region of interest configuration

An important aspect in evaluating the reproducibility of the classification system is the reliability of the ROI configuration among operators. This is important because, it is the only step that requires manual intervention from users. Some of the subjects involved in this analysis are different than the subjects in Chapter 5. In addition, the LGN structure is not removed in this work and, therefore, can reduce the inter-user reliability. Therefore, the reliability assessment is necessary in spite of the systematically followed procedure in delineating the ROI and the developed GUI. The GUI usage and the ROI identification procedure are explained to two experts. Then, twenty subjects were randomly selected and the two experts were requested to perform the manual ROI delineation on these 20 subjects independently. The selected subjects included 8 POAG, 5 NTG, and 7 healthy subjects. This includes the correction of segmentation errors as well as the removal of the branching segments of the optic radiation near its distal end. The degree of agreement between the operators is measured using the percentage of voxel overlap given by Equation 5.1 and MHD (See Section 5.3.5).

6.3.3 Feature Extraction

Statistical features are extracted from diffusion tensor derived parameters on the configured ROI. The utilized DTI measures are: (1) three diffusivity parameters:

AD which represents the diffusion along the fiber, RD is the average diffusion in the direction normal to the fiber, and MD is the average diffusion within a voxel. (2) An anisotropy index (FA) which is related to the intravoxel fiber coherence and integrity as it measures the degree of anisotropy. FA ranges from zero for an isotropic diffusion to one for a perfect anisotropic diffusion. (3) Fiber orientation parameters based on the PDD. The PDD has three Cartesian components along the three coordinate axes and has a length of unity as it represents a direction. By transforming the PDD to the spherical coordinates, we can exclude the radial component since its value is always one. Thus, it reduces the PDD variables to the azimuth and inclination angles. Moreover, due to the symmetry of the diffusion tensor, the sign of the PDD does not correspond always to the actual diffusion direction. Therefore, the azimuth and inclination angles are confined to fall in the range of 0-180 degrees by reversing the PDD direction in case of pointing outside this range. This results in a total of six medically relevant parameters describing fiber aspects of the optic radiation. The features extracted from each DTI-parameter can be categorized based on the order of the statistical features. i.e., the degree of spatial interaction between image voxels. The histogram group corresponds to the first order statistical features computed on the basis of individual voxels. Co-occurrence matrices [Hara 73] represent the second category and are distributions of patterns considering the values of two voxels at specific relative spatial location. The third group is the Laws energy features which is a higher order statistical features by examining the relation between more than two voxels [Laws 80]. In the following subsections we describe each category.

Histogram features

The range of the DTI-derived measures is divided into a number of bins. The number of voxels in each bin is counted and the histograms are obtained. The histograms are divided by the number of voxels in the ROI to give the probability of occurrence. The histograms are computed from the values of the individual voxels and do not take the spatial relation into account. Therefore, the histogram features are first order statistical features. The mean, variance, skewness, kurtosis, energy, and entropy are the six features derived from the histograms resulting in a total of 36 features (6 DTI-measures $\times$ 6 histogram features). Equations (6.1-6.6) provide the mathematical formulation of the histogram features. The mean is the average parameter value while the variance measures the deviation from the mean. Skewness is the third central moment and measures the symmetry around the mean of the histogram with a negative skewness if the histogram is skewed to the left and a positive skewness if it is skewed to the right. The kurtosis measures the deviation of the histogram from the normal distribution having equivalent variance with regard to peakedness. The energy is the sum of squared probabilities. The Energy reaches its minimum for a flat histogram and describes the intensity variations within the ROI. The entropy corresponds to the histogram uniformity.

$$Mean : \mu = \sum_{i=1}^{N} param(i) \times hist(i) \tag{6.1}$$

$$Variance : \sigma^2 = \sum_{i=1}^{N} (param(i) - \mu)^2 \times hist(i) \tag{6.2}$$

$$Skewness : \mu_3 = \sigma^{-3} \sum_{i=1}^{N} (param(i) - \mu)^3 \times hist(i) \tag{6.3}$$

$$Kurtosis : \mu_4 = \sigma^{-4} \sum_{i=1}^{N} (param(i) - \mu)^4 \times hist(i) - 3 \tag{6.4}$$

$$Energy : E = \sum_{i=1}^{N} hist(i)^2 \tag{6.5}$$

$$Entropy : H = -\sum_{i=1}^{N} hist(i) \log(hist(i)) \tag{6.6}$$

where the number of bins in the DTI-parameter histogram is N, the normalized histogram is *hist* (i.e. probability distribution which is the histogram divided by the total number of voxels within the ROI), i is the index of the ith bin, and $param(i)$ is the mean value of the corresponding parameter (*param*) in the ith bin.

Gray-level co-occurrence matrices features

The gray-level co-occurrence matrix (GLCM) proposed by Haralick et al. [Hara 73] of an image takes into account the spatial dependences on a two pixels basis. It calculates the distribution of gray level values co-occurring at two points separated by a certain offset. GLCM is a square symmetric matrix where the rows and columns correspond to the gray levels in the image or identified ranges of gray levels. The ij-element of the matrix represents the number of occurrences of gray level corresponding to row i and the gray level corresponding to column j for a given spatial offset. In Figure 6.3, an example offset is illustrated. This offset is commonly described by a distance and an angle along which the distance is measured. The GLCMs of all the six DTI-measures are computed with an offset distance of one pixel and along four angles 0°, 45°, 90°, and 135°. The contrast, correlation, angular second moment (ASM), and homogeneity are statistical measures derived from the GLCMs resulting in 96 features for the six DTI-parameters. Before the calculations of the statistical parameters, the GLCM is normalized so that the sum of the matrix elements is one and the values represent the joint probability of occurrence. Also, the analysis is restricted to the defined ROI. The contrast reflects the degree of local intensity variations in the ROI. Correlation expresses the relation and dependency between the gray levels and the neighboring. The squared sum of the probabilities is the ASM while the deviation of the matrix from its diagonal is inversely proportional to the homogeneity. All derived statistics are summed over the whole ROI or equivalently over the GLCM as given by the following equations:

$$Contrast = \sum_{i=0}^{G-1} \sum_{j=0}^{G-1} (i - j)^2 p(i, j) \tag{6.7}$$

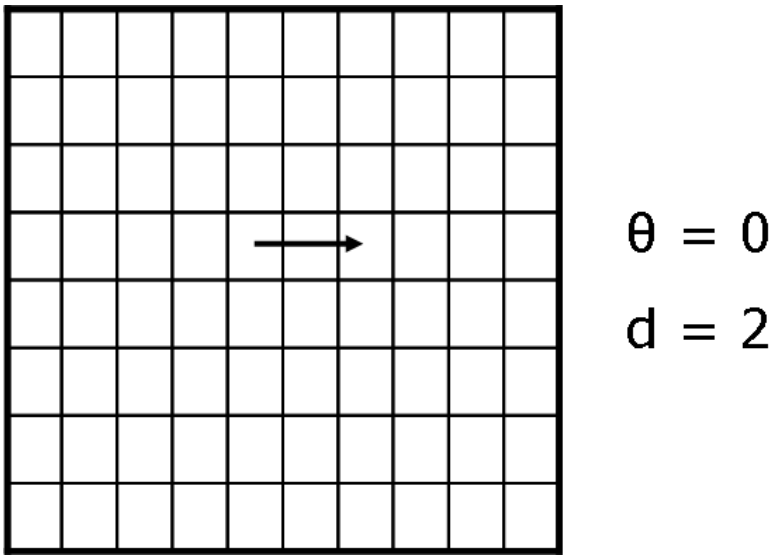

Figure 6.3: The offset associated with the gray-level co-occurrence matrix shown on an image grid. In this case, the offset is represented by an angle (θ) = 0 and a distance (d) of two pixels.

$$Correlation = \sum_{i=0}^{G-1}\sum_{j=0}^{G-1}\frac{(i-\mu_i)(j-\mu_j)p(i,j)}{\sigma_i\sigma_j} \tag{6.8}$$

$$AngularSecondMoment(ASM) = \sum_{i=0}^{G-1}\sum_{j=0}^{G-1}[p(i,j)]^2 \tag{6.9}$$

$$Homogeneity = \sum_{i=0}^{G-1}\sum_{j=0}^{G-1}\frac{p(i,j)}{1+|i-j|} \tag{6.10}$$

where i and j are the gray levels (indices) of the i^{th} row and the j^{th} column ranging from zero to $G-1$, respectively. $p(i,j)$ are the joint probability of i and j given by the ij-element of the normalized GLCM. μ_i and σ_i are the mean and the standard deviation of the rows sums of the GCLM while μ_j and σ_j are the equivalents for the columns sums.

Laws texture energy features

Higher order statistical features examine the spatial relation between image points on more than two pixels scale. Laws energy features belong to this category [Laws 80]. The five following one-dimensional kernels were devised by Laws to correspond to average gray level (L), edge (E), spot (S), wave (W), and ripple (R):

$$
\begin{aligned}
Level : L5 &= [\ 1 \ \ 4 \ \ 6 \ \ 4 \ \ 1] \\
Edge : E5 &= [-1 \ \ -2 \ \ 0 \ \ 2 \ \ 1] \\
Spot : S5 &= [-1 \ \ 0 \ \ 2 \ \ 0 \ \ -1] \\
Wave : W5 &= [-1 \ \ 2 \ \ 0 \ \ -2 \ \ 1] \\
Ripple : R5 &= [\ 1 \ \ -4 \ \ 6 \ \ -4 \ \ 1]
\end{aligned}
$$

Twenty five two-dimensional kernels are obtained from the convolution of the one-dimensional kernels with each other and with themselves. This is performed by convolving one vertical kernel with one horizontal kernel. These 25 kernels are then convolved with the DTI-derived parameters' images to produce 25 images for each DTI-parameter. This is accomplished by replacing the value of a pixel at a certain location with the result of applying one of the convolution kernels at this location. The texture energy is evaluated for each kernel by locally applying a 3×3 average filter resulting in 25 energy images. The dual energy images that are calculated from the same one-dimensional kernels regardless of the order of the convolution (e.g., L5S5 and S5L5) are averaged. This leads to rotational invariant features and reduces the number of energy images to 15 images. Finally, the mean, variance, and energy range on the ROI for each DTI-measure are computed and used as features. The total higher order statistical features are 270 features.

6.3.4 Feature selection and classification

The combined feature vector contains 36 histogram features, 96 GLCM features, and 270 Laws energy features which are summed to 402 features from the six DTI-derived measures under consideration. In this step, we apply a feature ranking algorithm to determine the most discriminating features in differentiating the different subjects' groups (i.e., healthy subjects and patients having different types of glaucoma). The utilized algorithm ranks the features by recursive feature elimination [Guyo 02]. The criterion for determining the feature to be excluded is the squared weight of the feature evaluated by an SVM classifier. It operates on the complete feature set by performing the following steps: (1) an SVM classifier is trained and the weights of the features are calculated. (2) The squared weights are examined and the feature corresponding to the smallest squared weight is marked and placed at the bottom of the ranked feature list. (3) The marked feature from the previous step is excluded from the feature set. (4) Steps(1-3) are applied to the remaining features and the procedure is repeated iteratively until the ranking of the entire feature set is accomplished. After the feature ranking, a search is performed on the ranked feature list to determine the optimal number of features and the classifier to be used in the classification. The result of this analysis is the selection of an SVM classifier for subjects' classes identification. The number of used ranked features differs based on the subjects' groups being investigated and will be detailed in the results section. The classification performance is tested using 10-fold cross validation. The feature ranking as well as the classification are performed using the software implementation of the algorithms in Weka [Hall 09].

Table 6.2: The number of classification features categorized according to their DTI-derived parameter for the different group pairs

Groups	#Features	FA	MD	AD	RD	THETA	PHI
Normal vs. G	33	2	7	10	3	5	6
Normal vs. POAG	53	6	10	15	7	8	7
Normal vs. NTG	28	5	1	4	4	6	8
NTG vs. POAG	52	12	9	15	9	3	4

The previous analysis may introduce selection bias as all the samples are included in the feature selection during the cross validation [Saey 07]. Thus, the classification rates can be overestimated. However, the aim of this evaluation is to provide a single set of ranked features for each group pair and to give an indication of the corresponding classification performance. An alternative approach is used that should result in an almost unbiased classification accuracy [Wood 07]. In this approach, 10 fold cross validation is performed. A single fold is used for testing while the remaining 9 folds are utilized for feature ranking and model determination. Stratified sampling is applied for data division into folds. i.e., the samples belonging to the same class are divided into folds separately and then added to form the final folds. This keeps approximately the same ratio of the classes in the training and testing subsets with respect the entire sample set. The aforementioned feature ranking methodology and SVM classifier are incorporated. This step is repeated 10 times so that all the folds are used for testing. The classification performance in each step is calculated. The correctly identified subjects as well as the misclassified subjects in each class from all the steps are concatenated to evaluate the overall accuracy.

6.4 Results

The ability of the classification system to differentiate between healthy subjects and glaucoma (POAG and NTG) patients is investigated. Moreover, the most significant DTI-parameters in distinguishing the normal class from different entities of glaucoma are identified. This is performed by the application of the system twice, once to the normal group against the POAG group and once to the normal group against the NTG group. The discrimination between different glaucoma types is examined by considering the POAG and the NTG groups. For the four aforementioned system applications, the distribution of the most significant features that lead to the best classification with respect to their DTI-measures is recorded in Table 6.2. Graphical representations of these distributions are shown in Figures 6.4(a)-6.7(a), the system performance is evaluated by the area under the ROC curve, classification accuracy (ACC), and Sensitivity/Specificity values as indicated in Table 6.4. The ROC curves are plotted in Figures 6.4(b)-6.7(b). The unbiased accuracy and Sensitivity/Specificity pairs are presented in Table 6.5. The results section is divided into four main subsections corresponding to the group pairs under investigation. An additional subsection is added for the inter-operator reliability analysis.

Table 6.3: Assessment of the inter-operator reliability of the optic radiation manual configuration

Group	Subjects	Overlap(%)		Modified Hausdorff(mm)	
		Mean	SD	Mean	SD
All subjects	20	92.94	6.61	0.80	0.95

6.4.1 Inter-operator reliability analysis of the ROI identification

The overlap and the MHD between the manipulated optic radiations from both operators were calculated for the twenty randomly selected subjects. The mean and the standard deviation of the overlap and the MHD among all sample subjects are computed and used as reliability measures. Table 6.3 summarizes the results of the reliability assessment. The mean overlap was 92.94% and the corresponding standard deviation was 6.61%. A mean MHD of 0.80 mm in comparison to an interslice resolution of 1.8×1.8 mm^2 indicates an average subvoxel agreement between operators.

6.4.2 Healthy vs. glaucoma

Thirty nine POAG patients were added to 18 NTG patients to form the glaucoma group that contained 57 subjects. The number of features that led to the highest classification accuracy of 94.05% and an AUC of 0.97 was 33 features. At a specificity of 96.30%, the sensitivity was 92.98%. The features categories are demonstrated in Figure 6.4b. Features extracted from MD and AD accounted for 51% of the classification features. The unbiased accuracy was approximately 9.5% lower than that of the single set of features at 84.52%. The sensitivity was 94.74% corresponding to 54 glaucoma patients being accurately recognized while the specificity was 62.96% corresponding to 17 subjects correctly associated with the normal class.

6.4.3 Healthy vs. primary open angle glaucoma

The ranked features according to the discrimination ability of healthy subjects from POAG patients that were selected as features for the classifier amounted to 53 features. As in the previous case, MD and AD represented the highest two contributions in the feature set with 25 features (47%) as indicated in Figure 6.5b. The accuracy of identifying the subjects' corresponding class was 92.42% with 36 glaucoma and 25 control subjects correctly classified and 5 subjects being wrongly classified (2 controls and 3 POAG patients). The AUC was 0.96 with a sample sensitivity/specificity of 92.31%/92.59%. The selection bias was estimated to be 10.6% and the classification error was increased to 18.18% instead of 7.58% in the biased case. Misclassification cases were 7 controls and 5 POAG patients resulting in modified a sensitivity/specificity of 87.18%/74.07%.

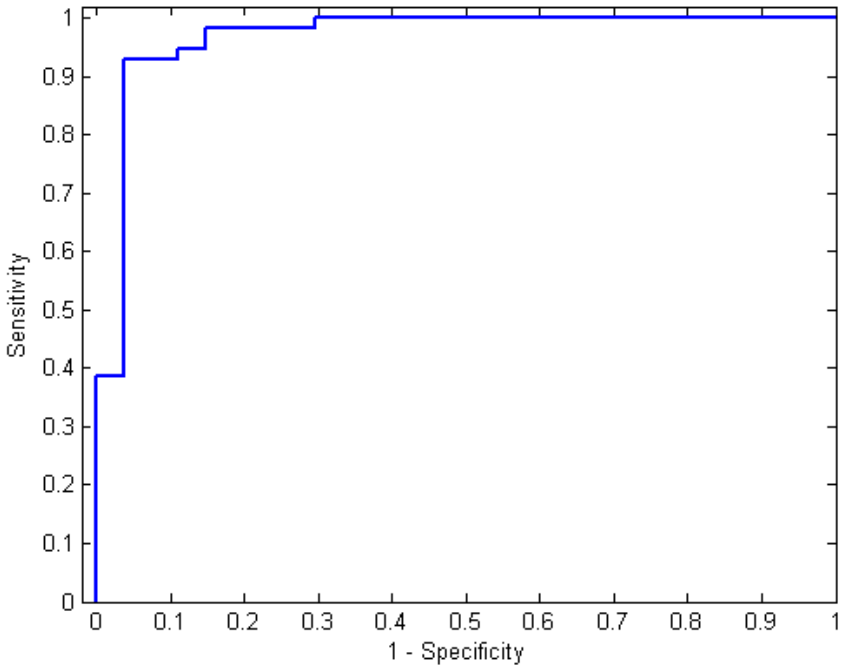

(a)

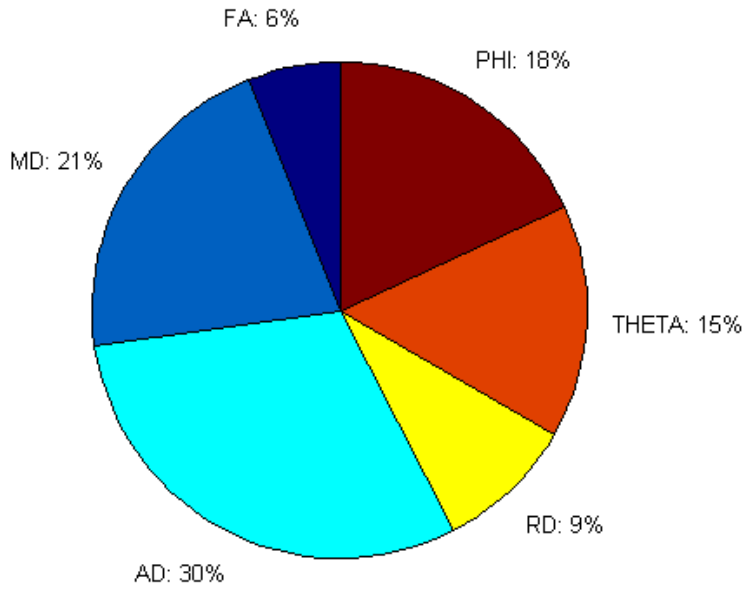

(b)

Figure 6.4: The distribution of classification features based on the DTI-derived measures for the healthy vs. glaucoma groups (a) and the ROC curve of the classification with an area under the curve of 0.97 (b)

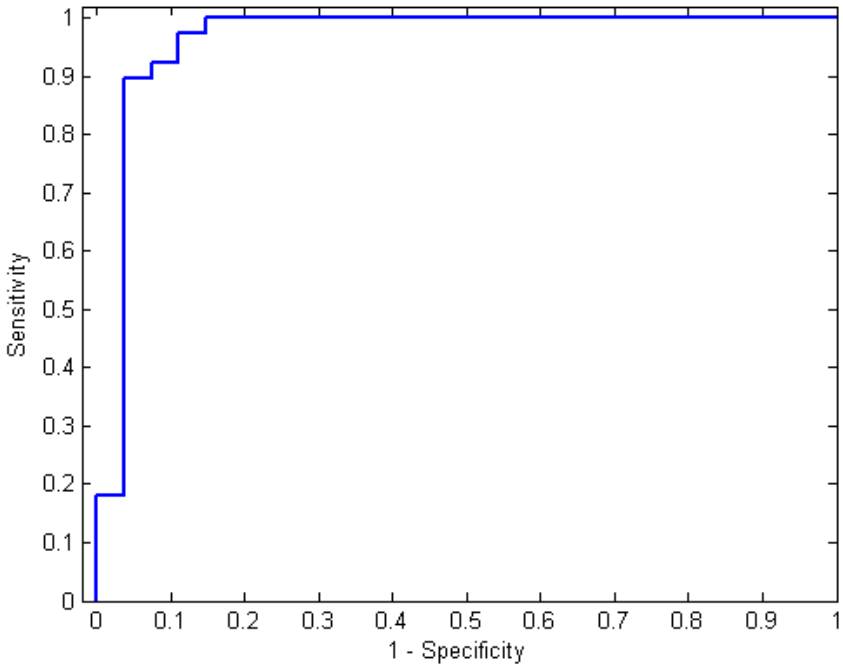

(a)

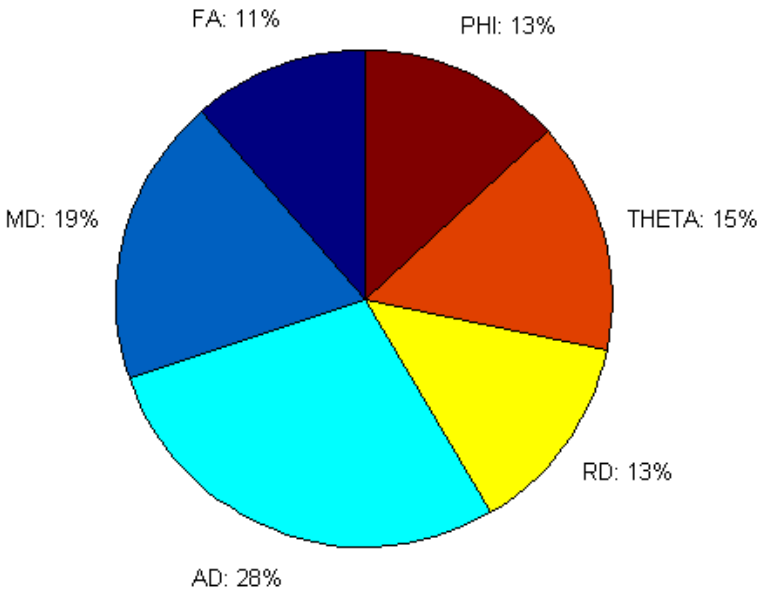

(b)

Figure 6.5: The distribution of classification features based on the DTI-derived measures for the healthy vs. primary open angle glaucoma groups (a) and the ROC curve of the classification with an area under the curve of 0.96 (b)

Table 6.4: Classification performance for the different group pairs evaluated by area under the receiver operating characteristic curve (AUC), classification accuracy (ACC), and sample Sensitivity/Specificity

Groups	#Features	AUC	ACC(%)	Sensitivity/Specificity
Normal vs. G	33	0.968	94.05	92.98/96.30
Normal vs. POAG	53	0.962	92.42	92.31/92.59
Normal vs. NTG	28	1	100	100/100
NTG vs. POAG	52	0.996	98.25	100/94.44

Table 6.5: Unbiased classification performance for the different group pairs evaluated by classification accuracy (ACC), and Sensitivity/Specificity

Groups	ACC(%)	Sensitivity/Specificity
Normal vs. G	84.52	94.74/62.96
Normal vs. POAG	81.82	87.18/74.07
Normal vs. NTG	80	77.78/81.48
NTG vs. POAG	80.70	92.31/61.11

6.4.4 Healthy vs. normal tension glaucoma

The number of features selected as an input to the classifier was 28. However, MD and AD amounted only to 18% of the features while PHI and THETA constituted 50% of the feature set. The achieved accuracy was 100% with all the subjects correctly categorized. This corresponded to a unit step ROC curve (Figure 6.6a) with an unity area and a maximum sensitivity/specificity of 100%/100%. The classification rate based on the unbiased analysis was 80%. This represented a 20% reduction from the aforementioned accuracy. Almost the same reduction ratio was observed in the sensitivity and specificity at 77.78% and 81.48%, respectively.

6.4.5 Primary open angle glaucoma vs. normal tension glaucoma

The final group pair tested the ability of the system to distinguish between subclasses of glaucoma (POAG and NTG). In this case the PDD related measures (THETA and PHI) had only 7 (14%) features among the 52 features that gave the best performance. The AD and FA based features were 29% and 23% of the set, respectively. From the ROC curve in Figure 6.7a, a 100% sensitivity can be observed at a 94.44% specificity while the AUC was 0.996. All POAG subjects were accurately recognized and only one NTG patient was misclassified as POAG subjects resulting in a 98.25% recognition rate. The difference between the two analyses was 17.5% and the adjusted recognition rate was 80.7%. Thirty six POAG patients and 11 NTG patients were correctly associated to their respective groups resulting in a sensitivity of 92.31% and a specificity of 61.11%.

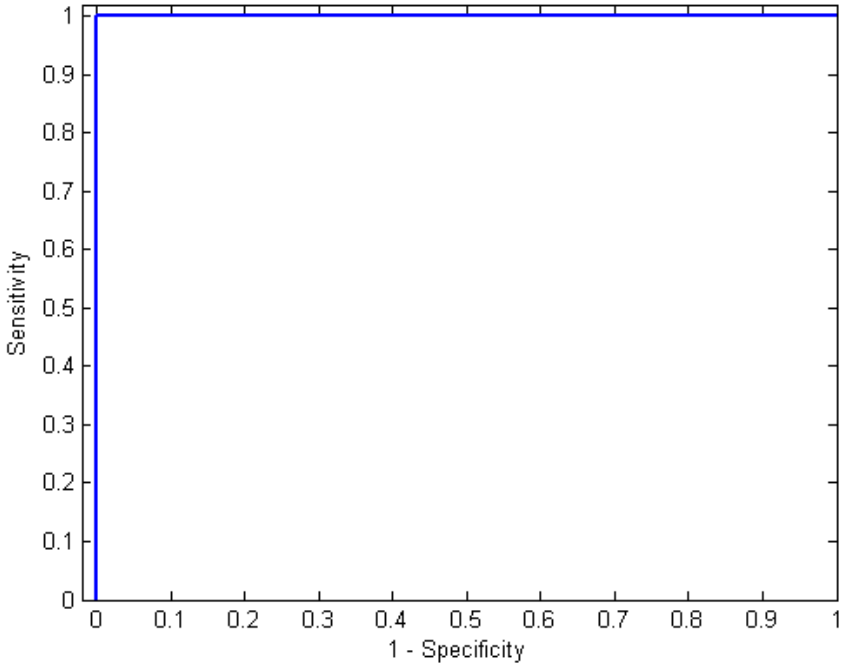

(a)

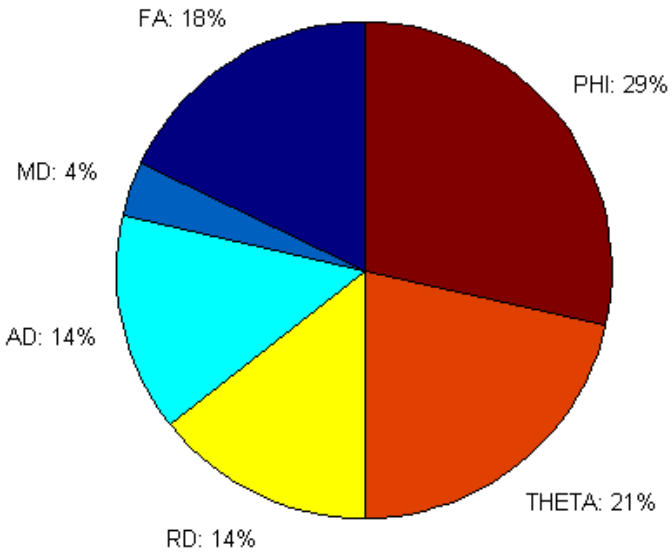

(b)

Figure 6.6: The distribution of classification features based on the DTI-derived measures for the healthy vs. normal tension glaucoma groups (a) and the ROC curve of the classification with an area under the curve of 1.0 (b)

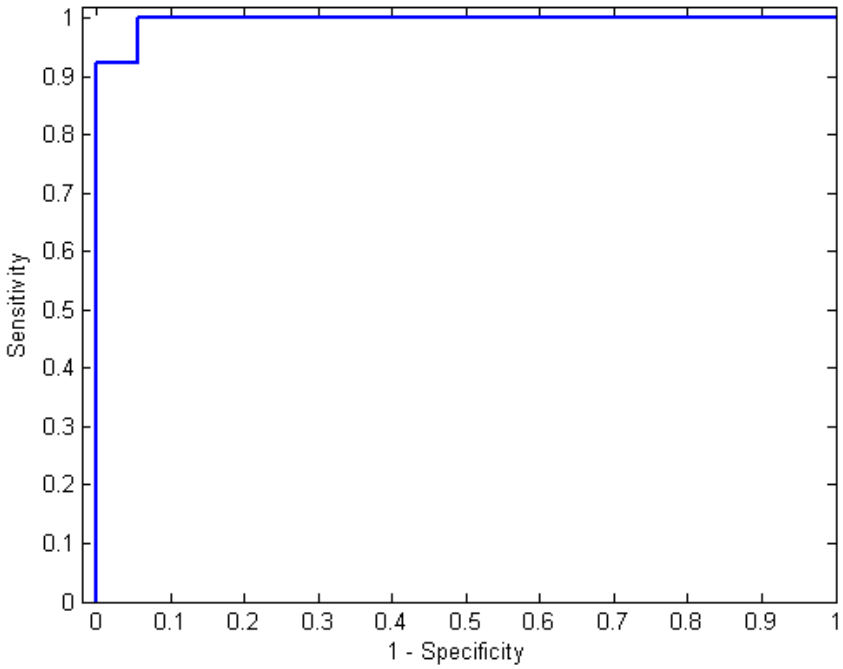

(a)

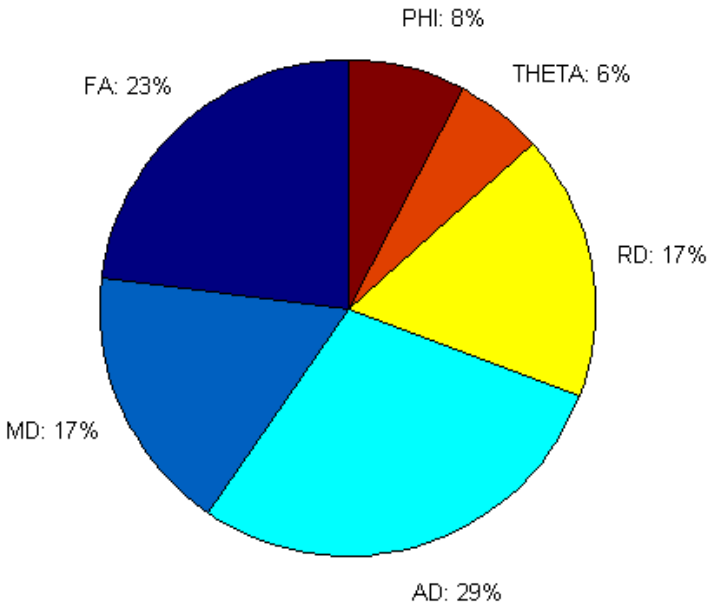

(b)

Figure 6.7: The distribution of classification features based on the DTI-derived measures for the Primary open angle glaucoma vs. normal tension glaucoma groups (a) and the ROC curve of the classification with an area under the curve of 0.996 (b)

6.5 Discussion

A novel direction in glaucoma classification using visual pathway analysis is proposed in this work. The system utilizes DTI to segment the optic radiation as a part of the human visual system and to extract features based on various aspects describing the state of its fiber bundle. The system is applied to four group pairs containing normal and different types of glaucoma. In addition, it identifies the DTI-parameters that have the most significant contribution in obtaining high classification rates for each group pair. Using this new approach, the system achieves very high classification rates for all the groups under consideration.

The automated segmentation algorithm followed by a minor manual post processing minimizes the user interaction and increases the reliability of the ROI selection. The finally processed ROI should represent the core coherent fiber bundle of the optic radiation ensuring the correct correspondence among all subjects and the DTI-problems. As can be seen from the reliability analysis of the ROI configuration, a mean subvoxel agreement measured by the MHD is obtained among two different operators in addition to a mean overlap of approximately 93%. The robust automated segmentation which requires no operator interaction, the developed manipulation GUI, and the devised configuration procedure contribute to this high inter-operator reliability. This is a very critical step to ensure that the extracted features are not operator dependant.

In addition to the three diffusivity parameters (MD, AD, and RD) and the anisotropy measure FA, the two angles of the spherical coordinate system describe the orientation of the fibers are used for feature extraction. These measures can be medically interpreted as they describe fiber aspects. Thus, these six DTI-parameters were included in the performed analysis.

The selection of the first order histogram features is motivated by the sensitivity of the DTI-parameters to Glaucoma [Gara 09, Enge 12a, Enge 12b]. Significant changes in the mean of FA, MD, and RD were demonstrated in glaucoma patients compared to healthy controls. Thus, the histogram statistics were previously examined as features by the author providing competitive glaucoma classification rates [El R 11c] and so they are included in this system as well. The performed voxel based morphometry analysis using DTI in Chapter 5 and the preliminarily results indicated localized fiber abnormalities due to glaucoma in the optic radiation for the DTI-derived measures. This suggests a possible texture difference along the optic radiation bundle and, therefore, second and higher order texture features are utilized. A ranking algorithm was applied to the features to identify the most discriminating features for each glaucoma type.

The relatively small number of samples with respect to the number of features in this study is a common challenge for classification that limits the evaluation of the presented system [Saey 07, Wood 07]. The optimal solution to such a problem is to have sufficient number of subjects to perform feature selection and classifier training on a separate subset that adequately represents the classes. The rest of the data should then be utilized to test the ranked features and to obtain the unbiased recognition rates. However, this is not feasible in many classification cases where the determination of the best performing features and the accuracy need to be computed.

This study faces the same challenge. In order to mitigate this problem, we have utilized two types of analysis. The first method targets mainly the selection of the optimal classification features and their distribution. The features are ordered using cross validation on the whole dataset. Then, a second cross validation on the entire data is used to evaluate the classification based on the selected features. The main drawback of this analysis is that the selection is based on the complete data which might give overrated recognition accuracy. However, it is expected that these rates should relate to the unbiased accuracies. The purpose of the second approach is to provide unbiased evaluation of the classification. This is accomplished by performing the testing on data that are not used for feature ranking and model construction as described in Subsection 6.3.4. Despite providing an unbiased accuracy, this method can not be used for determining a single set of features or the parameters' distribution. This is due to the possibility of having different feature sets in each step. Therefore, both methods are presented in this work to identify the generalized discriminative feature distributions and to estimate accurately the classification rates.

The separation of control subjects from the different entities of glaucoma or in general glaucoma subjects is accomplished with high recognition rates and limited number of features. However, a certain degree of bias is anticipated in the rates. The normal-NTG classes can be identified with 100% accuracy using only 28 features while for normal-POAG the accuracy is 92.4%. The system produces 94.1% recognition accuracy for the normal-glaucoma (POAG+NTG) groups with 33 features. Moreover, the two considered types of glaucoma can be distinguished from each other with 98.3% accuracy. This emphasizes the significance of the visual pathway analysis and the sensitivity of the used DTI-parameters. The set of parameters for a group pair is not necessarily the best for the others. For example, AD and MD represent almost the source of half of the features used in normal-glaucoma and normal-POAG pairs. However, AD and FA features comprises 52% of the features used for POAG-NTG groups. So, the contribution of the DTI-parameters in the feature set is different depending on the groups being classified. Eighty four subjects are included in this analysis. The NTG is the smallest group containing 18 subjects while POAG is the largest group with 39 patients. More subjects are needed to precisely determine the distribution of the most discriminating DTI-indices. Nevertheless, the sensitivity of the parameters to glaucoma and their effectiveness in glaucoma classification can be observed from the system performance.

The selection bias for the healthy vs. glaucoma and POAG groups was calculated to be around of 10% leading to classification accuracies of 84.52% and 81.82%, respectively. The bias was increased in the NTG vs. POAG and NTG vs. control groups to 17.5% and 20%, respectively. The bias increase in the pairs involving the NTG group could be attributed to the relatively small number of samples in this group. Thus, removing 10% of the samples for testing and estimating the features based on the rest could highly affect the generalization of the classifier. This will in turn degrade the performance.

The existence of many eye imaging modalities that are integrated in the clinical flow for eye examinations and disease detection attracted many researchers to develop systems utilizing the data provided by these modalities for glaucoma diagnosis [Mede 04]. Examples are methods based on fundus images [Naya 09, Bock 10],

HRT [Burg 07], and OCT [Mede 04]. Despite the efficiency of these systems, there are still many issues to be addressed and improved. e.g., detecting different types of glaucoma, prognosis and early diagnosis of glaucoma, improving existing systems performance, etc. The trend followed in the proposed system is new as it analyzes the visual pathway in the brain which has not been considered before for glaucoma classification. The high efficiency of the system is evident from the classification results from the system application to different diseased groups. Additionally, it uses a different source of information that could open a new dimension in this field not specifically for glaucoma but for other visual system diseases.

Chapter 7

Summary

Many mechanisms and factors are involved in the formation of glaucoma pathology. The pathophysiology of the different types of the disease is variable. The symptoms of glaucoma are scarce and the vision loss develops gradually. These cause patients' unawareness of the disease until a remarkable change of vision is observed. The neuronal death and the visual impairment associated with the pathology can not be restored. Therefore, early diagnosis is crucial to reduce the high prevalence of glaucoma. The retina contains three out of the four visual pathway neurons (photoreceptors, amacrine and bipolar cells, retinal ganglion cells). Thus, it was the focus of many studies that investigated the correlation between glaucoma and structural abnormalities such as retinal nerve fiber atrophy, retinal vessels and optic disk changes. However, the third neuron (RGCs) connects the retina with the brain while the intracerebral part of the fourth neuron (optic radiation) completely resides in the brain. Furthermore, it has been reported that the glaucomatous degeneration is transneuronal where disorders in various locations in the visual pathway were observed. This suggests that brain imaging techniques can be utilized to increase the understanding of the disease and, consequently, provide additional examinations that may result in improving the diagnosis.

In this dissertation, we aimed to investigate the relevance and the significance of visual system analyses to glaucoma at the cerebral level. The great possibilities offered by the non-invasive DTI-modality allowed performing this research. DTI goes beyond traditional MRI by supplying directional information about the self-diffusion within fibers and, thus, it is used to capture the organization of the white matter pathways. Moreover, parameters have been derived from the diffusion tensor to describe different aspects of the diffusion process. Diffusivity, anisotropy, and coherence measures are among the classes of DTI-derived indices. Some of these parameters are related to the neuronal injury attributed to neurodegenerative diseases. The optic radiation is the main targeted object for processing and analysis using DTI.

An algorithm has been proposed for the automatic segmentation of the optic radiation. This algorithm is an essential element in the introduced systems and the studies conducted in this work. It uses dissimilarity measure between the tensors and relies on the coherence property within the fiber bundle of the optic radiation. The automation eliminates the inconsistencies arising from inter-operator intervention for identifying the optic radiation. In addition, it allows the processing of large num-

ber of subjects. The problem of system initialization is addressed by utilizing prior knowledge about the physiological and anatomical properties of the optic radiation in order to automatically provide a robust estimation of it. The incorporation of the Log-Euclidean framework in the statistical level set framework is suitable and efficient for DTI segmentation because it accounts for the Riemannian nature of the tensor space and incorporates the whole tensor information in a probabilistic framework. The system is implemented and tested using real DTI-data. The experimental results indicate that the system shows high efficiency in determining the main fiber bundle of the optic radiation for normal and glaucoma subjects. Therefore, it is suitable for usage in glaucoma related examinations.

Recent studies showed that the diffusion tensor parameters correlate with glaucoma in the visual pathway. Mean diffusivity and FA are used as indicators of impaired white matter. Decreased FA and increased MD demonstrated fiber degeneration in the glaucomatous optic radiation and optic nerve. We confirmed these results and additionally we investigated the diffusion in a direction transverse to the fiber orientation described by the RD. Neuronal diseases causing demyelination are suggested to lead to an increase in RD as observed in the obtained results. Furthermore, significant correlation was found between the DTI-parameters in the optic radiation and the stage of glaucoma indicated by indices derived from retinal examination. A statistical analysis was performed to cluster the glaucoma patients and to identify the factors affecting the optic radiation such as age. In this study, we observed that the age is a decisive factor to ascertain the glaucomatous disorder in the optic radiation.

A framework is proposed for the localization of the deleterious glaucoma effect on the optic radiation. The system overcomes the complexities of the DTI and allows efficient voxel-based morphometric analysis. The framework is based on intersubject shape similarity of the optic radiation bundle. Thus, it can be applied to any neurological disease that does not influence the shape topology of the fiber bundle under examination. It is independent from the diffusion tensor changes in the visual pathway. The preliminary analysis of the system application provided maps of localized fiber abnormalities in the optic radiation associated with glaucoma. These maps showed the significant regional differences with respect to different DTI-measures.

Visual pathway analysis using DTI is recently introduced to glaucoma by analyzing the white matter fibers of the visual system. The proposed system is the first to classify the disease using optic radiation analysis. In contrast to the common diagnostic systems based on eye imaging modalities, the proposed visual pathway based system presents a novel classification perspective. The system achieved high recognition rates not only for discriminating healthy subjects from different types of patients but also for differentiating entities of the disease. Moreover, it is competitive to many of the state of the art retina-based detection algorithms in terms of the recognition rates. In agreement with previous studies, this analysis emphasizes the sensitivity of the DTI-derived parameters to glaucoma. Moreover, it identified the most significant DTI-measures for the considered forms of the pathology.

In conclusion, the proposed algorithms, systems, and studies can lead to the advance of the glaucoma research and therapy. The suggested novel techniques to process DTI-data assist in the understanding of neuro-ophthalmologic diseases. The

results from the presented medical studies add more evidence to the extension of the glaucoma insult to the visual pathway. Thus, they emphasize the importance and potential of this direction. DTI is a valuable tool for the identification of white matter fibers as well as the characterization and localization of pathologic abnormalities. This suggests that integrating DTI-based visual pathway analysis to the glaucoma examination flow can give more insight into the disease and in turn enhance the diagnosis and treatment.

Chapter 8

Outlook

The analysis of the visual pathway conducted in this work has the optic radiation as its main focus. The optic radiation has a complex fiber structure that follows a complicated course. In addition, the limited spatial resolution of the DTI modality and the limitations of the diffusion tensor in modeling complex fiber situations such as crossing and branching of fibers contribute to inaccuracies in identifying the optic radiation. These inaccuracies lead to difficulties in distinguishing the optic radiation from other intersecting bundles and to the inability to resolve the branching segments to the visual cortex. Moreover, it results in mismeasurements of the degree of anisotropy and diffusivities at locations with IVOH. Therefore, the analysis is confined to the main coherent fiber bundle of the optic radiation. However, the segmentation of the optic radiation connections to the visual cortex should be examined. This requires the development of a robust tractography algorithm in order to capture the highly variable branches of the optic radiation while taking into consideration the complex fiber situations (e.g. crossing, branching, etc...) and the uncertainties in the diffusion tensor data.

The developed voxel based morphometry framework was applied to a limited number of subjects. A large population study where different glaucoma entities and factors can be examined and differentiated should be considered. This will increase the reliability of the voxelwise statistical analysis and the confidence in the localization maps. Such studies are expected to resolve the discriminating factors for each glaucoma entity and to aid in explaining the pathology mechanism. Following the introduced shape similarity concept, volumetric shape modeling of the optic radiation can be incorporated to perform three-dimensional analysis.

Glaucoma is a complicated systemic disease. Therefore, analyses covering the entire visual system can contribute in enhancing the screening and diagnosis of glaucoma. This can be achieved, considering the advances in neuroimaging and retina imaging, by complementing the data from various parts of the visual system. For example, the non-myelinated axons comprising the RNFL using OCT, vessel trees from fundus imaging, optic disc topography described by HRT, and myelinated axons along the visual pathway from the optic nerve to the optic radiation and visual cortex by DTI. Gathering this information together can provide a comprehensive characterization of the visual system. Thus, it can facilitate the understanding of the pathophysiology of glaucoma. New treatment approaches may be developed which

target the neuroprotection of the visual pathway. This may prevent the spread of the disease. The effectiveness of these therapies may be evaluated in longitudinal studies using the proposed morphometry framework. The utilization of the framework in treatment follow up within a group of patients will demonstrate not only the global effect but also the regional changes in the white matter architecture.

The parts of the visual pathway not considered in this thesis, such as the optic nerve and the optic chiasm, require higher spatial resolutions in order to accurately depict their structure. Algorithms to reconstruct the whole visual pathway should be able to resolve voxels with directional heterogeneity. The drawbacks of the diffusion tensor model discussed in Section 3.4 constrain the validity of the parcellation at such locations. This may lead to disconnection of tracts due to the inability to determine the correct fiber orientation. Models capable of discriminating intravoxel fiber populations having different orientations exist in the literature (Section 3.4). Due to their long scanning duration, these models are currently utilized mainly for research purposes. This is due to the fact that significantly large numbers of measuring gradients need to be applied to adequately sample the diffusion process. The range of 32-64 gradients directions is typical for calculating these models. Nevertheless, algorithms based on them can track the fibers in a more plausible manner through IVOH. Moreover, they provide the information that describes diverging or crossing fibers. Their incorporation in the presented analyses is anticipated to produce more precise construction of the visual system structures. Consequently, this will enable performing global analysis of the entire visual pathway.

List of Figures

List of Tables

List of Abbreviations

ACG	Angle Closure Glaucoma
AD	Axial Diffusivity
aFMT	advanced Fast Marching Tractography
ASM	Angular Second Moment
AUC	Area Under the ROC Curve
CI	Coherence Index
DTI	Diffusion Tensor Imaging
DWI	Diffusion Weighted Imaging
EPI	Echo Planar Imaging
FA	Fractional Anisotropy
FDT	Frequency Doubling Technology
FFD	Free-Form Deformation
FMT	Fast Marching Tractography
FoV	Field of View
GLCM	Gray-Level Co-occurrence Matrix
GPS	Glaucoma Probability Score
GRI	Glaucoma Risk Index
GUI	Graphical User Interface
HRT	Heidelberg Retina Tomograph
IOP	IntraOcular blood Pressure
IVOH	IntraVoxel Orientational Heterogeneity
LGN	Lateral Geniculate Nucleus
LI	Lattice Index
MD	Mean Diffusivity
MHD	Modified Hausdorff Distance
MPRAGE	Magnetization Prepared Rapid Gradient Echo
MRA	Moorfields Regression Analysis
MRI	Magnetic Resonance Imaging
NTG	Normal Tension Glaucoma
OAG	Open Angle Glaucoma
OCT	Optical Coherence Tomography
ONH	Optic Nerve Head
PCA	Principal Component Analysis
PDD	Principal Diffusion Direction
PGSE	Pulsed-Gradient Spin-Echo
POAG	Primary Open Angle Glaucoma
RA	Relative Anisotropy

RAVE	RAndom VEctor
RD	Radial Diffusivity
RF	Radio Frequency
RGCs	Retinal Ganglion Cells
ROC	Receiver Operating Characteristic
ROI	Region Of Interest
SD	Standard Deviation
SPM	Statistical Parametric Mapping
SSD	Sum of Squared Differences
SVD	Singular Value Decomposition
SVM	Support Vector Machine
TE	Echo Time
TEND	TENsor Deflection
TR	Repetition Time
VR	Volume Ratio

Bibliography

[Alex 01] A. L. Alexander, K. M. Hasan, M. Lazar, J. S. Tsuruda, and D. L. Parker. "Analysis of partial volume effects in diffusion-tensor MRI". *Magnetic Resonance in Medicine*, Vol. 45, No. 5, pp. 770–780, 2001.

[Alwa 98] W. L. Alward. "Medical management of glaucoma". *New England Journal of Medicine*, Vol. 339, No. 18, pp. 1298–1307, 1998.

[Arde 07] S. Ardekani, A. Kumar, G. Bartzokis, and U. Sinha. "Exploratory voxel-based analysis of diffusion indices and hemispheric asymmetry in normal aging". *Magnetic Resonance Imaging*, Vol. 25, No. 2, pp. 154–167, 2007.

[Arsi 06] V. Arsigny, P. Fillard, X. Pennec, and N. Ayache. "Log-Euclidean metrics for fast and simple calculus on diffusion tensors". *Magnetic Resonance in Medicine*, Vol. 56, No. 2, pp. 411–421, 2006.

[Bala 10] M. Balafar, A. Ramli, M. Saripan, and S. Mashohor. "Review of brain MRI image segmentation methods". *Artificial Intelligence Review*, Vol. 33, pp. 261–274, 2010.

[Bamm 03] R. Bammer, B. Acar, and M. E. Moseley. "In vivo MR tractography using diffusion imaging". *European Journal of Radiology*, Vol. 45, No. 3, pp. 223–234, 2003.

[Bamm 99] R. Bammer, R. Stollberger, M. Augustin, J. Simbrunner, H. Offenbacher, H. Kooijman, S. Ropele, P. Kapeller, P. Wach, F. Ebner, and F. Fazekas. "Diffusion-weighted imaging with navigated interleaved echo-planar imaging and a conventional gradient system". *Radiology*, Vol. 211, No. 3, pp. 799–806, 1999.

[Bass 00] P. J. Basser, S. Pajevic, C. Pierpaoli, J. Duda, and A. Aldroubi. "In vivo fiber tractography using DT-MRI data". *Magnetic Resonance in Medicine*, Vol. 44, No. 4, pp. 625–632, 2000.

[Bass 02] P. Basser and D. Jones. "Diffusion-tensor MRI: theory, experimental design and data analysis - a technical review". *NMR Biomed*, Vol. 15, No. 7-8, pp. 456–467, 2002.

[Bass 94] P. Basser, J. Mattiello, and D. Lebihan. "MR diffusion tensor spectroscopy and imaging". *IOVS*, Vol. 66, No. 1, pp. 259–267, 1994.

[Bass 95] P. J. Basser. "Inferring microstructural features and the physiological state of tissues from diffusion-weighted images". *NMR Biomed*, Vol. 8, No. 7-8, pp. 333–344, 1995.

[Bass 96] P. Basser and C. Pierpaoli. "Microstructural and physiological features of tissues elucidated by quantitative-diffusion-tensor MRI". *Journal of Magnetic Resonance, Series B*, Vol. 111, No. 3, pp. 209–219, 1996.

[Beau 02] C. Beaulieu. "The basis of anisotropic water diffusion in the nervous system - a technical review". *NMR in Biomedicine*, Vol. 15, No. 7-8, pp. 435–455, 2002.

[Behr 03] T. Behrens, M. Woolrich, M. Jenkinson, H. Johansen-Berg, R. Nunes, S. Clare, P. Matthews, J. Brady, and S. Smith. "Characterization and propagation of uncertainty in diffusion-weighted MR imaging". *Magnetic Resonance in Medicine*, Vol. 50, No. 5, pp. 1077–1088, 2003.

[Berg 05] O. Bergmann, A. Lundervold, and T. Steihaug. "Generating a synthetic diffusion tensor dataset". In: *Computer-Based Medical Systems, 2005. Proceedings. 18th IEEE Symposium on*, pp. 277–281, 2005.

[Bock 10] R. Bock, J. Meier, L. Nyúl, J. Hornegger, and G. Michelson. "Glaucoma risk index: automated glaucoma detection from color fundus images". *Medical Image Analysis*, Vol. 14, No. 3, pp. 471–481, 2010.

[Bowd 01] C. Bowd, L. M. Zangwill, C. C. Berry, E. Z. Blumenthal, C. Vasile, C. Sanchez-Galeana, C. F. Bosworth, P. A. Sample, and R. N. Weinreb. "Detecting early glaucoma by assessment of retinal nerve fiber layer thickness and visual function". *Investigative Ophthalmology & Visual Science*, Vol. 42, No. 9, pp. 1993–2003, 2001.

[Bozk 07] U. Bozkaya and B. Acar. "SMT: split and merge tractography for DT-MRI". In: *MICCAI, Brisbane, Australia. Lecture Notes in Computer Science*, pp. 153–160, Springer, 2007.

[Buda 11] A. Budai, J. Odstrcilik, R. Kolar, J. Hornegger, J. Jan, T. Kubena, and G. Michelson. "A public database for the evaluation of fundus image segmentation algorithms". *IOVS*, Vol. 52, ARVO E-Abstract 1345, 2011.

[Burg 05] Z. Burgansky-Eliash, G. Wollstein, T. Chu, J. D. Ramsey, C. Glymour, R. J. Noecker, H. Ishikawa, and J. S. Schuman. "Optical coherence tomography machine learning classifiers for glaucoma detection: a preliminary study". *Investigative Ophthalmology & Visual Science*, Vol. 46, No. 11, pp. 4147–4152, 2005.

[Burg 07] Z. Burgansky-Eliash, G. Wollstein, R. Bilonick, H. Ishikawa, L. Kagemann, and J. Schuman. "Glaucoma detection with the Heidelberg retina tomograph 3". *Ophthalmology*, Vol. 114, No. 3, pp. 466–471, 2007.

[Butl 93] S. Butler. "Functional neuroanatomy". In: *G. Morgan and S. Butler, Editors. Seminars in Basic Neurosciences*, pp. 1–41, London, Gaskell, 1993.

[Cabe 11] M. Cabezas, A. Oliver, X. Lladó, J. Freixenet, and M. B. Cuadra. "A review of atlas-based segmentation for magnetic resonance brain images". *Computer Methods and Programs in Biomedicine*, Vol. 104, No. 3, pp. e158 – e177, 2011.

[Cart 04] F. W. Cartes-Zumelzu, I. Stavrou, M. Castillo, E. Eisenhuber, E. Knosp, and M. M. Thurnher. "Diffusion-weighted imaging in the assessment of brain abscesses therapy". *American Journal of Neuroradiology*, Vol. 25, No. 8, pp. 1310–1317, 2004.

[Cell 00] K. E. Cello, J. M. Nelson-Quigg, and C. A. Johnson. "Frequency doubling technology perimetry for detection of glaucomatous visual field loss". *American Journal of Ophthalmology*, Vol. 129, No. 3, pp. 314–322, 2000.

[Chen 09] T. Chen, C. Lin, Y. Chen, H. Liu, M. Hua, Y. Huang, and M. Chiu. "Diffusion tensor changes in patients with amnesic mild cognitive impairment and various dementias". *Psychiatry Research: Neuroimaging*, Vol. 173, No. 1, pp. 15–21, 2009.

[Cicc 05] O. Ciccarelli, A. Toosy, S. Hickman, G. Parker, C. Wheeler-Kingshott, D. Miller, and A. Thompson. "Optic radiation changes after optic neuritis detected by tractography-based group mapping". *Human Brain Mapping*, Vol. 25, No. 3, pp. 308–316, 2005.

[Clos 09] T. G. Close, J.-D. Tournier, F. Calamante, L. A. Johnston, I. Mareels, and A. Connelly. "A software tool to generate simulated white matter structures for the assessment of fibre-tracking algorithms". *NeuroImage*, Vol. 47, No. 4, pp. 1288–1300, 2009.

[Cole 08] A. L. Coleman and S. Miglior. "Risk factors for glaucoma onset and progression". *Survey of Ophthalmology*, Vol. 53, No. 6, Supplement, pp. S3–S10, 2008.

[Cong 92] N. Congdon, F. Wang, and J. M. Tielsch. "Issues in the epidemiology and population-based screening of primary angle-closure glaucoma". *Survey of Ophthalmology*, Vol. 36, No. 6, pp. 411–423, 1992.

[Cont 99] T. E. Conturo, N. F. Lori, T. S. Cull, E. Akbudak, A. Z. Snyder, J. S. Shimony, R. C. Mckinstry, H. Burton, and M. E. Raichle. "Tracking neuronal fiber pathways in the living human brain". *Proc Natl Acad Sci U S A*, Vol. 96, No. 18, pp. 10422–10427, 1999.

[Coro 06] I. Corouge, P. Fletcher, S. Joshi, S. Gouttard, and G. Gerig. "Fiber tract-oriented statistics for quantitative diffusion tensor MRI analysis". *Medical Image Analysis*, Vol. 10, No. 5, pp. 786–798, 2006.

[Ding 03] Z. Ding, J. C. Gore, and A. W. Anderson. "Classification and quantification of neuronal fiber pathways using diffusion tensor MRI". *Magnetic Resonance in Medicine*, Vol. 49, No. 4, pp. 716–721, 2003.

[Dolc 02] F. Dolcos, H. Rice, and R. Cabeza. "Hemispheric asymmetry and aging: right hemisphere decline or asymmetry reduction". *Neuroscience & Biobehavioral Reviews*, Vol. 26, No. 7, pp. 819–825, 2002.

[Dong 04] Q. Dong, R. C. Welsh, T. L. Chenevert, R. C. Carlos, P. Maly-Sundgren, D. M. Gomez-Hassan, and S. K. Mukherji. "Clinical applications of diffusion tensor imaging". *Journal of Magnetic Resonance Imaging*, Vol. 19, pp. 6–18, 2004.

[Down 11] J. C. Downs, M. D. Roberts, and I. A. Sigal. "Glaucomatous cupping of the lamina cribrosa: a review of the evidence for active progressive remodeling as a mechanism". *Experimental Eye Research*, Vol. 93, No. 2, pp. 133–140, 2011.

[Dran 01] S. Drance, D. R. Anderson, and M. Schulzer. "Risk factors for progression of visual field abnormalities in normal-tension glaucoma". *American Journal of Ophthalmology*, Vol. 131, No. 6, pp. 699–708, 2001.

[Dubu 94] M. Dubuisson and A. Jain. "A modified Hausdorff distance for object matching". In: *Proceedings of the 12th IAPR International Conference on Pattern Recognition, Conference A: Computer Vision & Image Processing*, pp. 566–568, 1994.

[Eins 05] A. Einstein. "Über die von der molekularkinetischen Theorie der Wärme geforderte Bewegung von in ruhenden Flüssigkeiten suspendierten Teilchen". *Annalen der Physik*, Vol. 17, pp. 549–560, 1905.

[El R 09] A. El-Rafei, J. Hornegger, T. Engelhorn, A. Dörfler, S. Wärntges, and G. Michelson. "Automatic segmentation of the optic radiation using DTI in glaucoma patients". In: *Computational Vision and Medical Image Processing - VipIMAGE 2009. International Conference VipIMAGE 2009 - II ECCOMAS Thematic Conference on Computational Vision and Medical Image Processing, Portugal*, pp. 293–298, Taylor and Francis, 2009.

[El R 11a] A. El-Rafei, T. Engelhorn, S. Waerntges, A. Doerfler, J. Hornegger, and G. Michelson. "Automatic segmentation of the optic radiation using DTI in healthy subjects and patients with glaucoma". In: *Tavares JMRS, Jorge RMN, editors. Computational Vision and Medical Image Processing, Computational Methods in Applied Sciences*, pp. 1–15, Springer, 2011.

[El R 11b] A. El-Rafei, T. Engelhorn, S. Waerntges, A. Doerfler, J. Hornegger, and G. Michelson. "A framework for voxel-based morphometric analysis of the optic radiation using diffusion tensor imaging in glaucoma". *Magnetic Resonance Imaging*, Vol. 29, No. 8, pp. 1076–1087, 2011.

[El R 11c] A. El-Rafei, T. Engelhorn, S. Waerntges, A. Doerfler, J. Hornegger, and G. Michelson. "Glaucoma classification based on histogram analysis of diffusion tensor imaging measures in the optic radiation". In: *Real P,Diaz-Pernil D, Molina-Abril H, Berciano A, Kropatsch W, editors. Computer Analysis of Images and Patterns, Lecture Notes in Computer Science*, pp. 529–536, Berlin: Springer, 2011.

[Enge 11] T. Engelhorn, G. Michelson, S. Waerntges, T. Struffert, S. Haider, and A. Doerfler. "Diffusion tensor imaging detects rarefaction of optic radiation in glaucoma patients". *Academic Radiology*, Vol. 18, No. 6, pp. 764–769, 2011.

[Enge 12a] T. Engelhorn, G. Michelson, S. Wärntges, S. Hempel, A. El-Rafei, T. Struffert, and A. Doerfler. "A new approach to assess intracranial white matter abnormalities in glaucoma patients: changes of fractional anisotropy detected by 3T diffusion tensor imaging". *Academic Radiology*, Vol. 19, No. 4, pp. 485–488, 2012.

[Enge 12b] T. Engelhorn, G. Michelson, S. Wärntges, M. Otto, A. El-Rafei, T. Struffert, and A. Doerfler. "Changes of radial diffusivity and fractional anisotropy in the optic nerve and optic radiation of glaucoma patients". *The Scientific World Journal*, Vol. 2012, Article ID 849632, 5 pages, 2012.

[Fech 94] R. Fechtner and R. Weinreb. "Mechanisms of optic nerve damage in primary open angle glaucoma". *Surv Ophthalmol*, Vol. 39, No. 1, pp. 23–42, 1994.

[Ferr 08] A. Ferreras, L. Pablo, J. Larrosa, V. Polo, A. B. Pajarín, and F. M. Honrubia. "Discriminating between normal and glaucoma-damaged eyes with the Heidelberg retina tomograph 3". *Ophthalmology*, Vol. 115, No. 5, pp. 775–781.e2, 2008.

[Flet 07] P. T. Fletcher and S. C. Joshi. "Riemannian geometry for the statistical analysis of diffusion tensor data". *Signal Processing*, Vol. 87, No. 2, pp. 250–262, 2007.

[Fost 02] P. J. Foster, R. Buhrmann, H. A. Quigley, and G. J. Johnson. "The definition and classification of glaucoma in prevalence surveys". *British Journal of Ophthalmology*, Vol. 86, No. 2, pp. 238–242, 2002.

[Gara 09] F. Garaci, F. Bolacchi, A. Cerulli, M. Melis, A. Spanó, C. Cedrone, R. Floris, G. Simonetti, and C. Nucci. "Optic nerve and optic radiation neurodegeneration in patients with glaucoma: in vivo analysis with 3-T diffusion-tensor MR imaging". *Radiology*, Vol. 252, No. 2, pp. 496–501, 2009.

[Goeb 03] R. Goebel, L. Muckli, and D. Kim. "The visual system". In: *G. Paxinos and J.K. Mai Editors, The Human Nervous System, 2nd Edition*, pp. 1280–1305, New York: Academic Press, 2003.

[Gupt 06] N. Gupta, L. Ang, L. de Tilly, L. Bidaisee, and Y. Yücel. "Human glaucoma and neural degeneration in intracranial optic nerve, lateral geniculate nucleus, and visual cortex". *British Journal of Ophthalmology*, Vol. 90, No. 6, pp. 674–678, 2006.

[Gupt 07] N. Gupta and Y. Yücel. "What changes can we expect in the brain of glaucoma patients?". *Survey of Ophthalmology*, Vol. 52, No. 6, Supplement 1, pp. S122–S126, 2007.

[Guyo 02] I. Guyon, J. Weston, S. Barnhill, and V. Vapnik. "Gene selection for cancer classification using support vector machines". *Machine Learning*, Vol. 46, No. 1-3, pp. 389–422, 2002.

[Hall 09] M. Hall, E. Frank, G. Holmes, B. Pfahringer, P. Reutemann, and I. Witten. "The WEKA data mining software: an update". *SIGKDD Explorations*, Vol. 11, No. 1, pp. 10–18, 2009.

[Hama 06] G. Hamarneh and J. Hradsky. "DTMRI segmentation using DT-snakes and DT-livewire". In: *IEEE International Symposium on Signal Processing and Information Technology*, pp. 513–518, 2006.

[Hami 08] L. Hamilton, J. Levitt, J. O'Neill, J. Alger, E. Luders, O. Phillips, R. Caplan, A. Toga, J. McCracken, and K. Narr. "Reduced white matter integrity in attention-deficit hyperactivity disorder". *Neuroreport*, Vol. 19, No. 17, pp. 1705–1708, 2008.

[Hara 73] R. Haralick, K. Shanmugam, and I. Dinstein. "Textural features for image classification". *IEEE Transactions on Systems, Man and Cybernetics*, Vol. 3, No. 6, pp. 610–621, 1973.

[Heij 02] A. Heijl, M. C. Leske, B. Bengtsson, L. Hyman, B. Bengtsson, and M. Hussein. "Reduction of intraocular pressure and glaucoma progression: results from the early manifest glaucoma trial". *Arch Ophthalmol*, Vol. 120, No. 10, pp. 1268–1279, 2002.

[Henr 03] R. Henry, J. Oh, S. Nelson, and D. Pelletier. "Directional diffusion in relapsing-remitting multiple sclerosis: a possible in vivo signature of Wallerian degeneration". *Journal of Magnetic Resonance Imaging*, Vol. 18, No. 4, pp. 420–426, 2003.

[Hern 11] A. Hernowo, C. Boucard, N. Jansonius, J. Hooymans, and F. Cornelissen. "Automated morphometry of the visual pathway in primary open-angle glaucoma". *IOVS*, Vol. 52, No. 5, pp. 2758–2766, 2011.

[Hofe 10] S. Hofer, A. Karaus, and J. Frahm. "Reconstruction and dissection of the entire human visual pathway using diffusion tensor MRI". *Frontiers in Neuroanatomy*, Vol. 13, pp. 4–15, 2010.

[Hood 07] D. C. Hood and R. H. Kardon. "A framework for comparing structural and functional measures of glaucomatous damage". *Prog Retin Eye Res*, Vol. 26, No. 6, pp. 688–710, 2007.

[Hors 02] M. Horsfield and D. Jones. "Applications of diffusion-weighted and diffusion tensor MRI to white matter diseases - a review". *NMR in Biomedicine*, Vol. 15, No. 7-8, pp. 570–577, 2002.

[Huan 07] J. Huang, R. Friedland, and A. Auchus. "Diffusion tensor imaging of normal-appearing white matter in mild cognitive impairment and early alzheimer disease: preliminary evidence of axonal degeneration in the temporal lobe". *American Journal of Neuroradiology*, Vol. 28, No. 10, pp. 1943–1948, 2007.

[Hui 07] E. Hui, Q. Fu, K. So, and E. Wu. "Diffusion tensor MR study of optic nerve degeneration in glaucoma". In: *Proceedings of the 29th Annual International Conference of the IEEE Engineering in Medicine and Biology Society (EMBS)*, pp. 4312–4315, 2007.

[Hupp 01] P. S. Huppi, B. Murphy, S. E. Maier, G. P. Zientara, T. E. Inder, P. D. Barnes, R. Kikinis, F. A. Jolesz, and J. J. Volpe. "Microstructural brain development after perinatal cerebral white matter injury assessed by diffusion tensor magnetic resonance imaging". *Pediatrics*, Vol. 107, No. 3, pp. 455–460, 2001.

[Jage 05] H. R. Jäger. "Loss of vision: imaging the visual pathways". *European Radiology*, Vol. 15, pp. 501–510, 2005.

[John 06] J. John, L. Wang, A. Moffitt, H. Singh, M. Gado, and J. Csernansky. "Inter-rater reliability of manual segmentation of the superior, inferior and middle frontal gyri". *Psychiatry Research: Neuroimaging*, Vol. 148, No. 2-3, pp. 151–163, 2006.

[Jona 03] J. B. Jonas, E. Berenshtein, and L. Holbach. "Anatomic relationship between lamina cribrosa, intraocular space, and cerebrospinal fluid space". *Investigative Ophthalmology & Visual Science*, Vol. 44, No. 12, pp. 5189–5195, 2003.

[Jone 05] D. Jones, M. Symms, M. Cercignani, and R. Howard. "The effect of filter size on VBM analyses of DT-MRI data". *NeuroImage*, Vol. 26, No. 2, pp. 546–554, 2005.

[Jone 08] D. Jones. "Tractography gone wild: probabilistic fibre tracking using the wild bootstrap with diffusion tensor MRI". *IEEE Transactions on Medical Imaging*, Vol. 27, No. 9, pp. 1268–1274, 2008.

[Klin 99] T. Klingberg, C. J. Vaidya, J. D. E. Gabrieli, M. E. Moseley, and M. Hedehus. "Myelination and organization of the frontal white matter in children: a diffusion tensor MRI study". *NeuroReport*, Vol. 10, pp. 2817–2821, 1999.

[Kroe 03] M. Kroese and H. Burton. "Primary open angle glaucoma. The need for a consensus case definition". *Journal of Epidemiology and Community Health*, Vol. 57, No. 9, pp. 752–754, 2003.

[Kueh 03] W. Kuehnel, Ed. *Color atlas of cytology, histology, and microscopic anatomy, 4th Edition*. Thieme Verlag, 2003.

[Kueh 05] M. Kuehn, J. Fingert, and Y. Kwon. "Retinal ganglion cell death in glaucoma: mechanisms and neuroprotective strategies". *Ophthalmol Clin North Am*, Vol. 18, pp. 383–395, 2005.

[Kwon 09] Y. H. Kwon, J. H. Fingert, M. H. Kuehn, and W. L. Alward. "Primary open-angle glaucoma". *New England Journal of Medicine*, Vol. 360, No. 11, pp. 1113–1124, 2009.

[Lans 00] M. G. Lansberg, A. M. Norbash, M. P. Marks, D. C. Tong, M. E. Moseley, and G. W. Albers. "Advantages of adding diffusion-weighted magnetic resonance imaging to conventional magnetic resonance imaging for evaluating acute stroke". *Arch Neurol*, Vol. 57, No. 9, pp. 1311–1316, 2000.

[Laws 80] K. Laws. *Textural features for image classification*. PhD thesis, Electrical Engineering, University of Southern California, 1980.

[Laza 02] M. Lazar and A. Alexander. "White matter tractography using random vector (RAVE) perturbation". In: *Proceedings of 10th ISMRM Annual Meeting*, p. 539, 2002.

[Laza 03] M. Lazar, D. M. Weinstein, J. S. Tsuruda, K. M. Hasan, K. Arfanakis, M. E. Meyerand, B. Badie, H. A. Rowley, V. Haughton, A. Field, and A. L. Alexander. "White matter tractography using diffusion tensor deflection". *Hum Brain Mapp*, Vol. 18, No. 4, pp. 306–321, 2003.

[Laza 05] M. Lazar and A. L. Alexander. "Bootstrap white matter tractography (BOOT-TRAC)". *NeuroImage*, Vol. 24, No. 2, pp. 524–532, 2005.

[Le B 01] D. Le Bihan, J. Mangin, C. Poupon, C. Clark, S. Pappata, N. Molko, and H. Chabriat. "Diffusion tensor imaging: concepts and applications". *The Anatomical Record*, Vol. 13, No. 4, pp. 534–546, 2001.

[Lee 10] B. B. Lee, P. R. Martin, and U. GrÃijnert. "Retinal connectivity and primate vision". *Progress in Retinal and Eye Research*, Vol. 29, No. 6, pp. 622 – 639, 2010.

[Leem 03] A. Leemans, J. Sijbers, M. Verhoye, A. V. D. Linden, and D. V. Dyck. "A simulated phantom for diffusion tensor MRI fiber tracking". In: *Proceedings of Advanced Concepts for Intelligent Vision Systems (ACIVS), Belgium*, pp. 281–285, 2003.

[Leem 09] A. Leemans, B. Jeurissen, J. Sijbers, and D. Jones. "ExploreDTI: a graphical toolbox for processing, analyzing, and visualizing diffusion MR data". In: *17th Annual Meeting of Intl Soc Mag Reson Med, Hawaii, USA*, p. 3537, 2009.

[Leng 06] C. Lenglet, M. Rousson, and R. Deriche. "DTI segmentation by statistical surface evolution". *IEEE Transactions on Medical Imaging*, Vol. 25, No. 6, pp. 685–700, 2006.

[Lian 00] Z. Liang and P. Lauterbur, Eds. *Principles of magnetic resonance imaging: a signal processing perspective*. IEEE Press New York, 2000.

[Liu 04] C. Liu, R. Bammer, B. Acar, and M. E. Moseley. "Characterizing non-gaussian diffusion by using generalized diffusion tensors". *Magnetic Resonance in Medicine*, Vol. 51, No. 5, pp. 924–937, 2004.

[Lu 08] A. T.-H. Lu, M. Wang, R. Varma, J. S. Schuman, D. S. Greenfield, S. D. Smith, and D. Huang. "Combining nerve fiber layer parameters to optimize glaucoma diagnosis with optical coherence tomography". *Ophthalmology*, Vol. 115, No. 8, pp. 1352–1357, 2008.

[Mart 08] F. Martini and J. Nath, Eds. *Fundamentals of anatomy and physiology, 8th Edition*. Benjamin Cummings, 2008.

[McCa 82] C. McCaa. "The eye and visual nervous system: anatomy, physiology and toxicology". *Environmental Health Perspectives*, Vol. 44, pp. 1–8, 1982.

[Mede 04] F. Medeiros, L. Zangwill, C. Bowd, and R. Weinreb. "Comparison of the GDx VCC scanning laser polarimeter, HRT II confocal scanning laser ophthalmoscope, and Stratus OCT optical coherence tomograph for the detection of glaucoma". *Arch Ophthalmol*, Vol. 122, No. 6, pp. 827–837, 2004.

[Mich 12a] G. Michelson, T. Engelhorn, S. Wärntges, A. El-Rafei, J. Hornegger, and A. Doerfler. "DTI-parameters of axonal integrity and demyelination of the optic radiation correlate with glaucoma indices". *Accepted in Graefe's Archive for Clinical and Experimental Ophthalmology*, 2012.

[Mich 12b] G. Michelson, T. Engelhorn, S. Wärntges, A. El-Rafei, J. Hornegger, and A. Doerfler. "Integrität/Demyelinisierung der Radiatio Optica, Morphologie der Papille und Kontrastsensitivität bei Glaukompatienten". *Accepted in Klinische Monatsblätter für Augenheilkunde*, 2012.

[Mich 12c] G. Michelson, S. Wärntges, T. Engelhorn, A. El-Rafei, J. Hornegger, and A. Doerfler. "Cluster analysis of glaucoma patients using the retinal nerve fiber layer thickness of the optic nerve and DTI parameters of the optic radiation". *J Clinic Experiment Ophthalmol 2011, S4:001*, 2012.

[Mobe 05] B. Moberts, A. Vilanova, and J. van Wijk. "Evaluation of fiber clustering methods for diffusion tensor imaging". In: *Visualization, 2005. VIS 05. IEEE*, pp. 65–72, 2005.

[Mori 02] S. Mori and P. C. M. van Zijl. "Fiber tracking: principles and strategies - a technical review". *NMR in Biomedicine*, Vol. 15, No. 7-8, pp. 468–480, 2002.

[Mori 08] S. Mori, K. Oishi, H. Jiang, L. Jiang, X. Li, K. Akhter, K. Hua, A. V. Faria, A. Mahmood, R. Woods, A. W. Toga, G. B. Pike, P. R. Neto, A. Evans, J. Zhang, H. Huang, M. I. Miller, P. van Zijl, and J. Mazziotta. "Stereotaxic white matter atlas based on diffusion tensor imaging in an ICBM template". *NeuroImage*, Vol. 40, No. 2, pp. 570–582, 2008.

[Mori 99] S. Mori and P. Barker. "Diffusion magnetic resonance imaging: its principle and applications". *The Anatomical Record*, Vol. 257, No. 3, pp. 102–109, 1999.

[Mose 90] M. E. Moseley, Y. Cohen, J. Mintorovitch, L. Chileuitt, H. Shimizu, J. Kucharczyk, M. F. Wendland, and P. R. Weinstein. "Early detection of regional cerebral ischemia in cats: comparison of diffusion- and T2-weighted MRI and spectroscopy". *Magnetic Resonance in Medicine*, Vol. 14, No. 2, pp. 330–346, 1990.

[Naka 07] T. Nakagawa, Y. Hayashi, Y. Hatanaka, A. Aoyama, T. Hara, A. Fujita, M. Kakogawa, H. Fujita, and T. Yamamoto. "Three-dimensional reconstruction of optic nerve head from stereo fundus images and its quantitative estimation". In: *Engineering in Medicine and Biology Society, 2007. EMBS 2007. 29th Annual International Conference of the IEEE*, pp. 6747–6750, 2007.

[Nave 07] R. Nave, S. Foresti, A. Pratesi, A. Ginestroni, M. Inzitari, E. Salvadori, M. Giannelli, S. Diciotti, D. Inzitari, and M. Mascalchi. "Whole-brain histogram and voxel-based analyses of diffusion tensor imaging in patients with leukoaraiosis: correlation with motor and cognitive impairment". *AJNR Am J Neuroradiol*, Vol. 28, No. 7, pp. 1313–1319, 2007.

[Naya 09] J. Nayak, R. Acharya, P. Bhat, N. Shetty, and T. Lim. "Automated diagnosis of glaucoma using digital fundus images". *Journal of Medical Systems*, Vol. 33, No. 5, pp. 337–346, 2009.

[Nolt 02] J. Nolte, Ed. *The human brain: an introduction to its functional anatomy, 5th Edition*. Mosby, 2002.

[Nour 04] K. Nouri-Mahdavi, D. Hoffman, D. P. Tannenbaum, S. K. Law, and J. Caprioli. "Identifying early glaucoma with optical coherence tomography". *American Journal of Ophthalmology*, Vol. 137, No. 2, pp. 228–235, 2004.

[Nuci 07] P. Nucifora, R. Verma, S. Lee, and E. Melhem. "Diffusion-tensor MR imaging and tractography: exploring brain microstructure and connectivity". *Radiology*, Vol. 245, No. 2, pp. 367–384, 2007.

[ODon 06] L. O'Donnell, M. Kubicki, M. Shenton, M. Dreusicke, W. Grimson, and C. Westin. "A method for clustering white matter fiber tracts". *American Journal of Neuroradiology*, Vol. 27, No. 5, pp. 1032–1036, 2006.

[Paje 99] S. Pajevic and C. Pierpaoli. "Color schemes to represent the orientation of anisotropic tissues from diffusion tensor data: application to white matter fiber tract mapping in the human brain". *Magnetic Resonance in Medicine*, Vol. 42, No. 3, pp. 526–540, 1999.

[Park 02a] G. J. Parker, K. E. Stephan, G. J. Barker, J. B. Rowe, D. G. MacManus, C. A. Wheeler-Kingshott, O. Ciccarelli, R. E. Passingham, R. L. Spinks, R. N. Lemon, and R. Turner. "Initial demonstration of in vivo tracing of axonal projections in the macaque brain and comparison with the human brain using diffusion tensor imaging and fast marching tractography". *NeuroImage*, Vol. 15, No. 4, pp. 797–809, 2002.

[Park 02b] G. Parker, C. Wheeler-Kingshott, and G. Barker. "Estimating distributed anatomical connectivity using fast marching methods and diffusion tensor imaging". *Medical Imaging, IEEE Transactions on*, Vol. 21, No. 5, pp. 505–512, 2002.

[Park 03] G. J. Parker, H. A. Haroon, and C. A. Wheeler-Kingshott. "A framework for a streamline-based probabilistic index of connectivity (PICo) using a structural interpretation of MRI diffusion measurements". *Journal of Magnetic Resonance Imaging*, Vol. 18, No. 2, pp. 242–254, 2003.

[Park 04] H. Park, C. Westin, M. Kubicki, S. Maier, M. Niznikiewicz, A. Baer, M. Frumin, R. Kikinis, F. Jolesz, R. McCarley, and M. Shenton. "White matter hemisphere asymmetries in healthy subjects and in schizophrenia:

a diffusion tensor MRI study". *NeuroImage*, Vol. 23, No. 1, pp. 213–223, 2004.

[Pele 06] S. Peled, O. Friman, F. Jolesz, and C.-F. Westin. "Geometrically constrained two-tensor model for crossing tracts in DWI". *Magnetic Resonance Imaging*, Vol. 24, pp. 1263–1270, 2006.

[Pele 98] S. Peled, H. Gudbjartsson, C. Westin, R. Kikinis, and F. Jolesz. "Magnetic resonance imaging shows orientation and asymmetry of white matter fiber tracts". *Brain Research*, Vol. 780, No. 1, pp. 27–33, 1998.

[Peng 09] H. Peng, A. Orlichenko, R. J. Dawe, G. Agam, S. Zhang, and K. Arfanakis. "Development of a human brain diffusion tensor template". *NeuroImage*, Vol. 46, No. 4, pp. 967–980, 2009.

[Penn 06] X. Pennec, P. Fillard, and N. Ayache. "A Riemannian framework for tensor computing". *Int. J. Comput. Vision*, Vol. 66, No. 1, pp. 41–66, 2006.

[Pero 90] P. Perona and J. Malik. "Scale-space and edge detection using anisotropic diffusion". *IEEE Transactions on Pattern Analysis and Machine Intelligence*, Vol. 12, No. 7, pp. 629–639, 1990.

[Pier 96a] C. Pierpaoli, P. Jezzard, P. Basser, A. Barnett, and G. Chiro. "Diffusion tensor MR imaging of the human brain". *Radiology*, Vol. 201, pp. 637–648, 1996.

[Pier 96b] C. Pierpaoli and P. J. Basser. "Toward a quantitative assessment of diffusion anisotropy". *Magnetic Resonance in Medicine*, Vol. 36, No. 6, pp. 893–906, 1996.

[Quig 06] H. Quigley and A. Broman. "The number of people with glaucoma worldwide in 2010 and 2020". *The British Journal of Ophthalmology*, Vol. 890, No. 3, pp. 262–267, 2006.

[Quig 99] H. A. Quigley. "Neuronal death in glaucoma". *Progress in Retinal and Eye Research*, Vol. 18, No. 1, pp. 39 – 57, 1999.

[Remi 04] L. Remington, Ed. *Clinical anatomy of the visual system, 2nd Edition.* Butterworth-Heinemann, 2004.

[Ritc 95] R. Ritch, J. Liebmann, and C. Tello. "A construct for understanding angle-closure glaucoma: the role of ultrasound biomicroscopy". *Ophthalmology Clinics of North America*, Vol. 8, pp. 281–293, 1995.

[Ritc 99] R. Ritch and J. M. Liebermann. "Angle closure glaucoma". *Asian Journal of Ophthalmology*, Vol. 1, No. 3, pp. 10–16, 1999.

[Ruec 99] D. Rueckert, L. Sonoda, C. Hayes, D. Hill, M. Leach, and D. Hawkes. "Nonrigid registration using free-form deformations: application to breast MR images". *IEEE Transactions on Medical Imaging*, Vol. 18, No. 8, pp. 712–721, 1999.

[Saey 07] Y. Saeys, I. n. Inza, and P. Larrañaga. "A review of feature selection techniques in bioinformatics". *Bioinformatics*, Vol. 23, No. 19, pp. 2507–2517, 2007.

[Sala 05] D. Salat, D. Tuch, D. Greve, A. van der Kouwe, N. Hevelone, A. Zaleta, B. Rosen, B. Fischl, S. Corkin, H. D. Rosas, and A. Dale. "Age-related alterations in white matter microstructure measured by diffusion tensor imaging". *Neurobiology of Aging*, Vol. 26, No. 8, pp. 1215–1227, 2005.

[Samp 00] P. A. Sample, C. F. Bosworth, E. Z. Blumenthal, C. Girkin, and R. N. Weinreb. "Visual function-specific perimetry for indirect comparison of different ganglion cell populations in glaucoma". *Investigative Ophthalmology & Visual Science*, Vol. 41, No. 7, pp. 1783–1790, 2000.

[Schu 08] T. Schultz and H.-P. Seidel. "Estimating crossing fibers: a tensor decomposition approach.". *IEEE Transactions on Visualization and Computer Graphics*, Vol. 14, No. 6, pp. 1635–1642, 2008.

[Sher 08a] A. Sherbondy, R. Dougherty, S. Napel, and B. Wandell. "Identifying the human optic radiation using diffusion imaging and fiber tractography". *J Vis*, Vol. 8, No. 10, pp. 12.1–11, 2008.

[Sher 08b] A. J. Sherbondy, R. F. Dougherty, M. Ben-Shachar, S. Napel, and B. A. Wandell. "ConTrack: finding the most likely pathways between brain regions using diffusion tractography". *Journal of Vision*, Vol. 8, No. 9, pp. 1–16, 2008.

[Shie 08] M. B. Shields. "Normal-tension glaucoma: is it different from primary open-angle glaucoma?". *Current Opinion in Ophthalmology*, Vol. 19, No. 2, pp. 85–88, 2008.

[Sinc 04] E. Sincoff, Y. Tan, and S. Abdulrauf. "White matter fiber dissection of the optic radiations of the temporal lobe and implications for surgical approaches to the temporal horn". *J Neurosurg*, Vol. 101, No. 5, pp. 739–746, 2004.

[Skar 00] S. Skare, T.-Q. Li, B. Nordell, and M. Ingvar. "Noise considerations in the determination of diffusion tensor anisotropy". *Magnetic Resonance Imaging*, Vol. 18, No. 6, pp. 659–669, 2000.

[Smit 06] S. Smith, M. Jenkinson, H. Johansen-Berg, D. Rueckert, T. Nichols, C. Mackay, K. Watkins, O. Ciccarelli, M. Cader, P. Matthews, and T. Behrens. "Tract-based spatial statistics: voxelwise analysis of multi-subject diffusion data". *NeuroImage*, Vol. 31, No. 4, pp. 1487–1505, 2006.

[Somm 91] A. Sommer, J. M. Tielsch, J. Katz, H. A. Quigley, J. D. Gottsch, J. Javitt, and Singh. "Relationship between intraocular pressure and primary open angle glaucoma among white and black americans: The Baltimore eye survey". *Arch Ophthalmol*, Vol. 109, No. 8, pp. 1090–1095, 1991.

[Song 03] S. Song, S. Sun, W. Ju, S. Lin, A. Cross, and A. Neufeld. "Diffusion tensor imaging detects and differentiates axon and myelin degeneration in mouse optic nerve after retinal ischemia". *NeuroImage*, Vol. 20, No. 3, pp. 1714–1722, 2003.

[Song 05] S. Song, J. Yoshino, T. Le, S. Lin, S. Sun, A. Cross, and R. Armstrong. "Demyelination increases radial diffusivity in corpus callosum of mouse brain". *NeuroImage*, Vol. 26, No. 1, pp. 132–140, 2005.

[Stae 06] P. Staempfli, T. Jaermann, G. Crelier, S. Kollias, A. Valavanis, and P. Boesiger. "Resolving fiber crossing using advanced fast marching tractography based on diffusion tensor imaging". *NeuroImage*, Vol. 30, No. 1, pp. 110–120, 2006.

[Stae 07] P. Staempfli, A. Rienmueller, C. Reischauer, A. Valavanis, P. Boesiger, and S. Kollias. "Reconstruction of the human visual system based on DTI fiber tracking". *Journal of Magnetic Resonance Imaging*, Vol. 26, No. 4, pp. 886–893, 2007.

[Stej 65] E. O. Stejskal and J. E. Tanner. "Spin diffusion measurements: spin echoes in the presence of a time-dependent field gradient". *The Journal of Chemical Physics*, Vol. 42, No. 1, pp. 288–292, 1965.

[Stie 11] L. H. Stieglitz, W. O. Lüdemann, M. Giordano, A. Raabe, R. Fahlbusch, and M. Samii. "Optic radiation fiber tracking using anteriorly angulated diffusion tensor imaging: a tested algorithm for quick application". *Neurosurgery*, Vol. 68, No. 5, pp. 1239–1251, 2011.

[Taka 10a] H. Takao, O. Abe, H. Yamasue, S. Aoki, K. Kasai, and K. Ohtomo. "Cerebral asymmetry in patients with schizophrenia: a voxel-based morphometry (VBM) and diffusion tensor imaging (DTI) study". *Journal of Magnetic Resonance Imaging*, Vol. 31, No. 1, pp. 221–226, 2010.

[Taka 10b] H. Takao, O. Abe, H. Yamasue, S. Aoki, K. Kasai, H. Sasaki, and K. Ohtomo. "Aging effects on cerebral asymmetry: a voxel-based morphometry and diffusion tensor imaging study". *Magnetic Resonance Imaging*, Vol. 28, No. 1, pp. 65–69, 2010.

[Tala 91] S. L. Talagala and I. J. Lowe. "Introduction to magnetic resonance imaging". *Concepts in Magnetic Resonance*, Vol. 3, No. 3, pp. 145–159, 1991.

[Tenc 02] C. Tench, P. Morgan, M. Wilson, and L. Blumhardt. "White matter mapping using diffusion tensor MRI". *Magnetic Resonance in Medicine*, Vol. 47, No. 5, pp. 967–972, 2002.

[Thiv 07] L. Thivard, P. Pradat, S. Lehéricy, L. Lacomblez, D. Dormont, J. Chiras, H. Benali, and V. Meininger. "Diffusion tensor imaging and voxel based morphometry study in amyotrophic lateral sclerosis: relationships with motor disability". *Journal of Neurology, Neurosurgery & Psychiatry*, Vol. 78, No. 8, pp. 889–892, 2007.

[Tour 02] J.-D. Tournier, F. Calamante, M. King, D. Gadian, and A. Connelly. "Limitations and requirements of diffusion tensor fiber tracking: an assessment using simulations". *Magnetic Resonance in Medicine*, Vol. 47, No. 4, pp. 701–708, 2002.

[Tour 04] J.-D. Tournier, F. Calamante, D. G. Gadian, and A. Connelly. "Direct estimation of the fiber orientation density function from diffusion-weighted MRI data using spherical deconvolution". *NeuroImage*, Vol. 23, No. 3, pp. 1176–1185, 2004.

[Tuch 02] D. Tuch, T. Reese, M. Wiegell, N. Makris, J. Belliveau, and V. Wedeen. "High angular resolution diffusion imaging reveals intravoxel white matter fiber heterogeneity". *Magnetic Resonance in Medicine*, Vol. 48, No. 4, pp. 577–582, 2002.

[Tuch 04] D. S. Tuch. "Q-ball imaging". *Magnetic Resonance in Medicine*, Vol. 52, No. 6, pp. 1358–1372, 2004.

[Tuck 98] M. Tuck and R. Crick. "The age distribution of primary open angle glaucoma". *Ophthalmic Epidemiology*, Vol. 5, No. 4, pp. 173–183, 1998.

[Ture 00] U. Türe, M. Yasargil, A. Friedman, and O. Al-Mefty. "Fiber dissection technique: lateral aspect of the brain". *Neurosurgery*, Vol. 47, No. 2, pp. 417–427, 2000.

[Vals 05] P. Valsasina, M. Rocca, F. Agosta, B. Benedetti, M. Horsfield, A. Gallo, M. Rovaris, G. Comi, and M. Filippi. "Mean diffusivity and fractional anisotropy histogram analysis of the cervical cord in MS patients". *NMR Biomed*, Vol. 26, No. 3, pp. 822–828, 2005.

[Waka 04] S. Wakana, H. Jiang, L. Nagae-Poetscher, P. van Zijl, and S. Mori. "Fiber tract-based atlas of human white matter anatomy". *Radiology*, Vol. 230, No. 1, pp. 77–87, 2004.

[Wang 05] Z. Wang and B. Vemuri. "DTI segmentation using an information theoretic tensor dissimilarity measure". *IEEE Transactions on Medical Imaging*, Vol. 24, No. 10, pp. 1267–1277, 2005.

[Wein 04] R. N. Weinreb and P. T. Khaw. "Primary open-angle glaucoma". *The Lancet*, Vol. 363, No. 9422, pp. 1711–1720, 2004.

[West 04] C. Westin, S. Maier, H. Mamata, A. Nabavi, F. Jolesz, and R. Kikinis. "Processing and visualization for diffusion tensor MRI". *Medical Image Analysis*, Vol. 6, No. 2, pp. 93–108, 2004.

[Wich 04] W. Wichmann and W. Müller-Forell. "Anatomy of the visual system". *Eur J Radiol*, Vol. 49, No. 1, pp. 8–30, 2004.

[Wood 07] I. A. Wood, P. M. Visscher, and K. L. Mengersen. "Classification based upon gene expression data: bias and precision of error rates". *Bioinformatics*, Vol. 23, No. 11, pp. 1363–1370, 2007.

[Xu 02] D. Xu, S. Mori, M. Solaiyappan, P. van Zijl, and C. Davatzikos. "A framework for callosal fiber distribution analysis". *NeuroImage*, Vol. 17, No. 3, pp. 1131–1143, 2002.

[Yoru 05] E. Yörük, B. Acar, and R. Bammer. "A physical model for MR-DTI based connectivity map computation". In: *MICCAI, Palm Springs, CA. Lecture Notes in Computer Science*, pp. 213–220, Springer, 2005.

[Yuce 03] Y. H. Yücel, Q. Zhang, R. N. Weinreb, P. L. Kaufman, and N. Gupta. "Effects of retinal ganglion cell loss on magno-, parvo-, koniocellular pathways in the lateral geniculate nucleus and visual cortex in glaucoma". *Progress in Retinal and Eye Research*, Vol. 22, No. 4, pp. 465–481, 2003.

[Zhan 05] J. Zhang, H. Ji, N. Kang, and N. Cao. "Fiber tractography in diffusion tensor magnetic resonance imaging: a survey and beyond". Technical Report No. 437-05, Department of Computer Science, University of Kentucky, Lexington, KY, 2005.

[Zhan 08] S. Zhang, S. Correia, and D. Laidlaw. "Identifying white-matter fiber bundles in DTI data using an automated proximity-based fiber-clustering method". *Visualization and Computer Graphics, IEEE Transactions on*, Vol. 14, No. 5, pp. 1044–1053, 2008.

[Zhuk 03] L. Zhukov, K. Museth, D. Breen, R. Whitaker, and A. Barr. "Level set modeling and segmentation of DT-MRI brain data". *Journal of Electronic Imaging*, Vol. 12, No. 1, pp. 125–133, 2003.